Handbook of Medical Imaging: Volume 3
Progess in Medical Image Processing and Analysis

SPIE Optical Engineering Press

J. Michael Fitzpatrick and Milan Sonka, Eds.

October 22, 1999

Contents

CHAPTER 3
Morphological Methods for Biomedical Image Analysis

John Goutsias
The Johns Hopkins University
Sinan Batman
The Johns Hopkins University

This chapter is an introduction to an image processing and analysis tool known as *mathematical morphology*. Our purpose is to provide an easy-to-read overview of basic aspects of this area of research and illustrate its applicability in image processing and analysis problems related to biomedical imaging.

3.1 Introduction

In most image processing and analysis applications, a given image f is transformed into an image g by means of an *image operator* ψ, such that $g = \psi(f)$. ψ is designed to perform a specific task; for example, to remove noise from f while preserving important image attributes (e.g., object boundaries). Usually, the image operator ψ is limited to satisfy two fundamental and intuitive properties: *distributivity* and *translation invariance*. If f is an image obtained by combining two images f_1 and f_2 with a given operation, then a *distributive operator* ψ applied on f produces an image g that is the result of combining images g_1 and g_2, obtained by applying ψ on f_1 and f_2, respectively, with the same operation. This property guarantees that the effect of operator ψ on the combined image can be deduced from applying ψ on the individual images. On the other hand, if f' is an image obtained by translating an image f, then ψ is a *translation invariant* operator if $g = \psi(f)$ implies that $g' = \psi(f')$. This property guarantees that operator ψ produces the same result (within a translation) when applied on translated versions of the same image.

The class of distributive image operators clearly depends on the way images are combined together. When images are combined by standard addition (i.e., by adding the graylevel values at each pixel), a distributive operator is called *linear* (provided that it also satisfies the scaling property $\psi(cf) = c\psi(f)$, for every image f and any constant c). For a linear and translation invariant operator ψ, we have that

$$g(x,y) = \psi(f)(x,y) = \int_{-\infty}^{\infty}\int_{-\infty}^{\infty} h(x-\xi, y-\eta) f(\xi,\eta) d\xi d\eta, \tag{3.1}$$

at each pixel $(x,y) \in E$, which is known as the *convolution equation*. Throughout this chapter, E will either be the two-dimensional Euclidean space $\mathbb{R}^2$ (for images defined over a continuous space), or the two-dimensional discrete space $\mathbb{Z}^2$ (for images that have been digitized). In (3.1), $h(x,y)$ is the *point spread function* of the linear operator ψ. In this case, the design of image operator ψ is equivalent to constructing an appropriate point spread function $h(x,y)$.

Image operators of the form (3.1) have been extensively used in image processing and analysis (e.g., see [1–3]). The main reason for their popularity is that (3.1) implies

$$G(\omega_x,\omega_y) = H(\omega_x,\omega_y)F(\omega_x,\omega_y), \quad -\infty \leq \omega_x, \omega_y \leq \infty, \tag{3.2}$$

where $F(\omega_x,\omega_y)$ denotes the 2D Fourier transform of an image $f(x,y)$, and $H(\omega_x,\omega_y)$ is the *frequency response* of operator ψ. Equation (3.2) is much simpler than (3.1), and dramatically simplifies mathematical calculations and numerical implementations. However, the product form of (3.2) reveals a major drawback for using operators (3.1) in image processing and analysis. We illustrate this argument with a simple example.

Assume that $f = f_0 + \eta$, where f_0 is a noise-free image and η is additive noise. We are interested in designing an image operator ψ that removes the noise η while preserving the image f_0. From (3.2), and the fact that $F(\omega_x,\omega_y) = F_0(\omega_x,\omega_y) + N(\omega_x,\omega_y)$, where $F_0(\omega_x,\omega_y)$ and $N(\omega_x,\omega_y)$ are the 2D Fourier transforms of $f_0(x,y)$ and $\eta(x,y)$, respectively, it is clear that

$$\begin{aligned} G(\omega_x,\omega_y) &= H(\omega_x,\omega_y)F(\omega_x,\omega_y) \\ &= H(\omega_x,\omega_y)F_0(\omega_x,\omega_y) + H(\omega_x,\omega_y)N(\omega_x,\omega_y). \end{aligned}$$

If

$$H(\omega_x,\omega_y) = \begin{cases} 1, & \text{for } (\omega_x,\omega_y) : N(\omega_x,\omega_y) = 0 \\ 0, & \text{otherwise} \end{cases},$$

then

$$G(\omega_x,\omega_y) = \begin{cases} F_0(\omega_x,\omega_y), & \text{for } (\omega_x,\omega_y) : N(\omega_x,\omega_y) = 0 \\ 0, & \text{otherwise} \end{cases}.$$

If the Fourier transform $N(\omega_x,\omega_y)$ of η is zero at low frequencies (which occurs in many practical situations), the resulting image g will be a lowpass

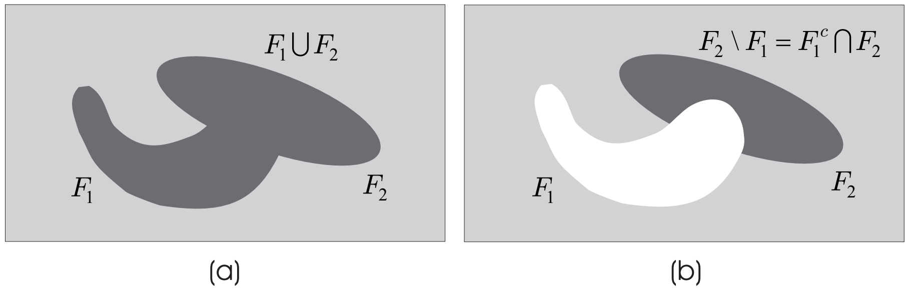

Figure 3.1: *When we look at two overlapping objects F_1 and F_2: (a) we either perceive both objects as one (i.e., we perceive their union $F_1 \cup F_2$), or (b) we perceive the non-occluded part of each object individually (i.e., we perceive their set difference $F_2 \setminus F_1 = F_1^c \cap F_2$).*

version of the noise-free image f_0 and the most desirable attributes in f_0 (e.g., object boundaries) will be smoothed out!

Another drawback of image operators of the form (3.1) is that they cannot be applied on binary (black and white) images. The reason is that linear operators of the form (3.1) assume that images are combined by standard addition, which is not possible in the binary case. An obvious question that arises here is: *how do we superimpose binary images?* A binary image (object) $f(x, y)$ can be either considered to be a function from E into $\{0, 1\}$ or a set F defined by $F = \{(x, y) \in E \mid f(x, y) = 1\}$. In the latter case, the *set-complement* F^c of F is given by $F^c = \{(x, y) \in E \mid f(x, y) = 0\}$. Note that, when we look at two overlapping objects F_1 and F_2, we either perceive both objects as one (i.e., we perceive their union $F_1 \cup F_2$), or we perceive the non-occluded part of each object individually (i.e., we perceive their set difference $F_1 \setminus F_2$ or $F_2 \setminus F_1$). This is illustrated in Fig. 3.1. Since $F_1 \setminus F_2 = F_1 \cap F_2^c$, this suggests that binary images are superimposed by either union or intersection. In this framework, a distributive *set operator* Ψ satisfies

$$\Psi(F_1 \cap F_2) = \Psi(F_1) \cap \Psi(F_2), \tag{3.3}$$

or

$$\Psi(F_1 \cup F_2) = \Psi(F_1) \cup \Psi(F_2). \tag{3.4}$$

Any set operator that satisfies (3.3) is called a binary *erosion*, whereas any set operator that satisfies (3.4) is called a binary *dilation*. Erosions and dilations are the most elementary operators of mathematical morphology [4–7]. We may therefore argue that *mathematical morphology is a natural algebraic framework for binary image processing and analysis.*

Mathematical morphology was first introduced in a seminal book by George Matheron, entitled *Random Sets and Integral Geometry* [4]. This book laid down the foundation of mathematical morphology and introduced it as a novel technique for image processing and analysis. Mathematical morphology was subsequently enriched and popularized by the highly inspiring book *Image Analysis and Mathematical Morphology* by Jean Serra [5]. Today, mathematical morphology is considered to be a powerful tool for image processing and analysis and has been used in numerous applications, including industrial inspection, automatic target detection, biomedical imaging, and remote sensing, just to mention a few.

From a theoretical point of view, mathematical morphology studies operators between complete lattices (i.e., nonempty sets furnished with a partial order relationship for which every subset has an infimum and a supremum); see [6, 8–10] for a lattice theoretic approach to mathematical morphology. Reasons why the theory of complete lattices is the right algebraic framework for mathematical morphology can be found in [11]. The power of mathematical morphology stems from the fact that, any translation invariant operator between complete lattices can be represented by means of elementary morphological operators (e.g., see [12, 13]). An image operator can be built by composing elementary morphological operators. However, this approach is not practical due to the need of using a prohibitively large number of elementary operators. Fortunately, most applications can be satisfactorily dealt with by restricting the number of morphological operators. The key task of the image analyst is to identify the family of morphological operators needed for a particular problem, whether it is for shape detection, extraction, or filtering.

The concept of erosion (dilation) can be extended to the grayscale case in a rather straightforward manner. As it will soon become clear, this is accomplished by means of the so-called *threshold decomposition*, which uniquely represents a grayscale image as a collection of binary images, known as the *cross sections*. Using threshold decomposition, the grayscale analogues of union and intersection are *supremum* and *infimum*, respectively (or maximum and minimum in the case of a finite number of images). Therefore, and as far as grayscale morphology is concerned, two grayscale images f_1 and f_2 are combined by means of (pixelwise) minimum or maximum, in order to produce images $f_1 \wedge f_2$ and $f_1 \vee f_2$, given by

$$\begin{aligned}(f_1 \wedge f_2)(x, y) &= f_1(x, y) \wedge f_2(x, y)\\ (f_1 \vee f_2)(x, y) &= f_1(x, y) \vee f_2(x, y),\end{aligned}$$

where $\wedge$ and $\vee$ denote infimum and supremum, respectively. In this framework, a distributive grayscale operator ψ either satisfies

$$\psi(f_1 \wedge f_2) = \psi(f_1) \wedge \psi(f_2), \tag{3.5}$$

or

$$\psi(f_1 \vee f_2) = \psi(f_1) \vee \psi(f_2). \tag{3.6}$$

Any operator that satisfies (3.5) is called a grayscale erosion, whereas any operator that satisfies (3.6) is called a grayscale dilation.

Later in this chapter, we will see that, for a grayscale translation invariant erosion ψ_ϵ, we have

$$\psi_\epsilon(f)(x,y) = \bigwedge_{\xi,\eta}[f(\xi,\eta) - b(\xi - x, \eta - y)], \tag{3.7}$$

whereas, for a grayscale translation invariant dilation ψ_δ, we have

$$\psi_\delta(f)(x,y) = \bigvee_{\xi,\eta}[f(\xi,\eta) + b(x - \xi, y - \eta)], \tag{3.8}$$

where $b(x,y)$ is a grayscale image known as the *structuring function*. Notice the striking similarity between (3.1) and (3.7), (3.8). For example, by comparing (3.1) with (3.8), it is clear that (3.8) is obtained by replacing the integral in (3.1) with the supremum, the point spread function with the structuring function, and the product with an addition. For this reason, (3.7) and (3.8) are sometimes called *morphological convolutions*.

Our purpose in this chapter is to provide an easy-to-read overview of basic aspects of mathematical morphology and illustrate its use in image processing and analysis problems related to biomedical imaging. The reader is referred to [2,3,14,15] for an elementary treatment, and to [4–7,16–19] for a more advanced exposition. The number of publications available on mathematical morphology has grown substantially. Due to space limitation, we limit our references here to publications which complement our exposition. For works using mathematical morphology in biomedical imaging applications, the reader is referred to [20–53], among many other publications.

In this chapter, we first choose to discuss mathematical morphology on binary images. This is the subject of Sections 3.2 and 3.3. We then extend our exposition to mathematical morphology on grayscale images. This is the subject of Sections 3.4 and 3.5. Although such a route produces some redundancy, we believe that is more pleasing to the reader for a very simple reason: binary morphology can be easily visualized by means of geometry, making the exposition very intuitive. In Section 3.6, we discuss the problem of binary and grayscale morphological image reconstruction. In mathematical morphology, image reconstruction is the process of extracting desirable parts from a given image, which have been marked by a set of markers. Image reconstruction turns-out to be very effective in problems of object detection and image segmentation. The problem of binary and grayscale image segmentation by means of morphological operators and, in particular, by means of the watershed transform, is discussed in Section 3.7. Finally, Section 3.8 summarizes our concluding remarks and provides a brief discussion on some recent developments in mathematical morphology. Moreover, this section gives a list of web sites where mathematical morphology software and toolboxes can be found.

Throughout this chapter, we illustrate basic concepts by means of examples derived from biomedical imaging applications. Most of these examples are used for illustration purposes only and they should not be thought of as validated solutions to the biomedical imaging problems associated with them.

Before we proceed, we would like to make some remarks regarding our notation. Grayscale images (functions) are denoted with small letters $f, g, \ldots$. Capital letters $F, G, \ldots$ denote binary images (sets). For simplicity of presentation, we limit ourselves to images defined over the two-dimensional Euclidean plane $\mathbb{R}^2$ or the two-dimensional discrete plane $\mathbb{Z}^2$. However, most of the concepts discussed here can be extended to higher dimensions (e.g., see [31]). The pair (x, y) will denote a point (pixel) in $\mathbb{R}^2$ or $\mathbb{Z}^2$. However, we also use $u, h, \ldots$ to denote points in E. Finally, set operators (i.e., operators which apply on binary images and produce binary images) will be denoted with capital Greek letters $\Psi, \Pi, \ldots$, whereas grayscale operators (i.e., operators which apply on grayscale images and produce grayscale images) will be denoted with small Greek letters $\psi, \pi, \ldots$.

3.2 Binary morphological operators

Mathematical morphology is a tool for extracting geometric information from binary and grayscale images. A shape probe (known as a *structuring element*) is used to build an image operator whose output depends on whether or not this probe fits inside a given image. Clearly, the nature of the extracted information depends on the shape and size of the probe used. To illustrate this concept, we initially restrict our discussion to the case of binary images.

3.2.1 Increasing and translation invariant operators

The most elementary set operators of interest to mathematical morphology are operators which are increasing and/or translation invariant. A set operator Ψ is *increasing* if

$$F_1 \subseteq F_2 \quad \Rightarrow \quad \Psi(F_1) \subseteq \Psi(F_2).$$

An increasing operator Ψ forbids an object F_1 that is occluded by an object F_2 to become visible after processing (i.e., $\Psi(F_1)$ will still be occluded by $\Psi(F_2)$).

On the other hand, translation invariance plays an important role in image processing and analysis. In most applications, an image object should be processed the same way no matter where it is located on the imaging plane. If $F + h = \{u + h \mid u \in F\}$ denotes the translation of a set F by $h \in E$, then a set operator Ψ is *translation invariant* if

$$\Psi(F + h) = \Psi(F) + h,$$

for every translation $h \in E$. A set operator may be increasing but not translation invariant and vice-versa. Most frequently however, we are interested in operators which are both increasing and translation invariant.

3.2.2 Erosion and dilation

As we discussed in Section 3.1, a set operator Ψ_ϵ, for which

$$\Psi_\epsilon(F_1 \cap F_2) = \Psi_\epsilon(F_1) \cap \Psi_\epsilon(F_2), \tag{3.9}$$

for every pair (F_1, F_2) of binary images, is a binary erosion, whereas, a set operator Ψ_δ, for which

$$\Psi_\delta(F_1 \cup F_2) = \Psi_\delta(F_1) \cup \Psi_\delta(F_2), \tag{3.10}$$

for every pair (F_1, F_2) of binary images, is a binary dilation. As a direct consequence of (3.9) and (3.10), both erosion and dilation are increasing operators (e.g., if $F_1 \subseteq F_2$, then (3.9) implies $\Psi_\epsilon(F_1) = \Psi_\epsilon(F_1 \cap F_2) = \Psi_\epsilon(F_1) \cap \Psi_\epsilon(F_2) \subseteq \Psi_\epsilon(F_2)$).

Every translation invariant erosion is of the form

$$\Psi_\varepsilon(F) = \bigcap_{b \in B} F - b = F \ominus B,$$

for some elementary subset B of the two-dimensional space, known as a *structuring element* (e.g., see [6]). In set theory, the translation invariant erosion is known as the *Minkowski subtraction*. It can be shown that

$$F \ominus B = \{h \in E \mid (B + h) \subseteq F\}.$$

This formula provides a geometric interpretation for the translation invariant erosion. It suggests that the translation invariant erosion of a set (shape) F by a structuring element B comprises all points h of E such that the structuring element B located at h fits entirely inside F.

The effect of the translation invariant erosion, using a disk structuring element, is illustrated in Fig. 3.2(a). Notice that F is “shrunk” (i.e., $F \ominus B \subseteq F$) in a manner determined by the shape and size of the structuring element B. This is always true when the structuring element contains the origin. In general, a set operator Ψ for which $\Psi(F) \subseteq F$, for every image F, is called *anti-extensive*.

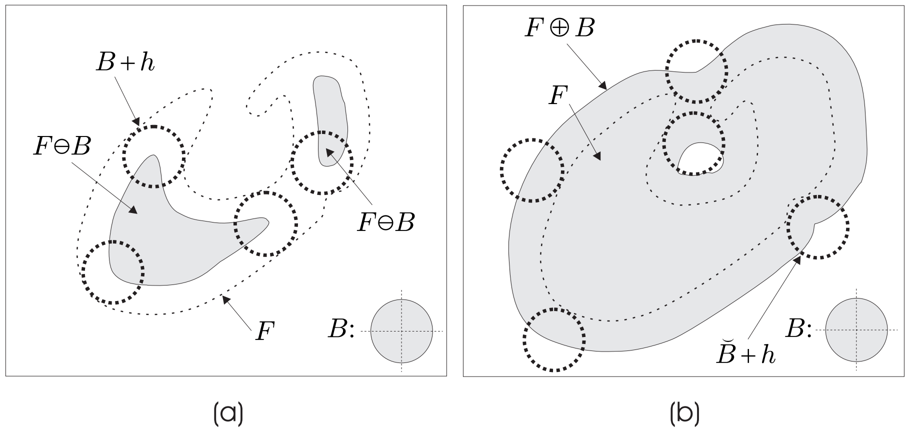

Figure 3.2: *The effect of translation invariant erosion, in (a), and translation invariant dilation, in (b), on a shape F. Notice that F is "shrunk" in (a) whereas it is "expanded" in (b).*

Similarly, every translation invariant dilation is of the form

$$\Psi_\delta(F) = \bigcup_{b\,\in B} F + b = F \oplus B,$$

for some structuring element B. In set theory, the translation invariant dilation is known as the *Minkowski addition*. It can be shown that

$$F \oplus B = \{h \in E \mid (\breve{B} + h) \cap F \neq \emptyset\},$$

where $\breve{B} = \{-b \mid b \in B\}$ is the *reflection* of B with respect to the origin. This formula suggests that the dilation of a set (shape) F by a structuring element B comprises all points h such that the reflected structuring element $\breve{B}$ translated to h hits (intersects) F. Moreover, $F \oplus B = (F^c \ominus \breve{B})^c$, which is a form of *duality* between erosion and dilation. This relationship simply says that the dilation of a shape F by a structuring element B is the set complement of the erosion of the set complement of F with structuring element $\breve{B}$.

The effect of the translation invariant dilation, using a disk structuring element, is illustrated in Fig. 3.2(b). Notice that F is "expanded" (i.e., $F \subseteq F \oplus B$) in a manner determined by the shape and size of B. This is always true when B contains the origin. In general, a set operator Ψ for which $\Psi(F) \supseteq F$, for every image F, is called *extensive*.

Some properties of erosion and dilation are listed in Tables 3.1 and 3.2. In these tables, $rF = \{ru \mid u \in F\}$ is the *scaled* version of F. Throughout this chapter, we simply refer to translation invariant erosion and dilation as erosion and dilation, respectively.

$F\ominus\{h\} = F - h$	
$(F+h)\ominus B = F\ominus(B-h) = (F\ominus B)+h$	Translation invariance
$F\ominus B_1 \supseteq F\ominus B_2$ if $B_1 \subseteq B_2$	Decreasingness with respect to structuring element
$F\ominus(B_1 \bigcup B_2) = (F\ominus B_1)\bigcap(F\ominus B_2)$	Parallel composition
$(F_1 \bigcap F_2)\ominus B = (F_1\ominus B)\bigcap(F_2\ominus B)$	Distributivity of intersection
$F\ominus(B_1 \bigcap B_2) \supseteq (F\ominus B_1)\bigcup(F\ominus B_2)$	Parallel composition inequality
$(F_1 \bigcup F_2)\ominus B \supseteq (F_1\ominus B)\bigcup(F_2\ominus B)$	Parallel composition inequality
$(F\ominus B_1)\ominus B_2 = F\ominus(B_1 \oplus B_2)$	Serial composition
$F_1 \subseteq F_2 \Rightarrow F_1\ominus B \subseteq F_2\ominus B$	Increasingness with respect to shape
$rF\ominus rB = r(F\ominus B)$	Homogeneity
$F\ominus B \subseteq F$ if B contains the origin	Anti-extensitivity
$F\ominus B = (F^c \oplus \breve{B})^c$	Duality

Table 3.1: *Some properties of binary erosion.*

The effect of erosion and dilation on a binarized image of a histological breast sample is shown in Fig. 3.3. Notice that erosion by a disk structuring element with a diameter of 3 pixels, effectively removes debris, producing the clean image depicted in Fig. 3.3(c). However, when a larger disk is used, significant portions of the image are removed as well. This is depicted in Fig. 3.3(d). Clearly, the erosion is very sensitive to "pepper" noise (i.e., small black dots) in the image, which tends to get larger in size. Reciprocally, dilation effectively "expands" the main features in an image, as depicted in Figs. 3.3(e),(f).

3.2.3 Representational power of erosions and dilations

A celebrated theorem by George Matheron states that, every translation invariant and increasing set operator can be expressed as a union of erosions or intersection of dilations [4]. To be more precise, for any translation invariant and increasing set operator Ψ, we have that

$$\Psi(F) \;=\; \bigcup_{B\in\mathcal{K}(\Psi)} F\ominus B \;=\; \bigcap_{B\in\mathcal{K}(\Psi^*)} F\oplus\breve{B}, \tag{3.11}$$

where $\mathcal{K}(\Psi)$ is the *kernel* of operator Ψ, defined by

$$\mathcal{K}(\Psi) = \{B \mid \Psi(B) \text{ contains the origin}\}, \tag{3.12}$$

and Ψ^* is the *dual* of operator Ψ, given by $\Psi^*(F) = [\Psi(F^c)]^c$. This result however is mainly of theoretical interest since, in practice, the kernel is highly

$F \oplus \{h\} = F + h$	
$F \oplus B = B \oplus F$	Commutativity
$(F + h) \oplus B = F \oplus (B + h) = (F \oplus B) + h$	Translation invariance
$F \oplus B_1 \subseteq F \oplus B_2$ if $B_1 \subseteq B_2$	Increasingness with respect to structuring element
$F \oplus (B_1 \cup B_2) = (F \oplus B_1) \cup (F \oplus B_2)$	Parallel composition
$(F_1 \cup F_2) \oplus B = (F_1 \oplus B) \cup (F_2 \oplus B)$	Distributivity of union
$F \oplus (B_1 \cap B_2) \subseteq (F \oplus B_1) \cap (F \oplus B_2)$	Parallel composition inequality
$(F \oplus B_1) \oplus B_2 = F \oplus (B_1 \oplus B_2)$	Serial composition
$F_1 \subseteq F_2 \Rightarrow F_1 \oplus B \subseteq F_2 \oplus B$	Increasingness with respect to shape
$rF \oplus rB = r(F \oplus B)$	Homogeneity
$F \oplus B \supseteq F$ if B contains the origin	Extensitivity
$F \oplus B = (F^c \ominus \breve{B})^c$	Duality

Table 3.2: *Some properties of binary dilation.*

redundant. Usually, a subset $\mathcal{B}(\Psi)$ of the kernel $\mathcal{K}(\Psi)$ is found, known as the *basis* of Ψ, which is much smaller than the kernel and can still represent the operator [54]. We illustrate this for the case of a median filter.

The median filter is an increasing and translation invariant operator, and as such, it is amenable to the representation dictated by (3.11). Indeed, the median filter over the cross mask $\{(0,0),(1,0),(-1,0),(0,1),(0,-1)\}$, centered at the origin $(0,0)$, has a basis that consists of the following ten structuring elements [55]:

$$\begin{pmatrix} 0 & 0 & 0 \\ 1 & \underline{1} & 1 \\ 0 & 0 & 0 \end{pmatrix} \begin{pmatrix} 0 & 1 & 0 \\ 0 & \underline{1} & 0 \\ 0 & 1 & 0 \end{pmatrix} \begin{pmatrix} 0 & 1 & 0 \\ 1 & \underline{0} & 0 \\ 0 & 1 & 0 \end{pmatrix} \begin{pmatrix} 0 & 0 & 0 \\ 1 & \underline{0} & 1 \\ 0 & 1 & 0 \end{pmatrix} \begin{pmatrix} 0 & 1 & 0 \\ 0 & \underline{0} & 1 \\ 0 & 1 & 0 \end{pmatrix}$$

$$\begin{pmatrix} 0 & 1 & 0 \\ 1 & \underline{0} & 1 \\ 0 & 0 & 0 \end{pmatrix} \begin{pmatrix} 0 & 1 & 0 \\ 1 & \underline{1} & 0 \\ 0 & 0 & 0 \end{pmatrix} \begin{pmatrix} 0 & 1 & 0 \\ 0 & \underline{1} & 1 \\ 0 & 0 & 0 \end{pmatrix} \begin{pmatrix} 0 & 0 & 0 \\ 0 & \underline{1} & 1 \\ 0 & 1 & 0 \end{pmatrix} \begin{pmatrix} 0 & 0 & 0 \\ 1 & \underline{1} & 0 \\ 0 & 1 & 0 \end{pmatrix}$$

where the underlined digit denotes the center of the structuring element. Notice that the cross mask contains five elements. The output of the median filter, with the mask placed at a pixel (x, y) of an image F, is 1, if at least three of the pixels in the mask have value 1, and is zero otherwise. This is equivalent to at least one of the structuring elements in the basis, shifted at pixel (x, y), being a subset of F. According to (3.11), with $\mathcal{K}(\Psi)$ being replaced by $\mathcal{B}(\Psi)$, the median filter over the cross mask can be implemented as the union of ten erosions with the structuring elements listed above. Notice that the erosion of F by any of these structuring elements can be implemented by an AND operation, whereas the union of erosions can

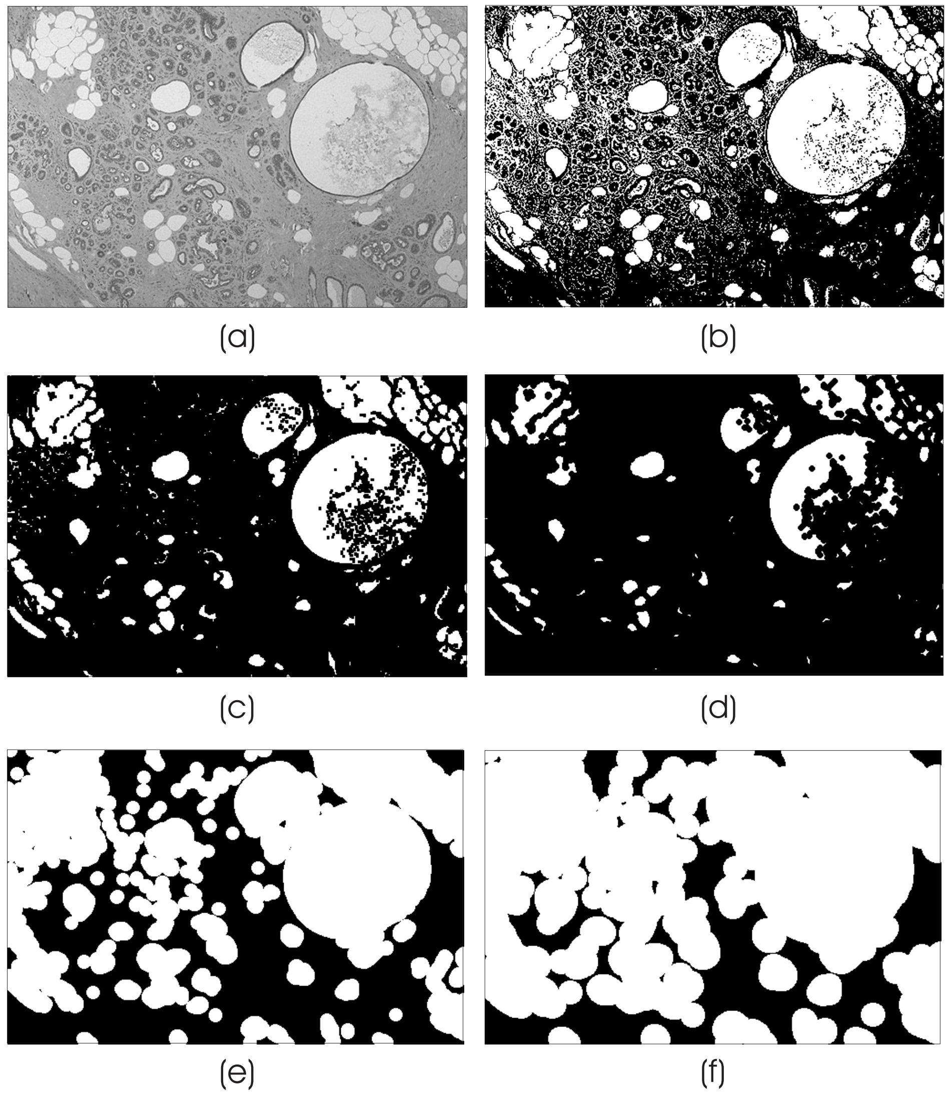

Figure 3.3: *Binary erosion and dilation: (a) original grayscale image of the histologic appearance of fibrocystic changes in breast; (b) original image after binarization; (c) erosion of (b) by a disk structuring element with a diameter of* 3 *pixels; (d) erosion of (b) by a disk structuring element with a diameter of* 7 *pixels; (e) dilation of (c) by a disk structuring element with a diameter of* 15 *pixels; (f) dilation of (c) by a disk structuring element with a diameter of* 27 *pixels. – Data courtesy of K. C. Klatt, Department of Pathology, University of Utah. Used with permission.*

be implemented by an OR operation. Therefore, the representation (3.11) on one hand provides a link between erosions and median filters, and on the other hand provides a way of implementing median filters by means of AND and OR operations.

3.2.4 Opening and closing

In general, the erosion and dilation operators do not enjoy an often desirable property, known as *idempotence*: an idempotent shape operator excerpts all information from a single application, while consecutive applications of the same operator will not have any effect. The ideal bandpass filter is an example of a linear operator that shares this property. The erosion and dilation operators on the other hand keep modifying the image at each successive application. However, when a translation invariant erosion $F \ominus B$ is composed with a translation invariant dilation $F \oplus B$, the resulting operator is idempotent, regardless of the order of composition. The composition $(F \ominus B) \oplus B$ is called an *opening*, whereas the composition $(F \oplus B) \ominus B$ is called a *closing*.

The notions of opening and closing are however more general: a set operator Ψ that is increasing (i.e., $F_1 \subseteq F_2 \Rightarrow \Psi(F_1) \subseteq \Psi(F_2)$), anti-extensive (i.e., $\Psi(F) \subseteq F$), and idempotent (i.e., $\Psi\Psi(F) = \Psi(F)$) is called an *opening*, whereas a set operator Ψ that is increasing, extensive (i.e., $F \subseteq \Psi(F)$), and idempotent is called a *closing*. It can be shown that openings and closings are closed with respect to union and intersection, respectively. This means that union of openings is an opening, whereas intersection of closings is a closing.

The operator

$$F \circ B = (F \ominus B) \oplus B \tag{3.13}$$

is referred to as the *structural opening*, since it involves a structuring element B. Later, the reader will have the opportunity to encounter openings which are not of this form. It can be shown that

$$F \circ B = \bigcup \{B + h \mid h \in E \text{ and } (B + h) \subseteq F\}.$$

This formula provides a geometric interpretation for the structural opening in (3.13). It suggests that $F \circ B$ is the union of all translated structuring elements $B + h$ that fit inside F. The effect of the structural opening $F \circ B$ (using a disk structuring element) is illustrated in Fig. 3.4(a). Notice that $F \circ B$ attempts to undo the effect of erosion $F \ominus B$, by applying the associated dilation $(F \ominus B) \oplus B$. Opening a shape F with a structuring element B removes all components of F which are "smaller" than B, in the sense that they cannot contain any translated replica of B. It therefore acts as a *smoothing* filter. The amount and type of smoothing is determined by the shape and size of the structuring element used.

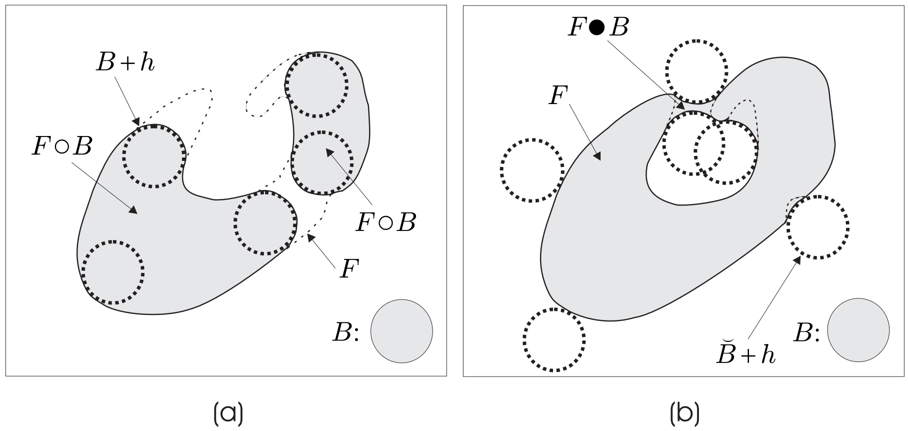

Figure 3.4: *The effect of structural opening, in (a), and structural closing, in (b), on a shape F.*

Similarly, the operator

$$F \bullet B = (F \oplus B) \ominus B$$

is referred to as the *structural closing*. It can be shown that

$$F \bullet B = \{u \in E \mid u \in \breve{B} + h \Rightarrow (\breve{B} + h) \cap F \neq \emptyset\}.$$

This formula suggests that $F \bullet B$ is the collection of all pixels u such that, all translated structuring elements $\breve{B} + h$ which contain u intersect F. The effect of the structural closing $F \bullet B$ (using a disk structuring element) is illustrated in Fig. 3.4(b). Notice that $F \bullet B$ attempts to undo the effect of dilation $F \oplus B$, by applying the associated erosion $(F \oplus B) \ominus B$. Closing a shape F with a structuring element B removes all components of F^c which are "smaller" than $\breve{B}$. This is a direct consequence of the duality between structural openings and closings, which says that $F \bullet B = (F^c \circ \breve{B})^c$.

Some properties of structural openings and closings are listed in Tables 3.3 and 3.4, respectively. The effect of these operators on a binarized image of a histological breast sample is depicted in Fig. 3.5 (see also Fig. 3.3).

Another useful opening operator is the so-called binary *area opening*. This operator removes a *grain* from a binary image whose area is below a given value. By a grain of an image F, we mean a *connected component* F_i of F. A component $F_i \subseteq F \subseteq E$ is *connected* if, given two pixels in F_i, there exists at least one path that connects these two pixels and lies entirely in F_i. Mathematically, the binary area opening is expressed by

$$\Psi_{\text{areaopn}}(F, \alpha) = \bigcup \{F_i \mid |F_i| \geq \alpha\},$$

$F \circ \{h\} = F$	
$(F+h) \circ B = (F \circ B) + h$	Translation invariance
$F \circ (B+h) = F \circ B$	
$F_1 \subseteq F_2 \Rightarrow F_1 \circ B \subseteq F_2 \circ B$	Increasingness with respect to shape
$rF \circ rB = r(F \circ B)$	Homogeneity
$F \circ B \subseteq F$	Anti-extensitivity
$(F \circ B) \circ B = F \circ B$	Idempotence
$F \circ B = (F^c \bullet \breve{B})^c$	Duality

Table 3.3: *Some properties of the binary structural opening.*

where $\{F_i \mid i = 1, 2, \ldots\}$ are the grains of F and $|A|$ denotes the *area* of A (when A is a discrete set, $|A|$ denotes the number of its elements, or the so-called *cardinality*). It is not difficult to see that, for a fixed value of α, this operator is increasing, anti-extensive, and idempotent and, therefore, is an opening. The area opening is a morphological filter that filters-out grains of area less than a specified value, whereas it passes grains of area larger than this value.

By duality, the binary area closing is defined as follows:

$$\Psi_{\text{areaclo}}(F, \alpha) = [\Psi_{\text{areaopn}}(F^c, \alpha)]^c.$$

The area closing fills-in the holes in a binary image, whose area is strictly smaller than α.

3.2.5 Representational power of structural openings and closings

As we mentioned in the previous subsection, the union of openings is still an opening, whereas the intersection of closings is a closing. This simple observation is very useful in practice, since it allows the design of openings and closings by taking the union or intersection of elementary openings or closings, respectively. This observation however is more general. It can be shown (e.g., see [6]) that any translation invariant opening Ψ_{opn} (i.e., a translation invariant operator that is increasing, anti-extensive, and idempotent) can be written as a union of structural openings, whereas any translation invariant closing Ψ_{clo} (i.e., a translation invariant operator that is increasing, extensive, and idempotent) can be written as an intersection of structural closings; i.e.,

$$\Psi_{\text{opn}}(F) = \bigcup_{B \in \text{Inv}(\Psi_{\text{opn}})} F \circ B \quad \text{and} \quad \Psi_{\text{clo}}(F) = \bigcap_{B \in \text{Inv}(\Psi_{\text{clo}})} F \bullet (\breve{B})^c, \tag{3.14}$$

$F \bullet \{h\} = F$	
$(F+h) \bullet B = (F \bullet B) + h$	Translation invariance
$F \bullet (B+h) = F \bullet B$	
$F_1 \subseteq F_2 \Rightarrow F_1 \bullet B \subseteq F_2 \bullet B$	Increasingness with respect to shape
$rF \bullet rB = r(F \bullet B)$	Homogeneity
$F \subseteq F \bullet B$	Extensitivity
$(F \bullet B) \bullet B = F \bullet B$	Idempotence
$F \bullet B = (F^c \circ \breve{B})^c$	Duality

Table 3.4: *Some properties of the binary structural closing.*

where $\mathrm{Inv}(\Psi)$ denotes the *invariance domain* of operator Ψ, given by $\mathrm{Inv}(\Psi) = \{F \mid \Psi(F) = F\}$.

Recall that translation invariant openings and closings are increasing operators. Therefore, they admit a decomposition in terms of a union of erosions or an intersection of dilations, as dictated by (3.11). However, the design of a translation invariant opening or closing based on these types of decompositions is cumbersome and less intuitive. On the other hand, the design of translation invariant openings and closings by means of (3.14) is more intuitive and easier to implement. We illustrate these remarks with a simple example.

Consider the problem of detecting slit-like "cholesterol clefts" of lipid material in the aortic atheromatous plaque that lead to coronary atherosclerosis. A sample of aortic atheromatous plaque is shown in Fig. 3.6(a). Notice that "cholesterol clefts" are the randomly rotated white elongated structures on the left-hand side of the image. The vertical bright streaks on the right-hand side belong to the artery wall and are of no interest here. A union of structural openings, using 3 linear structuring elements (a horizontal, a left diagonal, and a right diagonal) of length 4, is applied to the image. It is hoped that the structuring elements will fit inside the majority of the clefts while eliminating noise due to binarization and unwanted structures. The results are depicted in Figs. 3.6(c)–(e). Observe that all unwanted debris and external structures have been eliminated. The resulting opening does a formidable job in isolating all but the vertically aligned "cholesterol clefts." This process could be augmented, by adding a vertical structuring element, to extract more of the vertically oriented clefts that remain. However, this may erroneously mark part of the coronary structure as clefts.

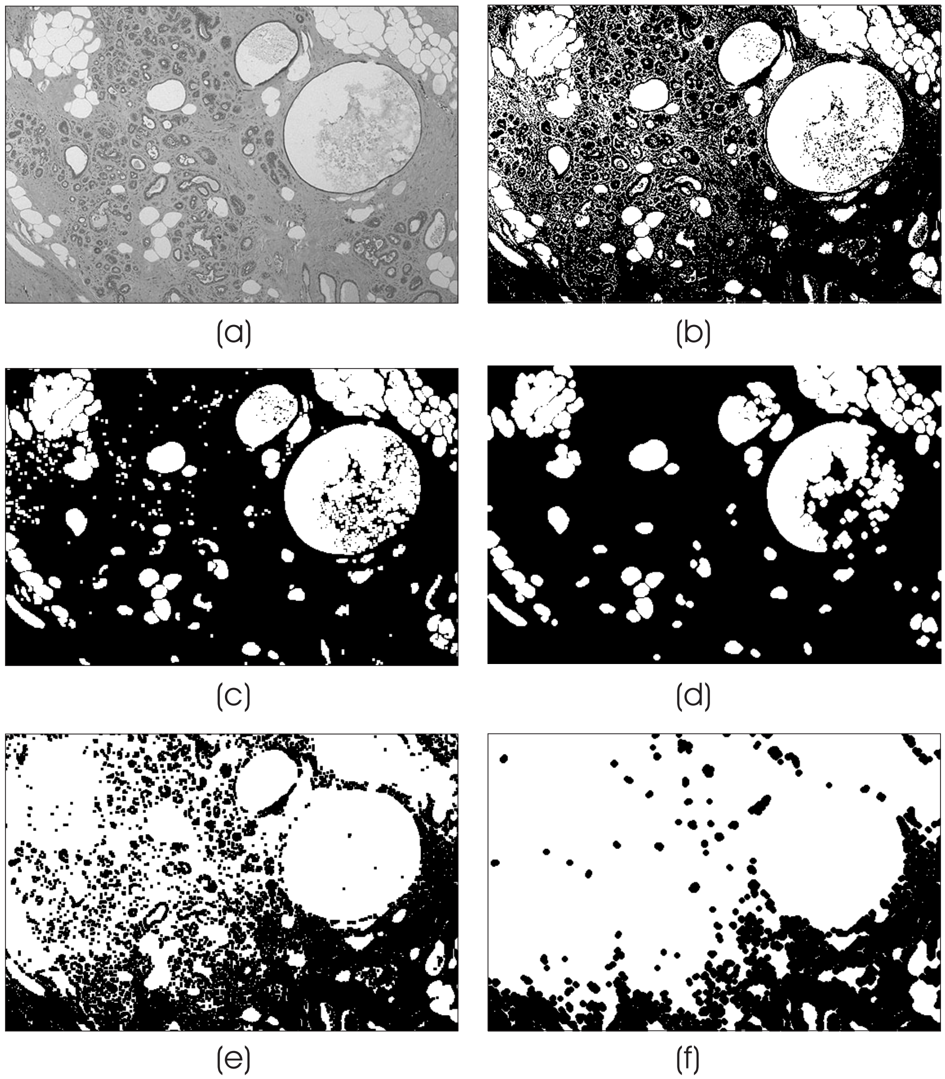

Figure 3.5: *An example of binary structural opening and closing: (a) original grayscale image of the histologic appearance of fibrocystic changes in breast; (b) original image after binarization; (c) structural opening by a disk structuring element with a diameter of* 3 *pixels; (d) structural opening by a disk structuring element with a diameter of* 7 *pixels; (e) structural closing by a disk structuring element with a diameter of* 3 *pixels; (f) structural closing by a disk structuring element with a diameter of* 7 *pixels. – Data courtesy of K. C. Klatt, Department of Pathology, University of Utah. Used with permission.*

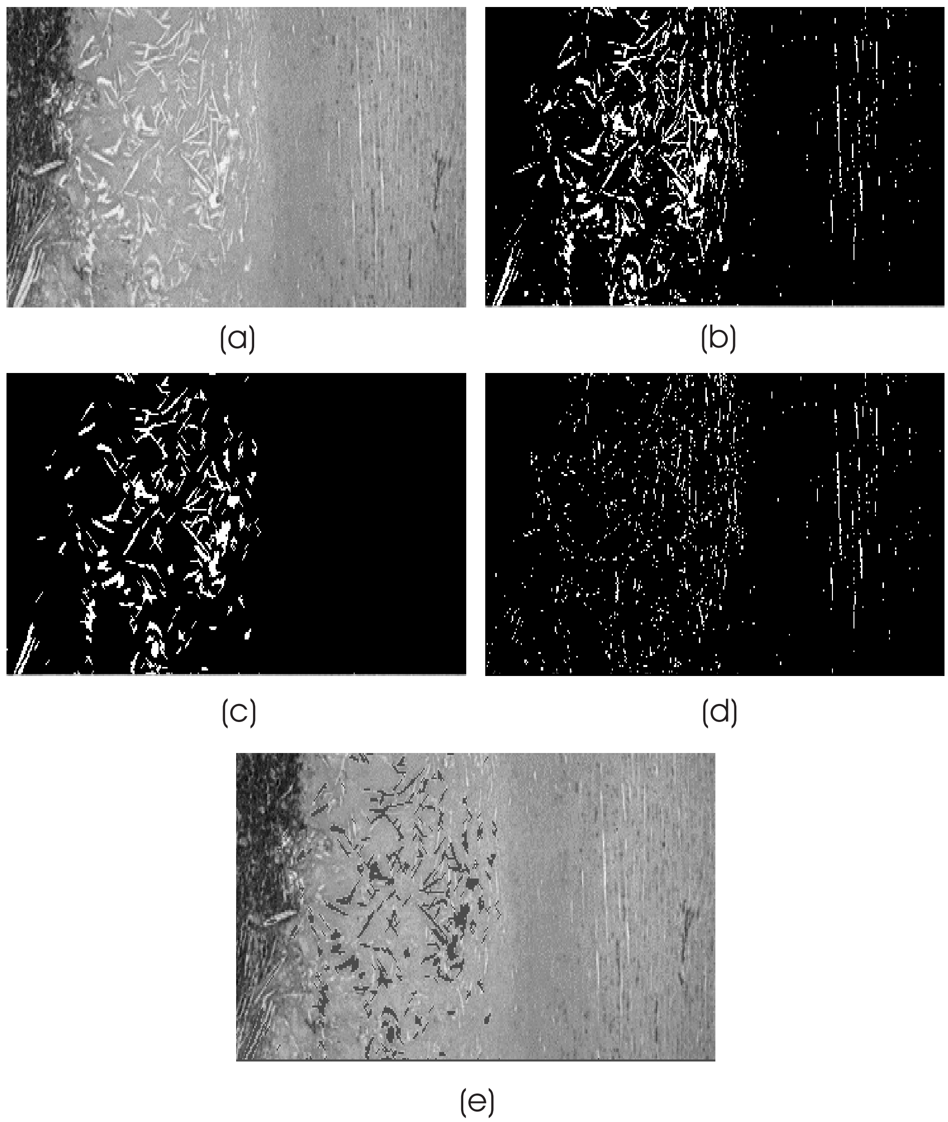

Figure 3.6: *Filtering via a union of openings: (a) original grayscale image of aortic atheromatous plaque; (b) original image after binarization; (c) the result of applying a union of openings, with* 3 *linear structuring elements (a horizontal, a left diagonal, and a right diagonal) of length* 4*, on the image in (b); (d) filter residue (the set difference between images (b) and (c)); (e) the result in (c) overlaid on the original grayscale image in (a). – Data courtesy of E. C. Klatt, Department of Pathology, University of Utah. Used with permission.*

$(F+h)\otimes(A,B)=[F\otimes(A,B)]+h$	Translation Invariance
$F^c\otimes(A,B)=F\otimes(B,A)$	
$F\otimes(A+h,B+h)=[F\otimes(A,B)]-h$	
$rF\otimes(rA,rB)=r[F\otimes(A,B)]$	Homogeneity
$A=\varnothing \;\Rightarrow\; F\otimes(A,B)=F^c\ominus B$	Decreasing operator
$B=\varnothing \;\Rightarrow\; F\otimes(A,B)=F\ominus A$	Increasing operator
$A\bigcap B\neq\varnothing \;\Rightarrow\; F\otimes(A,B)=\varnothing$	

Table 3.5: *Some properties of the hit-or-miss operator.*

3.2.6 The hit-or-miss operator

Instead of only probing the inside, or the outside, of a given binary image with a structuring element, it may be fruitful in certain applications to probe both the background and the foreground at the same time. The *hit-or-miss operator* formalizes this idea. It is defined by

$$\Psi_{\mathrm{hm}}(F) = F \otimes (A, B) = \{h \in E \mid (A + h) \subseteq F \;\text{ and }\; (B + h) \subseteq F^c\},$$

where A and B are two structuring elements, such that $A \cap B = \emptyset$. This says that a point h lies in the hit-or-miss transformed set $F \otimes (A, B)$ if and only if the translated structuring element $A + h$ does not hit F^c (or, equivalently, it is contained in F) and the translated structuring element $B + h$ misses F (or, equivalently, it is contained in F^c). It can shown that

$$F \otimes (A, B) = (F \ominus A) \cap (F^c \ominus B).$$

Therefore, the hit-or-miss transformed set contains all points that simultaneously belong to the erosion of the foreground F by the structuring element A and the erosion of the background F^c by the structuring element B. Some properties of this operator are listed in Table 3.5. It is required that $A \cap B = \emptyset$, for the hit-or-miss operator not to result in an empty set. The hit-or-miss operator is well suited to the task of locating points inside an object with certain (local) geometric properties; e.g., isolated points, edge points, corner points, etc. (e.g., see [6, 56]).

The hit-or-miss operator leads to an extraordinary result, due to Banon and Barrera [12]: *any translation invariant set operator can be represented as a union of hit-or-miss operators.* This is clearly a more powerful result than the representation by a union of erosions (or an intersection of dilations), which is limited to the case of increasing and translation invariant operators.

To be formal, we first need two definitions. Given two sets A and B, the *interval* $[A, B]$ is the collection of all sets F such that $A \subseteq F \subseteq B$. Given a set operator Ψ, the *bi-kernel* $\mathcal{W}(\Psi)$ of Ψ is defined by

$$\mathcal{W}(\Psi) = \{(A, B) \mid [A, B] \subseteq \mathcal{K}(\Psi)\},$$

where $\mathcal{K}(\Psi)$ is the kernel of operator Ψ, defined by (3.12). Then, for any translation invariant set operator Ψ, we have that (e.g., see [6])

$$\Psi(F) \;=\; \bigcup_{(A,B)\in\mathcal{W}(\Psi)} F \otimes (A, B^c). \tag{3.15}$$

The design of binary morphological operators, based on the representation in (3.15), has been investigated in [57]. However, this approach often needs a large training set making its use in medical imaging applications difficult.

3.2.7 Morphological gradients

The set operator

$$\Psi_{\text{grad}}(F) = F \oplus B \setminus F \ominus B, \tag{3.16}$$

where B is a structuring element that contains the origin, is known as the *morphological gradient*. $\Psi_{\text{grad}}(F)$ is a “boundary peeler” that estimates the boundary of an object F. This operator is often used to obtain surface area estimates in 3D binary images. The result depends on the size and shape of the structuring element B and is less affected by boundary noise when compared to differential edge detectors.

By using variants of (3.16), it is possible to detect external or internal boundaries. Indeed, the *external morphological gradient* operator

$$\Psi^{+}_{\text{grad}}(F) = F \oplus B \setminus F$$

calculates the external boundary of an object F, whereas the *internal morphological gradient* operator

$$\Psi^{-}_{\text{grad}}(F) = F \setminus F \ominus B \tag{3.17}$$

calculates the internal boundary of F. Notice that

$$\Psi_{\text{grad}}(F) = \Psi^{+}_{\text{grad}}(F) \cup \Psi^{-}_{\text{grad}}(F).$$

The morphological gradient, and its external and internal variants, are always positive because dilations and erosions with structuring elements that contain the origin are extensive and anti-extensive, respectively. An illustration of the morphological gradient operators is depicted in Fig. 3.7. The *cross* structuring element $B_{\text{cr}} = \{(0,0), (-1,0), (1,0), (0,-1), (0,1)\}$, centered at the origin $(0,0)$, is used in this case. Notice that the internal gradient operator detects cellular boundaries correctly, whereas the gradient and the external gradient operators may connect the boundaries of some cells which are in close proximity to each other. For more information on morphological gradients the reader is referred to [58, 59].

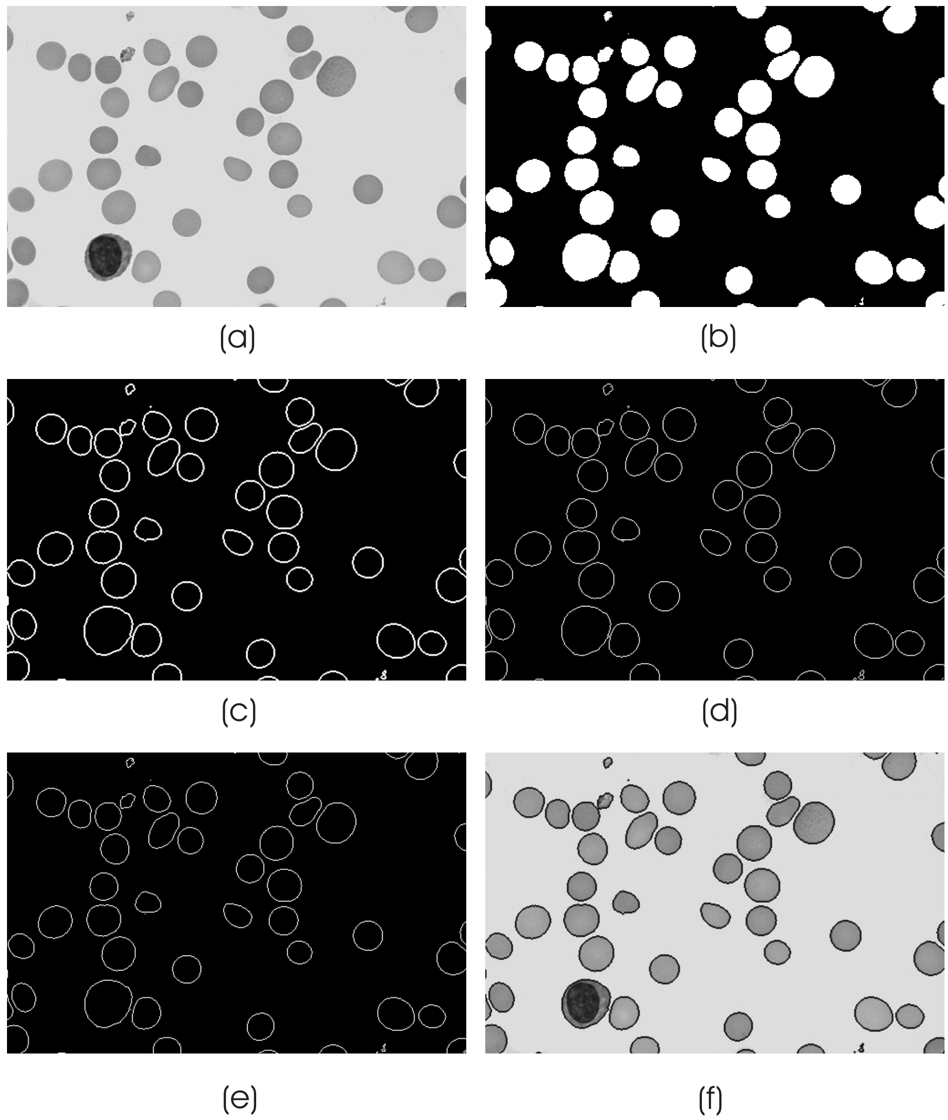

Figure 3.7: *Morphological gradients: (a) peripheral blood smear of a* 30 *year old anemic female with a diagnosis of hereditary spherocytosis; (b) original image after binarization; (c) gradient using the cross structuring element* B_{cr}*; (d) external gradient; (e) internal gradient; (f) gradient overlaid on the original grayscale image in (a). – Data courtesy of K. C. Klatt, Department of Pathology, University of Utah. Used with permission.*

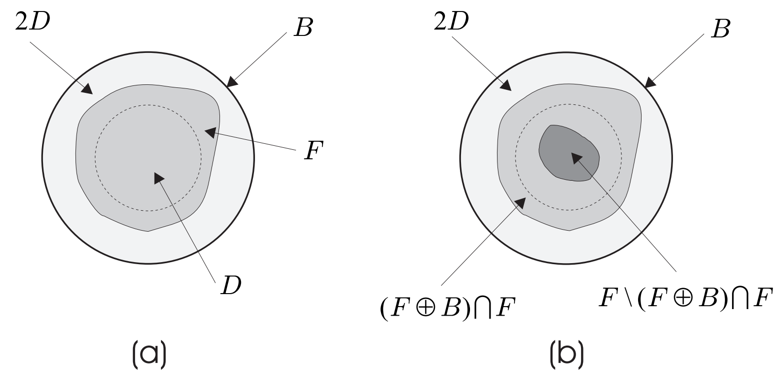

Figure 3.8: *(a) A grain F such that $D \subseteq F \subseteq \mathrm{int}(2D)$; (b) the internal marker $F \setminus (F \oplus B) \cap F$ obtained by means of an annular opening by the circular structuring element B.*

3.2.8 Conditional dilation

If an image is dilated by a structuring element that contains the origin, it is expanded. If this type of dilation is repeated indefinitely, the original image will grow out of bound. One way to avoid this problem is to restrict the dilation $F \oplus B$ within a *mask element* M. This defines a new type of (non-translation invariant) dilation, known as *conditional dilation*, given by

$$\Psi_\delta(F \mid M) = (F \oplus B) \cap M.$$

It will become clear in the following (see Section 3.6), that the conditional dilation plays a key role in defining a new morphological operator, known as opening by reconstruction, which turns-out to be very useful in object detection and segmentation problems.

3.2.9 Annular openings and closings

If B is a *symmetric* structuring element (i.e., if $\breve{B} = B$), which does not contain the origin, then the operator

$$\Psi_{\mathrm{anopn}}(F) = (F \oplus B) \cap F$$

defines an opening (i.e., it is increasing, anti-extensive, and idempotent). This is known as the *annular opening*. The dual

$$\Psi_{\mathrm{anclo}}(F) = (F \ominus B) \cup F$$

of an annular opening is a closing (i.e., an operator that is increasing, extensive, and idempotent), known as the *annular closing*.

The annular opening is a useful operator for marking grains in an image of a particular geometry and size. We illustrate this with an example. Given a grain F, let D be a disk of radius r such that $D \subseteq F \subseteq \mathrm{int}(2D)$, where $\mathrm{int}(2D)$ denotes the *interior* of $2D$, obtained by removing its boundary; see Fig. 3.8(a). Figure 3.8(b) depicts the result of the annular opening $(F \oplus B) \cap F$, where B is the boundary of $2D$ (i.e., it is a circle of radius $2r$). The set difference $F \setminus (F \oplus B) \cap F$ produces a hole punched through F. We use the result of this set difference as a marker for grain F. However, if $F \subset D$, $\Psi_{\mathrm{anopn}}(F) = \emptyset$ and, therefore, $F \setminus \Psi_{\mathrm{anopn}}(F) = F$, whereas, if $2D \subseteq F$, $\Psi_{\mathrm{anopn}}(F) = F$ and, therefore, $F \setminus \Psi_{\mathrm{anopn}}(F) = \emptyset$. In these two cases, F will not marked.

We now apply these observations to the problem of extracting normal blood cells from microscopic images of a blood smear. The image in Fig. 3.9(a) depicts the peripheral blood smear of a 29 year old female with a diagnosis of acute promyelocytic leukemia. Many fragmented red blood cells are evident, due to disseminated intravascular coagulation. The normal red blood cells have a zone of central pallor of about 1/3 of their size and demonstrate minimal variation in size (anisocytosis) and shape (poikilocytosis). An annular opening by a circular structuring element of appropriate size is expected to consistently punch a hole (marker) in the center of these cells. Red blood cells which are too large, too small due to fragmentation, or that are deformed, are not marked.

To achieve this, the image in Fig. 3.9(a) is first binarized by means of thresholding. However, the pallors of some of the red blood cells manifest themselves as holes after thresholding. To remove these holes, we apply an area closing operation, which eliminates holes with area smaller than 200 pixels. The result is depicted in Fig. 3.9(b). In order to avoid possible interference among cells in close proximity to each other, the grains are "shrunk" by means of an erosion by a disk structuring element with a diameter of 5 pixels. The resulting image is then processed by means of an annular opening with a circular structuring element with diameter of 35 pixels. The result is depicted in Fig. 3.9(c). Notice the presence of black holes within grains associated with normal blood cells. The holes that do not touch the boundary are extracted from the image in (c); see Fig. 3.9(d). This is done by means of an area closing, which fills-in the holes in image (c), from which the image in (c) is subtracted. The resulting markers are then used to identify the normal red blood cells, which are depicted in Fig. 3.9(e) as dark shapes overlaid on the original image in (a) (the reconstruction of the actual cell shape from the marker will be treated in Section 3.6). The remaining cells are depicted in Fig. 3.9(f). Notice that the cells in (f) are either fragmented, overlapping, or have irregular shape.

Additional information about annular openings and closings, and about a more general class of operators known as *annular filters*, may be found in [60].

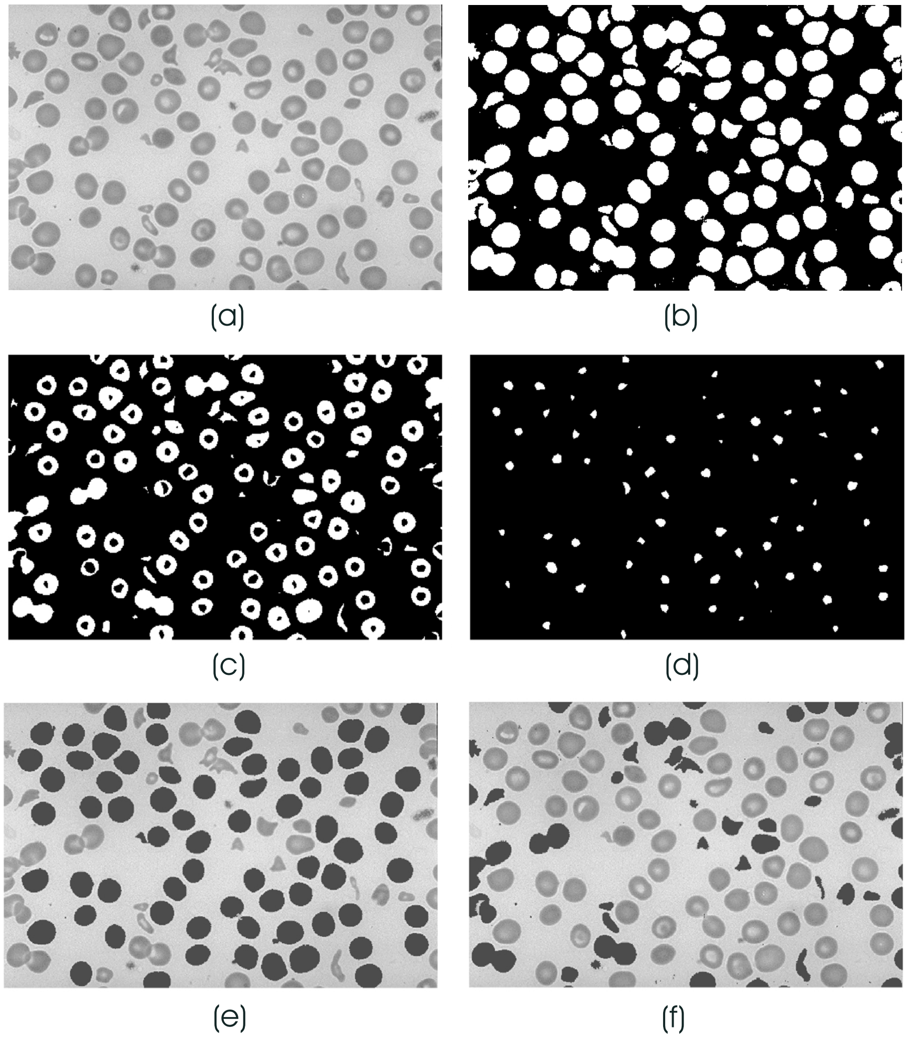

Figure 3.9: *Annular opening: (a) peripheral blood smear of a 29 year old female with a diagnosis of acute promyelocytic leukemia demonstrates many fragmented red blood cells due to disseminated intravascular coagulation; (b) original image after binarization and area closing; (c) annular opening by a circular structuring element; (d) normal red blood cell markers extracted from (c); (e) marked normal red blood cells overlaid on the original grayscale image in (a) (dark shapes); (f) marked fragmented, overlapping, and suspicious red blood cells overlaid on the original grayscale image in (a) (dark shapes). – Data courtesy of K. C. Klatt, Department of Pathology, University of Utah. Used with permission.*

3.2.10 Morphological filters

A set operator Ψ is said to be a binary *morphological filter*, if Ψ is increasing (i.e., $F_1 \subseteq F_2 \Rightarrow \Psi(F_1) \subseteq \Psi(F_2)$) and idempotent (i.e., $\Psi\Psi(F) = \Psi(F)$). Binary morphological filters are most frequently used to smooth object boundaries or to remove components from an image based on certain geometric properties. These operators are constrained to preserve order (i.e., they need to be increasing) and are required to remove components in a single application (i.e., they need to be idempotent). According to this definition, openings and closings are morphological filters, since they are increasing and idempotent. However, erosions and dilations are not morphological filters, since they are not idempotent.

We can build binary morphological filters from other binary morphological filters by composition (e.g., see [6, 61]). If Ψ_1 and Ψ_2 are two binary morphological filters, such that $\Psi_1 \subseteq \Psi_2$ or $\Psi_2 \subseteq \Psi_1$, then

$$\Psi_2\Psi_1, \quad \Psi_1\Psi_2, \quad \Psi_1\Psi_2\Psi_1, \quad \text{and} \quad \Psi_2\Psi_1\Psi_2$$

are binary morphological filters as well. Based on these compositions, the operators (recall that $F \circ B \subseteq F \bullet B$, for every structuring element B)

$$\Pi_k(F) = (F \circ kB) \bullet kB \quad \text{and} \quad P_k(F) = (F \bullet kB) \circ kB \tag{3.18}$$

where

$$kB = \begin{cases} \{\text{origin}\}, & \text{for} \quad k = 0 \\ B \oplus B \oplus \cdots \oplus B \ (k-1 \text{ dilations}), & \text{for} \quad k \geq 1 \end{cases}, \tag{3.19}$$

are binary morphological filters. In the literature, these filters are known as *alternating filters* (AF), since they alternate between opening and closing. The operators

$$\Sigma_k(F) = ((F \circ kB) \bullet kB) \circ kB \quad \text{and} \quad T_k(F) = ((F \bullet kB) \circ kB) \bullet kB$$

are binary morphological filters as well. Finally, we can compose alternating filters to form another class of binary morphological filters known as *alternating sequential filters* (ASF), given by

$$M_k(F) = \Pi_k\Pi_{k-1} \cdots \Pi_1(F) \quad \text{and} \quad N_k(F) = P_kP_{k-1} \cdots P_1(F).$$

Usually, the ASFs are more preferable in practice than the AFs. This is primarily due to the fact that, for a given value of k, an ASF filters-out shape components by gradually increasing the size of the structuring element, from B to kB, whereas an AF filters-out shape components by only applying the structuring element kB. Figure 3.10 depicts the results obtained by filtering the binary image of Fig. 3.3(b) with the AF Π_3, in (b), the morphological filter Σ_3, in (c), and the ASF M_3, in (d). In all cases, B is taken to be the cross structuring element. For more information on binary morphological filters, the reader is referred to [6, 54, 61–63].

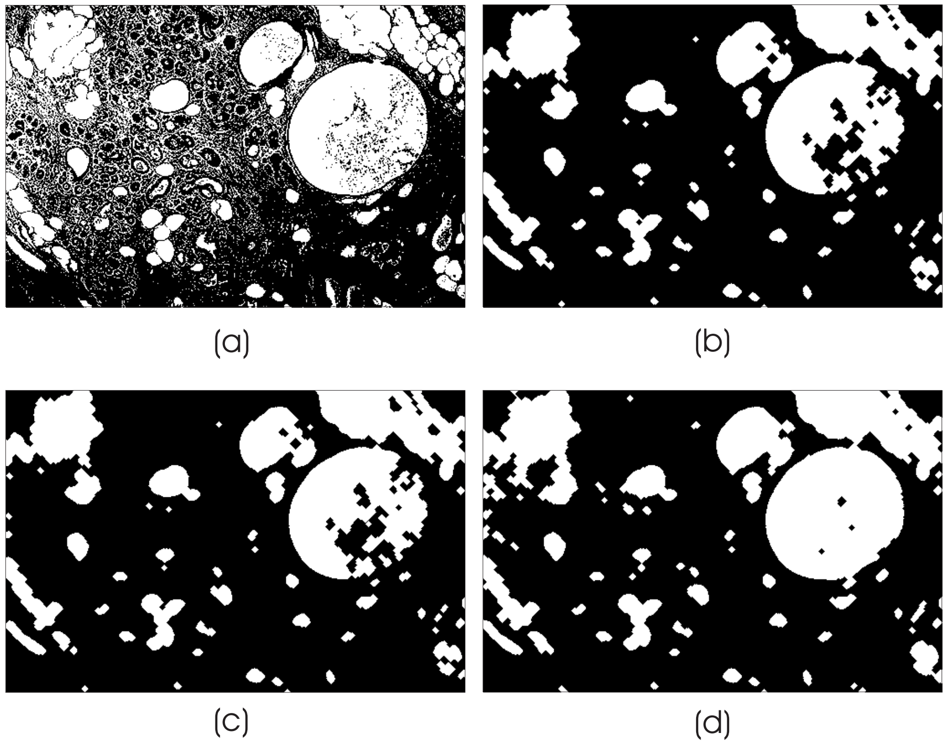

Figure 3.10: *Morphological filtering of the binary image depicted in Fig. 3.3(b): (a) original binary image; (b) filtering by the AF* Π_3*; (b) filtering by the morphological filter* Σ_3*; (d) filtering by the ASF* M_3*.*

3.3 Morphological representation of binary images

Image representation is a very important problem whose aim is to transform image data into a compact form so that information becomes easily accessible. Image representation can also lead to techniques for image description and compression. Although a large number of image representation techniques are available in the literature (e.g., techniques based on the Fourier transform or the wavelet transform [64]), mathematical morphology has produced some very useful techniques, especially for binary images. In this section, we discuss two of these techniques, namely the discrete size transform and the morphological skeleton. The reader is referred to [65–70] for more details on these subjects.

3.3.1 The discrete size transform

Given a binary image F, its *discrete size transform* (DST) is defined by

$$F \mapsto (..., D_{-k}(F;B), ..., D_{-1}(F;B), D_0(F;B), D_1(F;B), ..., D_k(F;B), ...),$$

where

$$D_k(F;B) = \begin{cases} F \circ kB \setminus F \circ (k+1)B, & \text{for } k = 0, 1, \ldots \\ F \bullet |k|\breve{B} \setminus F \bullet (|k|-1)\breve{B}, & \text{for } k = -1, -2, \ldots \end{cases},$$

with kB defined in (3.19). Notice that

$$F \circ (k+1)B \subseteq F \circ kB \quad \text{and} \quad F \bullet k\breve{B} \subseteq F \bullet (k+1)\breve{B},$$

for $k = 0, 1, \ldots$. Therefore, $D_k(F;B) \cap D_m(F;B) = \emptyset$, for $k \neq m$, and the DST is an *orthogonal* shape decomposition scheme, in the sense that it decomposes a binary image into disjoint components. Moreover,

$$F = \bigcup_{k \geq 0} D_k(F;B) = \left[\bigcup_{k \leq -1} D_k(F;B) \right]^c .$$

Therefore, the DST is an *invertible* image decomposition scheme as well (i.e., an image F can be uniquely reconstructed from the DST components $\{D_k(F;B), k \geq 0\}$ or $\{D_k(F;B), k \leq -1\}$).

When F consists of (nonoverlapping) grains F_i, $i = 1, 2, \ldots$, the opening $F \circ kB$, for $k \geq 0$, can be viewed as a *sieve* of mesh "width" k that allows only grains of "size" less than k to pass through. In this case, we may say that a grain F_i is of "size" k if $F_i \cap (F \circ kB) \neq \emptyset$, but $F_i \cap (F \circ (k+1)B) = \emptyset$. This leads to the observation that $\{F \circ kB, k \geq 0\}$ is a *multiresolution* image decomposition scheme which reduces resolution as k increases. However, the term "resolution" is not associated here to the frequency content of F, as is customary in linear multiresolution techniques (e.g., see [64]), but to its size content (see [66] for more details on this subject). Notice that the notion of size is directly related to the structuring element B used: a grain F_i of F is of "size" k if there exists at least one translated replica of kB that fits inside F_i, whereas there is no translated replica of $(k+1)B$ that fits inside F_i. Similar remarks hold for $\{F \bullet (|k|-1)\breve{B}, k \leq -1\}$, as it pertains to the holes of F.

Based on these remarks, it is now clear that the DST is a multiresolution image decomposition scheme in terms of successive differences of openings and closing with structuring elements of increasing size. For $k \geq 0$, the k^{th} component of the DST contains only grains that are of "size" k. On the other hand, for $k \leq -1$, the k^{th} component of the DST contains only holes that are of "size" k.

3.3.2 The pattern spectrum

The DST can be thought of as the morphological analogue of the Fourier transform. Both transforms decompose an image into orthogonal components that are sufficient for reconstructing the image under consideration. It

FOURIER SPECTRUM	PATTERN SPECTRUM
A smooth image is characterized by large values in the Fourier spectrum at low frequencies and small or zero values at high frequencies.	A shape with many large smooth objects and few or no small objects is characterized by large values in the higher part of the pattern spectrum and small or zero values in the lower part of the pattern spectrum.
An image with fast grayscale variation is characterized by small or zero values in the Fourier spectrum at low frequencies and large values at high frequencies.	A shape with many small rough objects and no large smooth objects is characterized by small or zero values in the higher part of the pattern spectrum and large values in the lower part of the pattern spectrum.
The Fourier spectrum is a histogram of the distribution of complex sinusoids representing an image.	The pattern spectrum is a histogram of the distribution of the sizes of various objects representing an image.
The original image cannot be recovered from only the Fourier spectrum – knowledge of the phase spectrum is also needed.	The original image cannot be recovered from its pattern spectrum.

Table 3.6: *A comparison of the Fourier spectrum and the pattern spectrum.*

is quite common, in Fourier-based image processing and analysis techniques, to characterize images by means of the magnitude of the Fourier transform, known as the *Fourier spectrum*, while discarding phase information. A similar approach applies in the morphological case as well. An image is characterized by the "magnitude" of the DST, known as the *pattern spectrum*, given by

$$P_{F;B}(k) = |D_k(F;B)| = \begin{cases} |F \bigcirc kB \setminus F \bigcirc (k+1)B|, & \text{for } k \geq 0 \\ |F \bullet |k|\breve{B} \setminus F \bullet (|k|-1)\breve{B}|, & \text{for } k \leq -1 \end{cases},$$

where $|A|$ is the area (or cardinality) of set A. Notice that the pattern spectrum depends on the particular structuring element B used (i.e., for a given image, different pattern spectra can be obtained for different structuring elements).

As in the case of the Fourier spectrum, the information conveyed by the pattern spectrum of an image F is not sufficient for reconstructing F. However, the pattern spectrum conveys some useful information regarding the shape-size content of a binary image. For example:

(a) The boundary roughness of F, relative to the structuring element B, appears in the lower part of the pattern spectrum, for a rough boundary, and in the higher part of the pattern spectrum, for a smooth boundary.

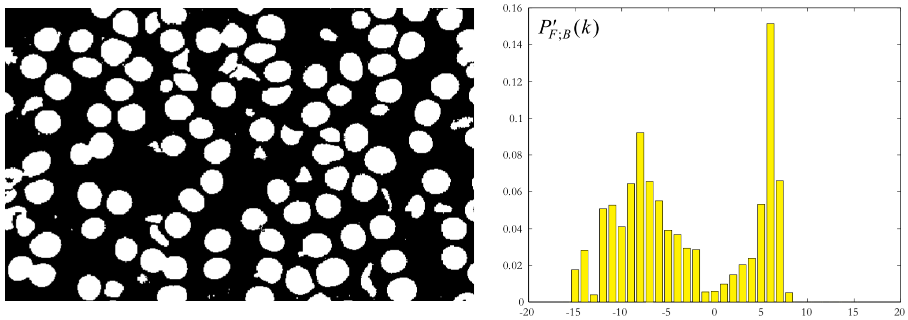

Figure 3.11: *The (normalized) pattern spectrum* $P'_{F;B}(k)$ *of a binary image. Notice that the large peak at size* 6 *indicates the prominent presence of particles of size* 6.

(b) Long capes or bulky protruding parts in F of pattern B show-up as isolated impulses or jumps at the positive sizes of the pattern spectrum.

(c) Big jumps at negative sizes illustrate the existence of prominent intruding gulfs or holes in F.

All these properties are the morphological analogues of similar properties of the Fourier spectrum. Table 3.6 summarizes similarities between the Fourier and the pattern spectra. Figure 3.11 depicts the (normalized) pattern spectrum of the binary image in Fig. 3.9(b), with the structuring element being a disk of diameter 3. Normalization produces a pattern spectrum $P'_{F;B}(k)$ from $P_{F;B}(k)$, such that $\sum_{k=-\infty}^{\infty} P'_{F;B}(k) = 1$. Notice that the large peak at size 6 indicates the prominent presence of particles of size 6.

The pattern spectrum is frequently used as a shape/size descriptor. It has been employed in a number of image processing and analysis tasks, such as shape and texture analysis [5], multiscale shape representation [66], morphological shape filtering and restoration [71–74], and analysis, segmentation, and classification of texture [74–82]. Its computation however may be time consuming. A number of efficient algorithms have been proposed in the literature for dealing with this problem (e.g., see [83, 84]).

3.3.3 The morphological skeleton transform

The (Euclidean) *skeleton* of a shape is a thin caricature, obtained by creating an archetypal stick figure that internally locates the central axis of the shape. This structure was first introduced by Blum [85], who called it the "medial axis." The skeleton is a binary image representation technique that summarizes a shape and conveys useful information about its size, orientation, and connectivity [86].

To define the skeleton of a shape F, for each point $h \in F$, let $D(h)$ denote the largest disk centered at h such that $D(h) \subseteq F$. Then, the point

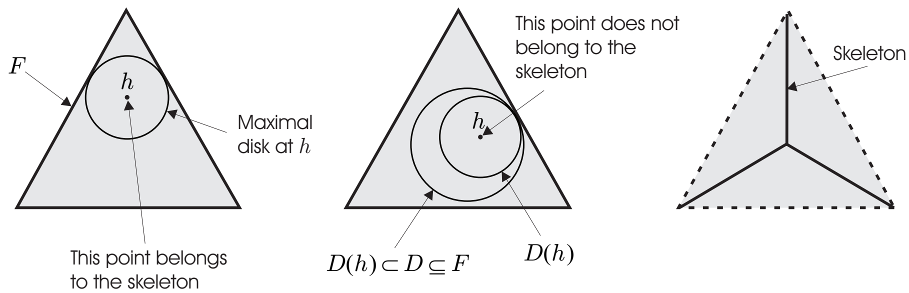

Figure 3.12: *Construction of the (Euclidean) skeleton for a triangular shape.*

h is a point on the skeleton of F if there does not exist a disk D, such that $D(h) \subset D \subseteq F$. In this case, $D(h)$ is called the *maximal disk* located at point h. This is illustrated in Fig. 3.12. If, in addition to the skeleton, the radii of the maximal disks located at all points h on the skeleton of a shape F are known, then F can be uniquely reconstructed from this information as the union of all such maximal disks. Therefore, the skeleton, together with the radius information associated with the maximal disks, contain enough information to uniquely reconstruct the original shape.

In 1977, Lantuéjoul showed that, if $\sigma(F)$ is the skeleton of a shape F (a set that contains all points of the skeleton of F), then:

$$\sigma(F) = \bigcup_{r>0} \sigma_r(F),$$

where

$$\sigma_r(F) = F \ominus rB \setminus (F \ominus rB) \circ drB, \tag{3.20}$$

with B being a disk of radius 1 (see [5]). In this case, rB is a disk of radius r and drB is a disk of an infinitesimal radius dr. The set $\sigma_r(F)$ contains the centers of all maximal disks of radius r. Since shape F equals the union of all maximal disks, we have that

$$F = \bigcup_{r>0} \sigma_r(F) \oplus rB.$$

Equation (3.20) can be discretized, by setting $r = kdr$, and $dr = 1$, for some integer k. In this case, $rB = kB = B \oplus B \oplus \cdots \oplus B$ ($k-1$ dilations). If we also replace disk B with an arbitrary structuring element, then we get the so-called morphological skeleton transform of F.

The *morphological skeleton transform* of a binary image F is given by:

$$F \mapsto (S_0(F;B), S_1(F;B), \ldots, S_k(F;B), \ldots),$$

where

$$S_k(F;B) = F \ominus kB \setminus (F \ominus kB) \circ B,$$

with kB given by (3.19). The set $S_k(F;B)$ is called the *skeleton subset of order* k. The union

$$S(F;B) = \bigcup_{k \geq 0} S_k(F;B)$$

is called the *morphological skeleton* of F. When B is a disk structuring element, then $S(F;B)$ is a discrete approximation of the skeleton of F. When B contains the origin,

$$F \ominus kB \supseteq (F \ominus kB) \circ B \supseteq F \ominus (k+1)B,$$

for $k = 0, 1, \ldots$. In this case,

$$S_k(F;B) \cap S_m(F;B) = \emptyset, \quad \text{for} \quad k \neq m,$$

and the morphological skeleton transform is an *orthogonal* shape decomposition scheme. Furthermore,

$$F = \bigcup_{k \geq 0} S_k(F;B) \oplus kB, \tag{3.21}$$

making the morphological skeleton transform *invertible*.

The morphological skeleton transform can be uniquely represented by a grayscale image $s_B(x,y)$, known as the *skeleton function*, given by

$$s_B(x,y) = \begin{cases} k, & \text{if } (x,y) \in S_k(F;B) \\ -\infty, & \text{if } (x,y) \notin S(F;B) \end{cases}.$$

Notice that

$$S_k(F;B) = \{(x,y) \in E \mid s_B(x,y) = k\}. \tag{3.22}$$

Therefore, image F can be uniquely reconstructed from the skeleton function $s_B(x,y)$, by means of (3.21) and (3.22). The skeleton function has been used for image compression and coding [65]. Moreover, the morphological skeleton transform has been used for shape analysis and recognition. Efficient algorithms for computing skeleton transforms can be found in [83, 87].

Figure 3.13 depicts an example of the morphological skeleton, by using the cross structuring element B_{cr}. Figure 3.13(a) depicts the morphological skeleton of the binary image F of Fig. 3.7(b), superimposed on F. Notice that individual grains can be compressed to small and thin line segments emanating from the center of the grains. On the other hand, Fig. 3.13(b) depicts the morphological skeleton of the complement image F^c, superimposed on F. In this case, the morphological skeleton may be used to segment the image into nonoverlapping partitions, each containing a grain. However, it is clear from the result depicted in Fig. 3.13(b) that the morphological skeleton may not produce partitions with connected boundaries. The morphological skeleton of the complement F^c of a shape F is sometimes referred to as the *exoskeleton*.

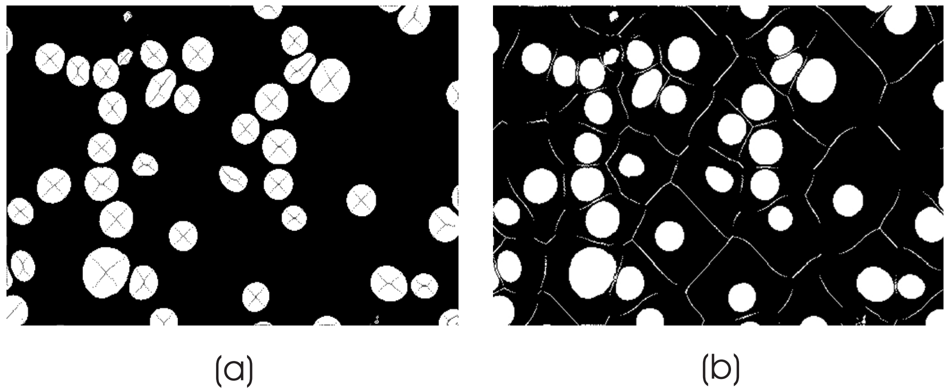

Figure 3.13: *Binary morphological skeleton using the cross structuring element B_{cr}: (a) skeleton of the binary image F depicted in Fig. 3.7(b), superimposed on F; (b) skeleton of the complement F^c, superimposed on F.*

3.4 Grayscale morphological operators

In order to extend mathematical morphology to the grayscale case, we need to combine grayscale images in a way that is compatible with unions and intersections. This is because a binary image is a special case of a grayscale image, when the number of gray levels is two. The tool that allows us to accomplish this task is known as threshold decomposition. Using threshold decomposition, we can show that the grayscale analogues of union and intersection are the operations of supremum and infimum, respectively. Using this observation, the extension of many binary morphological operators to the grayscale case is most often straightforward.

3.4.1 Threshold decomposition

Given a grayscale image $f(x, y)$, we define its *cross section* $F(t)$ at level t by

$$F(t) = \{(x, y) \in E \mid f(x, y) \geq t\}.$$

The collection $\mathcal{F} = \{F(t) \mid t \in \mathbb{R}, F(t) \neq \emptyset\}$ of all non-empty cross sections is known as the *threshold decomposition* of f. An image f is uniquely characterized by its threshold decomposition, since

$$f(x, y) = \bigvee \{t \in \mathbb{R} \mid (x, y) \in F(t)\},$$

at every pixel (x, y). Figure 3.14 depicts two cross sections of a 1D signal f for a high and a low value of the threshold t. Notice that, as t increases, $F(t)$ decreases. In particular, if $t_1 \geq t_2$, then $F(t_1) \subseteq F(t_2)$. This is known as the *stacking property*.

An image f has a unique threshold decomposition $\mathcal{F}$. However, given a collection $\mathcal{F} = \{F(t) \mid t \in \mathbb{R}, F(t) \neq \emptyset\}$ of non-empty sets, there might not

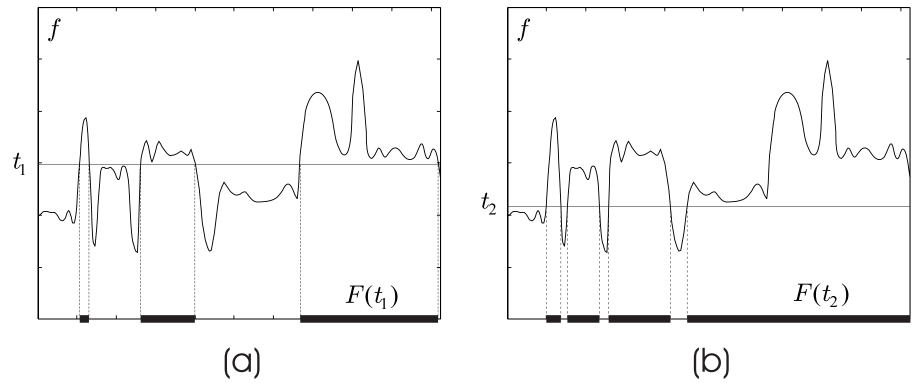

Figure 3.14: *Threshold decomposition of a grayscale function $f(x)$ into its cross sections $F(t)$: (a) cross section $F(t_1)$ for a high value t_1 of t; (b) cross section $F(t_2)$ for a low value t_2 of t.*

exist an image f with threshold decomposition $\mathcal{F}$. This is because the cross sections of an image f should satisfy the stacking property.

Threshold decomposition provides a useful link between grayscale and binary images. This link is used as a way to combine grayscale images that is compatible with mathematical morphology, by means of the following three steps:

1. Calculate the threshold decompositions $\mathcal{F}_1$, $\mathcal{F}_2$ of images f_1 and f_2, respectively.

2. Generate the threshold decomposition
$$\mathcal{F} = \{F(t) = F_1(t) \cup F_2(t) \mid t \in \mathbb{R}, F(t) \neq \emptyset\}.$$

3. Set
$$f(x, y) = \bigvee \{t \in \mathbb{R} \mid (x, y) \in F(t)\}.$$

It is not difficult to see that:
$$f(x, y) = f_1(x, y) \vee f_2(x, y) = (f_1 \vee f_2)(x, y).$$

Alternatively, we may combine two images f_1 and f_2 by means of the following three steps:

1. Calculate the threshold decompositions $\mathcal{F}_1$, $\mathcal{F}_2$ of images f_1 and f_2, respectively.

2. Generate the threshold decomposition
$$\mathcal{F} = \{F(t) = F_1(t) \cap F_2(t) \mid t \in \mathbb{R}, F(t) \neq \emptyset\}.$$

3. Set
$$f(x,y) = \bigvee\{t \in \mathbb{R} \mid (x,y) \in F(t)\}.$$

In this case,
$$f(x,y) = f_1(x,y) \wedge f_2(x,y) = (f_1 \wedge f_2)(x,y).$$

Evidently, the grayscale analogues of union and intersection are the pixelwise supremum and infimum, respectively. It is also true that
$$f_1 \leq f_2 \quad \Leftrightarrow \quad F_1(t) \subseteq F_2(t), \quad \text{for every } t \in \mathbb{R}.$$

Therefore, the grayscale analogue of set inclusion is for a grayscale image f_1 to be smaller than another image f_2 (i.e., $f_1 \leq f_2$), in the sense that $f_1(x,y) \leq f_2(x,y)$, at every pixel (x,y).

Additional information about threshold decomposition can be found in [88].

3.4.2 Increasing and translation invariant operators

As we said before, the most elementary operators of interest to mathematical morphology are increasing and translation invariant. A grayscale image operator ψ is said to be *increasing*, if $f_1 \leq f_2$ implies that $\psi(f_1) \leq \psi(f_2)$. On the other hand, if $f_{x_0,y_0}(x,y)$ denotes the spatially translated image $f(x-x_0, y-y_0)$, then a grayscale image operator ψ is *spatially translation invariant* if
$$\psi(f_{x_0,y_0})(x,y) = \psi(f)(x-x_0, y-y_0),$$
for every space translation (x_0, y_0). If $(f+v)(x,y)$ denotes the grayscale translated image $f(x,y)+v$, then a grayscale image operator ψ is *grayscale translation invariant* if
$$\psi(f+v)(x,y) = \psi(f)(x,y) + v.$$

Notice that, here, we are dealing with two types of translation invariance, spatial and grayscale, as opposed to the binary case where we only deal with spatial translation invariance. In the grayscale case, when we speak about translation invariance, we mean both spatial and grayscale translation invariance.

When f is real-valued, the *negative image* f^* of f is defined by
$$f^*(x,y) = -f(x,y). \tag{3.23}$$

When f takes finite values in $\{0,1,\ldots,G\}$, the negative image f^* of f is defined by
$$f^*(x,y) = G - f(x,y).$$

Notice that, when $G = 1$ (i.e., in the case of binary images), f^* is the set-complement. Finally, a grayscale image operator ψ is *anti-extensive*, if $\psi(f) \leq f$, *extensive*, if $\psi(f) \geq f$, and *idempotent*, if $\psi\psi(f) = \psi(f)$.

3.4.3 Erosion and dilation

As in the binary case, where it is opted to use operators that distribute over unions and intersections, it is desirable to deal with grayscale image operators which distribute over suprema and infima. Any image operator ψ_ϵ such that $\psi_\epsilon(f_1 \wedge f_2) = \psi_\epsilon(f_1) \wedge \psi_\epsilon(f_2)$, for every pair (f_1, f_2) of grayscale images, is called a grayscale erosion. Any image operator ψ_δ such that $\psi_\delta(f_1 \vee f_2) = \psi_\delta(f_1) \vee \psi_\delta(f_2)$, for every pair (f_1, f_2) of grayscale images, is called a grayscale dilation. As a direct consequence of these definitions, both grayscale erosion and dilation are increasing operators.

When the grayscale erosion is translation invariant, then

$$\begin{aligned}\psi_\epsilon(f)(x,y) &= \bigwedge_{\xi,\eta}[f(x+\xi, y+\eta) - b(\xi,\eta)] \\ &= \bigwedge_{\xi,\eta}[f(\xi,\eta) - b(\xi - x, \eta - y)] \\ &= (f \ominus b)(x,y),\end{aligned}$$

where b is a grayscale image known as the *structuring function* (e.g., see [6]). In the special case when

$$b(x,y) = \begin{cases} 0, & \text{for } (x,y) \in B \\ -\infty, & \text{otherwise} \end{cases}, \tag{3.24}$$

for some structuring element B, then

$$\psi_\epsilon(f)(x,y) = \bigwedge_{(\xi,\eta)\in B} f(x+\xi, y+\eta).$$

This is called *flat* (grayscale) *erosion*, and is denoted (with a slight abuse of notation) by $f \ominus B$. A structuring function of the form (3.24) is usually referred to as a *flat structuring function*. The flat erosion replaces the value of an image f at a pixel (x,y) by the infimum of the values of f over a structuring element B. Some properties of the grayscale erosion are summarized in Table 3.7. In this table, $\breve{b}(x,y) = b(-x,-y)$ is the *reflection* of the structuring function b around the origin. An example of a flat grayscale erosion is depicted in Fig. 3.15.

When the grayscale dilation is translation invariant, then

$$\begin{aligned}\psi_\delta(f)(x,y) &= \bigvee_{\xi,\eta}[f(x-\xi, y-\eta) + b(\xi,\eta)] \\ &= \bigvee_{\xi,\eta}[f(\xi,\eta) + b(x-\xi, y-\eta)] \\ &= (f \oplus b)(x,y),\end{aligned}$$

$(f_{x_0,y_0} \ominus b)(x,y) = (f \ominus b_{-x_0,-y_0})(x,y)$ $= (f \ominus b)(x-x_0, y-y_0)$	Spatial translation invariance
$(f+v) \ominus b = f \ominus (b-v) = (f \ominus b) + v$	Grayscale translation invariance
$f \ominus b_1 \geq f \ominus b_2$ if $b_1 \leq b_2$	Decreasingness with respect to structuring function
$f \ominus (b_1 \vee b_2) = (f \ominus b_1) \wedge (f \ominus b_2)$	Parallel composition
$(f_1 \wedge f_2) \ominus b = (f_1 \ominus b) \wedge (f_2 \ominus b)$	Distributivity of minimum
$f \ominus (b_1 \wedge b_2) \geq (f \ominus b_1) \vee (f \ominus b_2)$	Parallel composition inequality
$(f_1 \vee f_2) \ominus b \geq (f_1 \ominus b) \vee (f_2 \ominus b)$	Parallel composition inequality
$(f \ominus b_1) \ominus b_2 = f \ominus (b_1 \oplus b_2)$	Serial composition
$f_1 \leq f_2 \Rightarrow f_1 \ominus b \leq f_2 \ominus b$	Increasingness with respect to image
$f \ominus b \leq f$ if $b(0) \geq 0$	Anti-extensitivity
$f \ominus b = (f^* \oplus \breve{b})^*$	Duality

Table 3.7: *Some properties of grayscale erosion.*

for some structuring function b. In the special case where b is "flat," then

$$\psi_\delta(f)(x,y) = \bigvee_{(\xi,\eta)\in B} f(x-\xi, y-\eta).$$

This is called *flat* (grayscale) *dilation*, and is denoted by $f \oplus B$. The flat dilation replaces the value of an image f at a pixel (x,y) by the supremum of the values of this function over a structuring element $\breve{B}$. Some properties of the grayscale dilation operator are summarized in Table 3.8. An example of a flat grayscale dilation is depicted in Fig. 3.16. For a geometric interpretation of flat grayscale erosions and dilations, the reader is referred to Subsection 3.4.7 below.

3.4.4 Representational power of erosions and dilations

Matheron's representation theorem can be extended to the grayscale case as well. In this case, every translation invariant and increasing operator ψ can be expressed as a supremum of erosions or infimum of dilations; i.e.,

$$\psi(f) \;=\; \bigvee_{b\in\mathcal{K}(\psi)} f \ominus b \;=\; \bigwedge_{b\in\mathcal{K}(\psi^*)} f \oplus \breve{b},$$

where $\mathcal{K}(\psi)$ is the *kernel* of operator ψ, defined by

$$\mathcal{K}(\psi) = \{b \mid \psi(b)(0,0) \geq 0\},$$

and ψ^* is the *dual* of operator ψ, given by $\psi^*(f) = [\psi(f^*)]^*$ (e.g., see [6]).

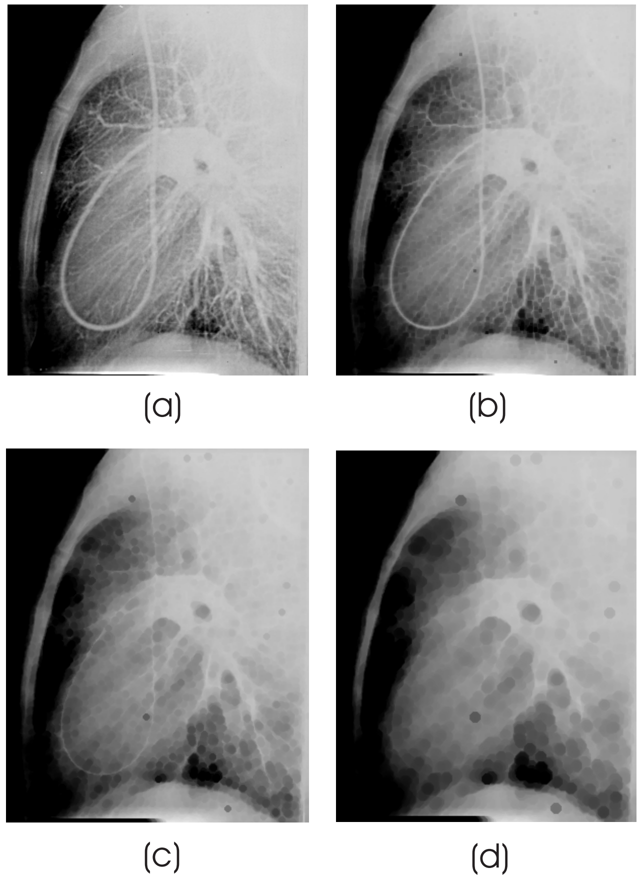

Figure 3.15: *Flat grayscale erosion: (a) original grayscale image of a lateral pulmonary artery angiogram; (b)–(d) flat erosions by a disk structuring element with a diameter of* 3, 7, *and* 11 *pixels, respectively. – Data courtesy of the University of Washington Digital Anatomist Program. Used with permission.*

3.4.5 Opening and closing

As in the binary case, an image operator ψ that is increasing ($f_1 \leq f_2 \Rightarrow \psi(f_1) \leq \psi(f_2)$), anti-extensive ($\psi(f) \leq f$), and idempotent ($\psi\psi(f) = \psi(f)$) is called an opening. On the other hand, an image operator that is increasing, extensive ($\psi(f) \geq f$) and idempotent is called a closing.

A popular (translation invariant) grayscale opening of an image f by a structuring function b is given by $f \bigcirc b = (f \ominus b) \oplus b$. We refer to this operator as the (grayscale) *structural opening*, since it involves a structuring function b. This is a smoothing filter that approximates an image from below, since $f \bigcirc b \leq f$. The amount and type of smoothing is determined by the shape and size of the selected structuring function. The structural opening attempts to

$f \oplus b = b \oplus f$	Commutativity
$(f_{x_0,y_0} \oplus b)(x,y) = (f \oplus b_{x_0,y_0})(x,y)$ $= (f \oplus b)(x - x_0, y - y_0)$	Spatial translation invariance
$(f + v) \oplus b = f \oplus (b + v) = (f \oplus b) + v$	Grayscale translation invariance
$f \oplus b_1 \leq f \oplus b_2$ if $b_1 \leq b_2$	Increasingness with respect to structuring element
$f \oplus (b_1 \vee b_2) = (f \oplus b_1) \vee (f \oplus b_2)$	Parallel composition
$(f_1 \vee f_2) \oplus b = (f_1 \oplus b) \vee (f_2 \oplus b)$	Distributivity of maximum
$f \oplus (b_1 \wedge b_2) \leq (f \oplus b_1) \wedge (f \oplus b_2)$	Parallel composition inequality
$(f \oplus b_1) \oplus b_2 = f \oplus (b_1 \oplus b_2)$	Serial composition
$f_1 \leq f_2 \Rightarrow f_1 \oplus b \leq f_2 \oplus b$	Increasingness with respect to image
$f \oplus b \geq f$ if $b(0) \geq 0$	Extensitivity
$f \oplus b = (f^* \ominus \breve{b})^*$	Duality

Table 3.8: *Some properties of grayscale dilation.*

undo the effect of erosion $f \ominus b$ by applying the associated dilation $(f \ominus b) \oplus b$. Some properties of the grayscale structural opening are summarized in Table 3.9. When b is a flat structuring function (i.e., when b is given by (3.24)), then the structural opening is referred to as a *flat* structural opening and is denoted by $f \bigcirc B$. An example of a flat structural opening is depicted in Fig. 3.17. Notice that, as the size of the structuring element increases, certain bright features are eliminated from the image.

Similarly, a popular (translation invariant) grayscale closing of an image f with a structuring function b is given by $f \bullet b = (f \oplus b) \ominus b$. We refer to this operator as the (grayscale) *structural closing.* This is a smoothing filter that approximates a shape from above, since $f \bullet b \geq f$. The amount and type of smoothing is determined by the shape and size of the structuring function used. The structural closing attempts to undo the effect of dilation $f \oplus b$ by applying the associated erosion $(f \oplus b) \ominus b$. Some properties of the structural grayscale closing are summarized in Table 3.9. When b is a flat structuring function, then the structural closing is referred to as a *flat* structural closing and is denoted by $f \bullet B$. An example of a flat structural closing is depicted in Fig. 3.18. For a geometric interpretation of flat grayscale openings and closings, refer to Subsection 3.4.7 below.

Another useful opening is the so-called *grayscale area opening.* This operator removes grains from the cross sections of a grayscale image with area below a given value. Mathematically, a grayscale area opening is expressed

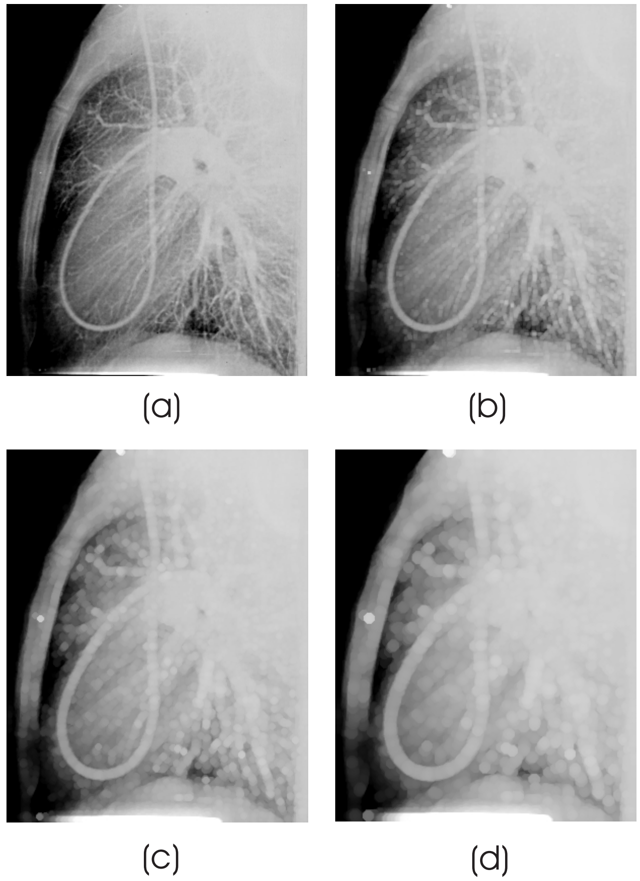

Figure 3.16: *Flat grayscale dilation: (a) original grayscale image of a lateral pulmonary artery angiogram; (b)–(d) flat dilations by a disk structuring element with a diameter of* 3, 7, *and* 11 *pixels, respectively. – Data courtesy of the University of Washington Digital Anatomist Program. Used with permission.*

by

$$\psi_{\text{areaopn}}(f, \alpha)(x, y) = \bigvee \{t \in \mathbb{R} \mid (x, y) \in \bigcup \{F_i(t) \mid |F_i(t)| \geq \alpha\}\}, \quad (3.25)$$

where $\{F_i(t) \mid i = 1, 2, \ldots\}$ are the grains of the cross section $F(t)$ of image f. It is not difficult to see that, for a fixed value of α, this operator is increasing, anti-extensive, and idempotent; therefore, it is an opening.

By duality, the *grayscale area closing* is defined as follows:

$$\psi_{\text{areaclo}}(f, \alpha) = [\psi_{\text{areaopn}}(f^*, \alpha)]^*,$$

where f^* is defined in (3.23). This operator fills-in the holes of the cross sections $F(t)$ of image f, whose area is strictly smaller than α. Efficient

$(f_{x_0,y_0} \circ b)(x,y) = (f \circ b)(x-x_0, y-y_0)$ $(f_{x_0,y_0} \bullet b)(x,y) = (f \bullet b)(x-x_0, y-y_0)$	Spatial translation invariance
$(f+v) \circ b = (f \circ b) + v$ $(f+v) \bullet b = (f \bullet b) + v$	Grayscale translation invariance
$f_1 \leq f_2 \Rightarrow f_1 \circ b \leq f_2 \circ b$ $f_1 \leq f_2 \Rightarrow f_1 \bullet b \leq f_2 \bullet b$	Increasingness with respect to image
$f \circ b \leq f$	Anti-extensitivity
$f \leq f \bullet b$	Extensitivity
$(f \circ b) \circ b = f \circ b$ $(f \bullet b) \bullet b = f \bullet b$	Idempotence
$f \circ b = (f^* \bullet \breve{b})^*$	Duality

Table 3.9: *Some properties of grayscale structural opening and closing.*

algorithms for the implementation of grayscale area openings and closings can be found in [89].

An example, illustrating the grayscale area opening operator, is depicted in Fig. 3.19. The blood smear, depicted in the first row of Fig. 3.19(a), is to be binarized in order to obtain the regions occupied by individual cells. The second row of Fig. 3.19(a) depicts the result of such a binarization. Due to the fact that blood cells have a zone of central pallor, which produces the bright regions within each cell, the result of binarization is not satisfactory: most cells produce a region filled with a black hole. Area opening can be effectively used to ameliorate this problem. This is evident from the results depicted in Figs. 3.19(b),(c). As the value of α, in (3.25), increases, the bright regions within each cell are effectively suppressed and binarization produces a more acceptable result.

3.4.6 Representational power of structural openings and closings

For a collection ψ_i of openings, $\psi = \bigvee_i \psi_i$ is an opening as well; i.e., the supremum of openings is also an opening. On the other hand, if ψ_i is a collection of closings, then $\psi = \bigwedge_i \psi_i$ is a closing as well; i.e., the infimum of closings is also a closing. This simple observation is very useful in practice, since it allows the design of grayscale openings and closings by taking the supremum, or infimum, of elementary grayscale openings or closings, respectively.

It can be shown (e.g., see [6]) that any translation invariant grayscale opening ψ_{opn} (i.e., a translation invariant operator that is increasing, anti-extensive, and idempotent) can be written as a supremum of grayscale structural openings, whereas any translation invariant grayscale closing ψ_{clo} (i.e., a translation invariant operator that is increasing, extensive, and idempo-

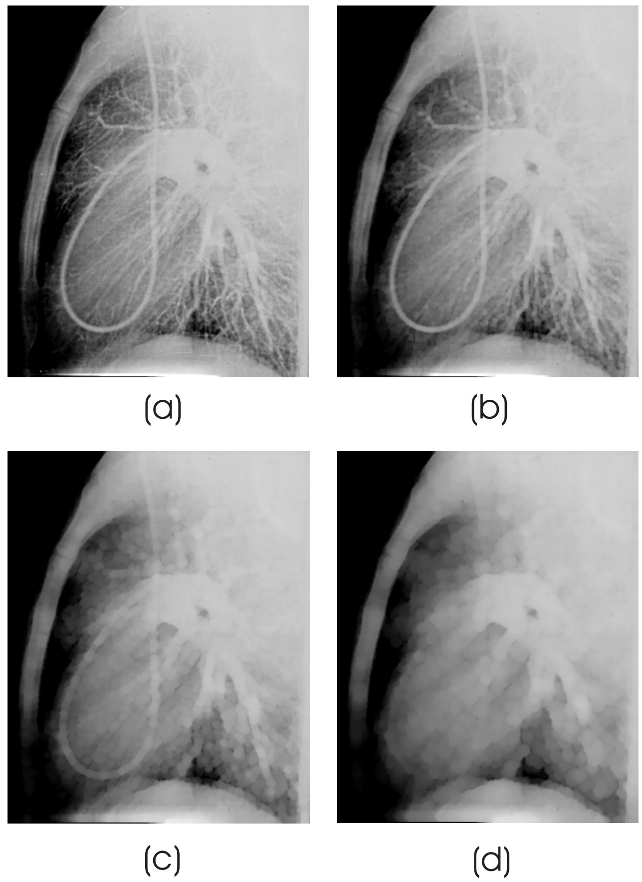

Figure 3.17: *Flat structural opening: (a) original grayscale image of a lateral pulmonary artery angiogram; (b)–(d) structural openings by a disk structuring element with a diameter of* 3*,* 7*, and* 11 *pixels, respectively. – Data courtesy of the University of Washington Digital Anatomist Program. Used with permission.*

tent) can be written as an infimum of grayscale structural closings; i.e.,

$$\psi_{\text{opn}}(f) = \bigvee_{b \in \text{Inv}(\psi_{\text{opn}})} f \circ b \quad \text{and} \quad \psi_{\text{clo}}(f) = \bigwedge_{b \in \text{Inv}(\psi_{\text{clo}})} f \bullet (\breve{b})^*,$$

where $\text{Inv}(\psi)$ denotes the *invariance domain* of the grayscale operator ψ, given by $\text{Inv}(\psi) = \{f \mid \psi(f) = f\}$.

3.4.7 Flat image operators

Threshold decomposition is used as an effective tool for building grayscale image operators from increasing binary image operators. Indeed, consider a grayscale image f. After applying threshold decomposition, we obtain the

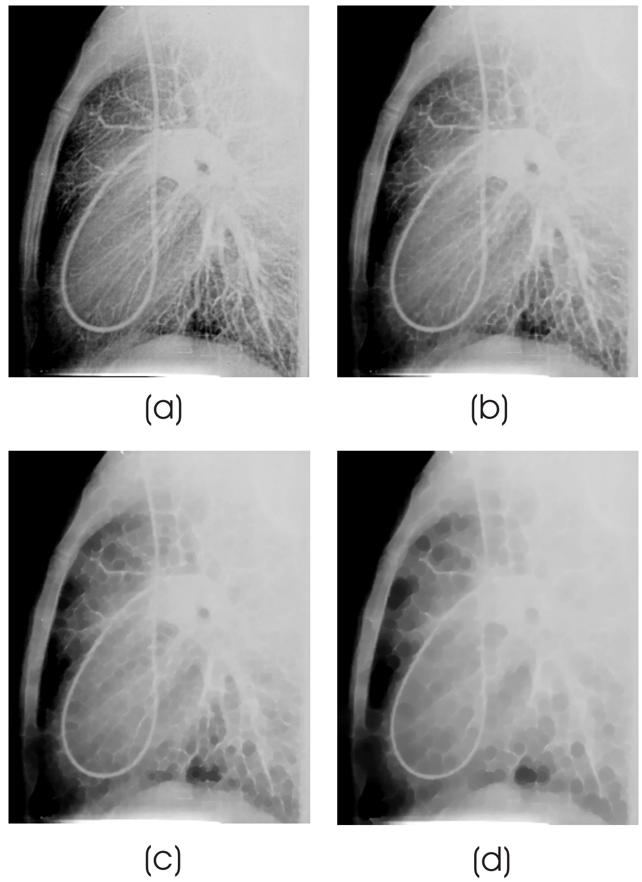

Figure 3.18: *Flat structural closing: (a) original grayscale image of a lateral pulmonary artery angiogram; (b)–(d) structural closing by a disk structuring element with a diameter of* 3, 7, *and* 11 *pixels, respectively. – Data courtesy of the University of Washington Digital Anatomist Program. Used with permission.*

cross sections $\mathcal{F} = \{F(t) \mid t \in \mathbb{R}, F(t) \neq \emptyset\}$. Now, consider an increasing set operator Ψ. For every t, apply this set operator on the cross section $F(t)$ in order to obtain a cross section $G(t)$. Since Ψ is increasing, we have that (recall the stacking property)

$$t_1 \geq t_2 \Rightarrow F(t_1) \subseteq F(t_2) \Rightarrow G(t_1) = \Psi(F(t_1)) \subseteq \Psi(F(t_2)) = G(t_2).$$

Clearly, the collection $\mathcal{G} = \{G(t) \mid t \in \mathbb{R}, G(t) \neq \emptyset\}$ of the resulting cross sections satisfies the stacking property. Therefore, $\mathcal{G}$ defines a grayscale image g by means of $g(x,y) = \bigvee\{t \in \mathbb{R} \mid (x,y) \in G(t)\}$. The mapping $g = \psi(f)$ thus obtained is called a *flat image operator*, generated by Ψ.

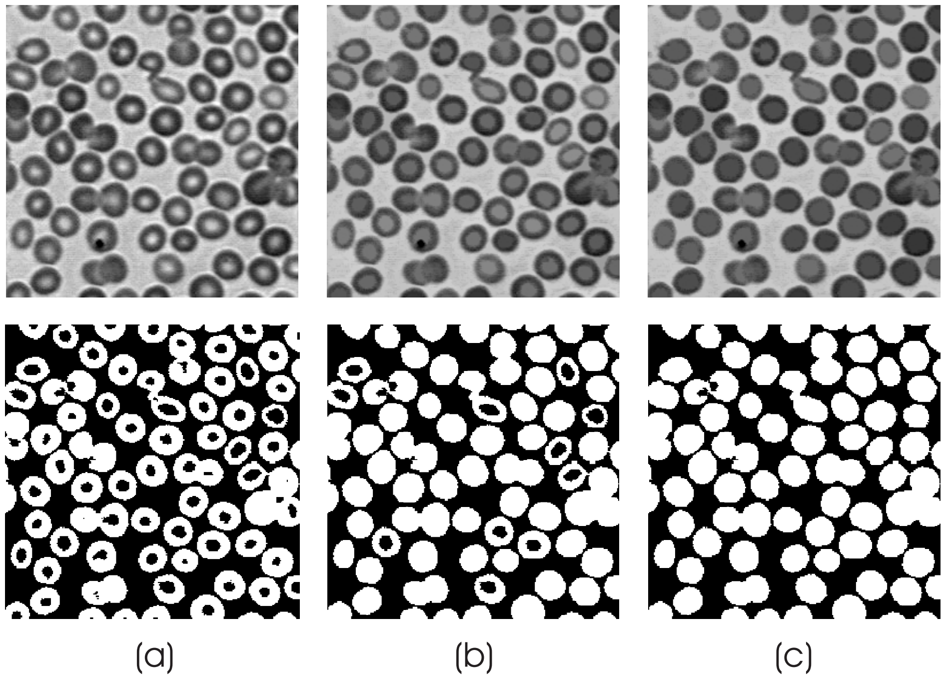

Figure 3.19: *Grayscale area opening: (a) original grayscale image of a blood smear (first row) and the result obtained after binarization by means of thresholding (second row); (b) the result of area opening (first row), applied on the grayscale image in (a), obtained by means of (3.25) with* $\alpha = 100$*, and the result obtained after binarization by means of thresholding (second row); (b) the result of area opening (first row), applied on the grayscale image in (a), obtained by means of (3.25) with* $\alpha = 200$*, and the result obtained after binarization by means of thresholding (second row). – Data courtesy of SDC Information Systems. Used with permission.*

Clearly,

$$\psi(f)(x,y) = \bigvee\{t \in \mathbb{R} \mid (x,y) \in \Psi(F(t))\}.$$

Flat image operators are increasing. This follows directly from the way these operators are constructed. Moreover, they enjoy properties directly induced from the set operator applied on each cross section. For example, if Ψ is an erosion, then ψ is an erosion as well. The same is true when Ψ is a dilation, opening, or closing; then, ψ is a dilation, opening, or closing, respectively. Moreover, if $\Psi(F) = F \ominus B$, then $\psi(f) = f \ominus B$. Thus, a flat (grayscale) erosion with structuring element B can be viewed as the process of applying a binary erosion on the cross sections of f with structuring element B and stacking-up the results. This gives a geometric interpretation of what erosion does to a grayscale image: the flat erosion of a grayscale image f by a structuring element B removes all grains in the cross sections

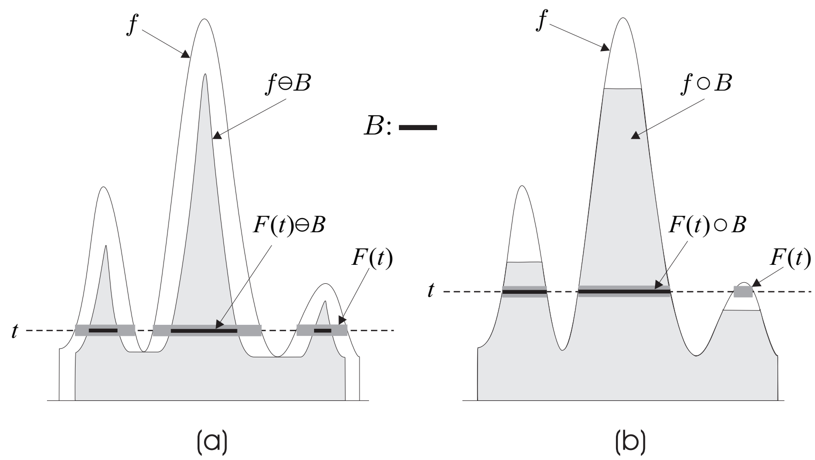

Figure 3.20: *An example of flat grayscale erosion, in (a), and of flat opening, in (b).*

of f that do not accommodate B whereas it "shrinks" all other grains by eroding them with B. This is illustrated in Fig. 3.20(a). A similar (dual) remark applies for the case of flat (grayscale) dilation.

If $\Psi(F) = F \bigcirc B$, then $\psi(f) = f \bigcirc B$. Thus, a flat (grayscale) opening with structuring element B can be viewed as the process of applying a binary opening on the cross sections of f with structuring element B and stacking-up the results. This again, gives a geometric interpretation of what opening does to a grayscale image: the flat opening of a grayscale image f by a structuring element B removes all grains in the cross sections of f that do not accommodate B whereas it smoothes all other grains by opening them with B. This is illustrated in Fig. 3.20(b). Therefore, the flat opening of an image f with a structuring element B can be viewed as an operator that removes the peaks and ridges from the *topographic surface* of f. A *peak*, or *regional maximum*, M of a grayscale image f is a connected component of pixels in f with a given graylevel value v, such that every pixel in a (properly defined) neighborhood of M has a value strictly smaller than v. A *ridge*, or *crest line*, of a grayscale image f is a curve on the topographic surface of f, such that, as we walk along this line, the points to the right and left of us are lower than the ones we are on. A similar (dual) remark applies for the case of flat (grayscale) closing, which removes the hollows and ravines from the topographic surface of f. A *hollow*, or *regional minimum*, M of a grayscale image f is a connected component of pixels in f with a given graylevel value v, such that every pixel in a (properly defined) neighborhood of M has a value strictly larger than v. A *ravine*, or *valley*, of a grayscale image f is a curve on the topographic surface of f, such that, as we walk along this line, the points to the right and left of us are higher than the ones we are on.

3.4.8 Morphological gradients

The grayscale operator

$$\psi_{\text{grad}}(f) = \frac{1}{2}\left[f \oplus B - f \ominus B\right],$$

where B is a structuring element that contains the origin, is known as the *grayscale morphological gradient.* If B is a disk structuring element with unit radius, then

$$\begin{aligned} ||\nabla f||_2 &= \sqrt{\left(\frac{\partial f(x,y)}{\partial x}\right)^2 + \left(\frac{\partial f(x,y)}{\partial y}\right)^2} \\ &= \lim_{r \to 0^+} \frac{1}{2r}\left[f \oplus rB - f \ominus rB\right], \end{aligned}$$

provided that f is continuously differentiable. In this case, the morphological gradient with a disk structuring element of radius r converges to the magnitude of the gradient ∇f of f, as r decreases to zero.

Similar gradient operators are the *external* and *internal* gradients, given by

$$\psi^+_{\text{grad}}(f) = \frac{1}{2}\left[f \oplus B - f\right],$$

and

$$\psi^-_{\text{grad}}(f) = \frac{1}{2}\left[f - f \ominus B\right],$$

respectively. Notice that

$$\psi_{\text{grad}}(f) = \psi^+_{\text{grad}}(f) + \psi^-_{\text{grad}}(f).$$

Figure 3.21 depicts an example of applying the grayscale morphological gradient, and its variants, on a *magnetic resonance* (MR) image of the human brain. In this case, the *square* structuring element $B_{\text{sq}} = \{(-1,-1), (-1,0), (-1,1), (0,-1), (0,0), (0,1), (1,-1), (1,0), (1,1)\}$, centered at the origin $(0,0)$, has been used. Notice that, in this example, the internal gradient provides the best separation between anatomical structures.

3.4.9 Opening and closing top-hat

Since the opening $f \circ B$ of an image f with a flat structuring element B removes peaks and ridges from the topographic surface of f, the operator

$$\psi_{\text{opnth}}(f) = f - f \circ B$$

produces such peaks and ridges. This is known as the *opening top-hat operator.* Dually, the operator $\psi_{\text{cloth}}(f) = f \bullet B - f$ produces the hollows and ravines of the topographic surface of f. This is known as the *closing*

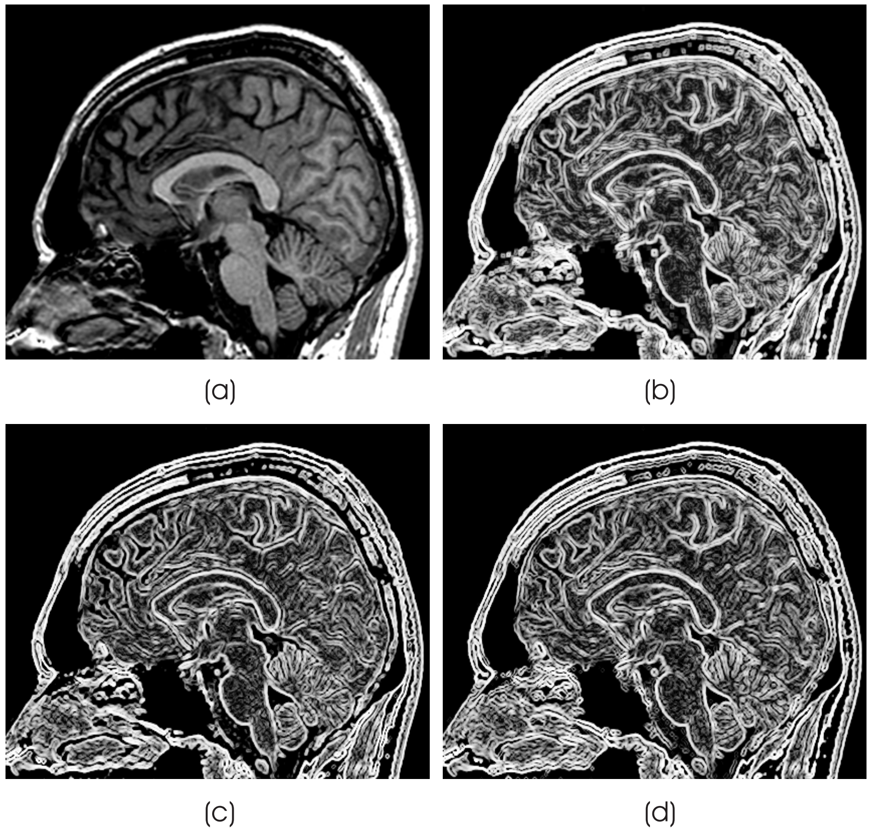

Figure 3.21: *Grayscale morphological gradient: (a) an MR image of the human brain; (b) histogram equalized grayscale morphological gradient with the square structuring element* B_{sq}*; (c) histogram equalized grayscale internal morphological gradient; (d) histogram equalized grayscale external morphological gradient. – Data courtesy of the University of Washington Digital Anatomist Program. Used with permission.*

top-hat operator. Figure 3.22 illustrates the use of this operator to extract and visualize the sulci from a lateral view of the right brain hemisphere. The procedure is shown for a 2D grayscale image. However, it can be used for a 3D representation of the brain as well. Correct extraction and visualization of sulci is important for identifying landmarks to achieve functional segmentation of the brain and to guide the surgeon during an operation.

3.4.10 Conditional dilation

If a grayscale image is dilated with a structuring element that contains the origin, its subgraph grows. If this type of dilation is successively repeated, the subgraph of the original image grows without bound. One way to restrict this growth is to restrict the dilation $f \oplus B$ of an image f by a structuring

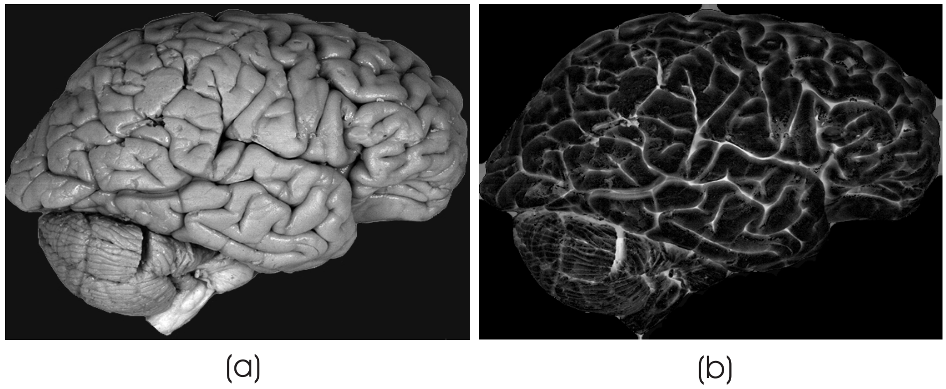

Figure 3.22: *Morphological closing top-hat: (a) lateral view of the right brain hemisphere; (b) closing top-hat by a disk structuring element with a diameter of 22 pixels. – Data courtesy of the University of Washington Digital Anatomist Program. Used with permission.*

element B within a mask image m. This defines the so-called *grayscale conditional dilation*, given by

$$\psi_\delta(f \mid m) = (f \oplus B) \wedge m.$$

It will become clear in the following (see Section 3.6), that the grayscale conditional dilation plays a key role in defining a new morphological operator, known as grayscale opening by reconstruction, which turns-out to be very useful in image segmentation problems.

3.4.11 Morphological filters

A grayscale operator ψ is said to be a *morphological filter*, if ψ is increasing (i.e., $f_1 \leq f_2 \Rightarrow \psi(f_1) \leq \psi(f_2)$) and idempotent (i.e., $\psi\psi(f) = \psi(f)$). Grayscale morphological filters are most frequently used to smooth the topographic surface of an image. According to this definition, grayscale openings and closings are morphological filters, since they are increasing and idempotent. However, grayscale erosions and dilations are not morphological filters, since they are not idempotent.

As in the binary case, we can build grayscale morphological filters from other grayscale morphological filters by composition (e.g., see [6,61]). If ψ_1 and ψ_2 are two grayscale morphological filters such that $\psi_1 \leq \psi_2$ or $\psi_2 \leq \psi_1$, then

$$\psi_2\psi_1, \quad \psi_1\psi_2, \quad \psi_1\psi_2\psi_1, \quad \text{and} \quad \psi_2\psi_1\psi_2$$

are grayscale morphological filters as well. Based on these compositions, the operators (recall that $f \circ B \leq f \bullet B$, for every structuring element B)

$$\pi_k(f) = (f \circ kB) \bullet kB \quad \text{and} \quad \rho_k(f) = (f \bullet kB) \circ kB, \tag{3.26}$$

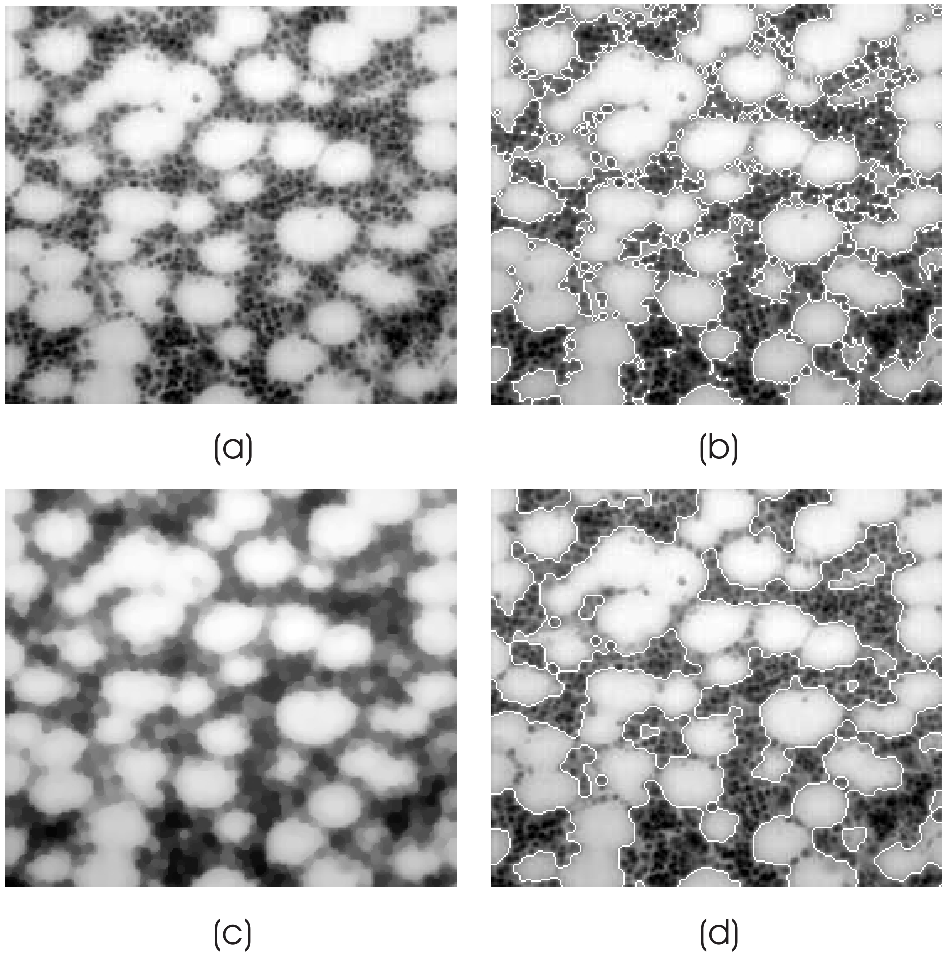

Figure 3.23: *Morphological filtering: (a) a bone marrow image f to be segmented into two regions of interest (from [90]); (b) detected edges, obtained by means of thresholding the image in (a) and applying the internal morphological gradient operator (3.17) on the binary result; (c) the result of applying the AF π_2 on f; (d) detected edges, obtained by means of thresholding the image in (c) and applying the internal morphological gradient operator (3.17) on the binary result.*

where kB is given by (3.19), are grayscale morphological filters. These filters are known as *grayscale alternating filters* (AF), since they alternate between opening and closing. The operators

$$\sigma_k(f) = ((f \circ kB) \bullet kB) \circ kB \quad \text{and} \quad \tau_k(f) = ((f \bullet kB) \circ kB) \bullet kB$$

are grayscale morphological filters as well. Finally, we can compose grayscale alternating filters to form another class of morphological filters known as *grayscale alternating sequential filters* (ASF), given by

$$\mu_k(f) = \pi_k \pi_{k-1} \cdots \pi_1(f) \quad \text{and} \quad \nu_k(f) = \rho_k \rho_{k-1} \cdots \rho_1(f).$$

Morphological filters are used to reduce grayscale variation in images. This may be desirable in order to reduce noise or simplify grayscale variation in an image for subsequent processing. An example is illustrated in Fig. 3.23. The bone marrow image f, depicted in Fig. 3.23(a), is to be segmented into two regions of interest. Towards this goal, f is first thresholded and the internal morphological gradient operator (3.17) is then applied on the binary result. Figure 3.23(b) depicts the detected edges, overlaid on the original image f. Clearly, the segmentation result is rather noisy due to high grayscale variation in f. However, application of the AF π_2 on f, given by (3.26), with B being a disk structuring element with a diameter of 3 pixels, produces the simplified version $\pi_2(f)$ of f depicted in Fig. 3.23(c). The internal morphological gradient operator (3.17), applied on the binary image obtained by thresholding $\pi_2(f)$, produces the result depicted in Fig. 3.23(d). Clearly, the result is smoother than the one in Fig. 3.23(b), and provides a reasonable segmentation of the original image f.

For more information on grayscale morphological filters, the reader is referred to [6, 54, 61–63].

3.5 Grayscale discrete size transform

In this section, we discuss the grayscale analogues of the discrete size transform and the associated pattern spectrum. The reader is referred to [66] for more details on these subjects. Although the skeleton transform can be defined for grayscale images as well, the resulting image representation is not very useful in practice. Therefore, we will not be discussing this representation here.

Given a grayscale image f, its *discrete size transform* (DST) is defined by

$$f \mapsto (..., d_{-k}(f;B), ..., d_{-1}(f;B), d_0(f;B), d_1(f;B), ..., d_k(f;B), ...),$$

where

$$d_k(f;B) = \begin{cases} f \bigcirc kB - f \bigcirc (k+1)B, & \text{for } k = 0, 1, \ldots \\ f \bullet |k|\breve{B} - f \bullet (|k|-1)\breve{B}, & \text{for } k = -1, -2, \ldots \end{cases},$$

with kB defined in (3.19). We limit our presentation here to flat openings and closings, although extension to more general structural openings and closings is possible [66]. Notice that

$$f \bigcirc (k+1)B \leq f \bigcirc kB \quad \text{and} \quad f \bullet k\breve{B} \leq f \bullet (k+1)\breve{B},$$

for $k = 0, 1, \ldots$. Therefore, the components $d_k(f; B)$ of the grayscale DST are always nonnegative, for every k. Moreover,

$$f = \sum_{k \geq 0} d_k(f; B) = \left[\sum_{k \leq -1} d_k(f; B) \right]^*,$$

where f^* is defined in (3.23). Therefore, the grayscale DST is an *invertible* image decomposition scheme.

The grayscale DST is a *multiresolution* image decomposition scheme, which decomposes an image f into residual images $f \circ kB - f \circ (k+1)B$ and $f \bullet |k|\breve{B} - f \bullet (|k|-1)\breve{B}$, obtained by successive approximations of f by means of structural openings and closings. Notice that, $d_0(f; B) = f - f \circ B$ is the opening top-hat transform of f, whereas $d_{-1}(f; B) = f \bullet \breve{B} - f$ is the closing top-hat transform. In general, $d_k(f; B)$, for $k \geq 0$, contains a layer scrapped from the subgraph of f by means of the difference $f \circ kB - f \circ (k+1)B$, whereas $d_k(f; B)$, for $k \leq -1$, contains a layer scrapped from the subgraph of f^* by means of the difference $f \bullet |k|\breve{B} - f \bullet (|k|-1)\breve{B}$. Since both opening and closing are smoothing (lowpass) filters, the DST can be thought of as the output of a filterbank comprising a collection of bandpass filters. However, the term *band* is not associated here to the frequency content of f, as is customary in linear filterbank techniques (e.g., see [64]), but to the particular layer scrapped from the subgraph of f.

The pattern spectrum of a grayscale image f, in terms of a structuring element B, is given by

$$P_{f;B}(k) = ||d_k(f; B)||_1 = \begin{cases} ||f \circ kB - f \circ (k+1)B||_1, & \text{for } k \geq 0 \\ ||f \bullet |k|\breve{B} - f \bullet (|k|-1)\breve{B}||_1, & \text{for } k \leq -1 \end{cases},$$

where

$$||f||_1 = \sum_{x,y} |f(x, y)|.$$

Clearly, the pattern spectrum is the "magnitude" of the discrete size transform.

The pattern spectrum turns-out to be a powerful tool for summarizing shape and texture content in images. It has been effectively used for grayscale morphological filtering and restoration [74], as well as for the analysis, segmentation, and classification of texture [74, 75, 77, 78, 80, 81, 91, 92]. Efficient algorithms for computing the pattern spectrum can be found in [84, 93, 94].

3.6 Morphological image reconstruction

In this section, we discuss a powerful tool for object extraction from binary and grayscale images, known as morphological image reconstruction. This

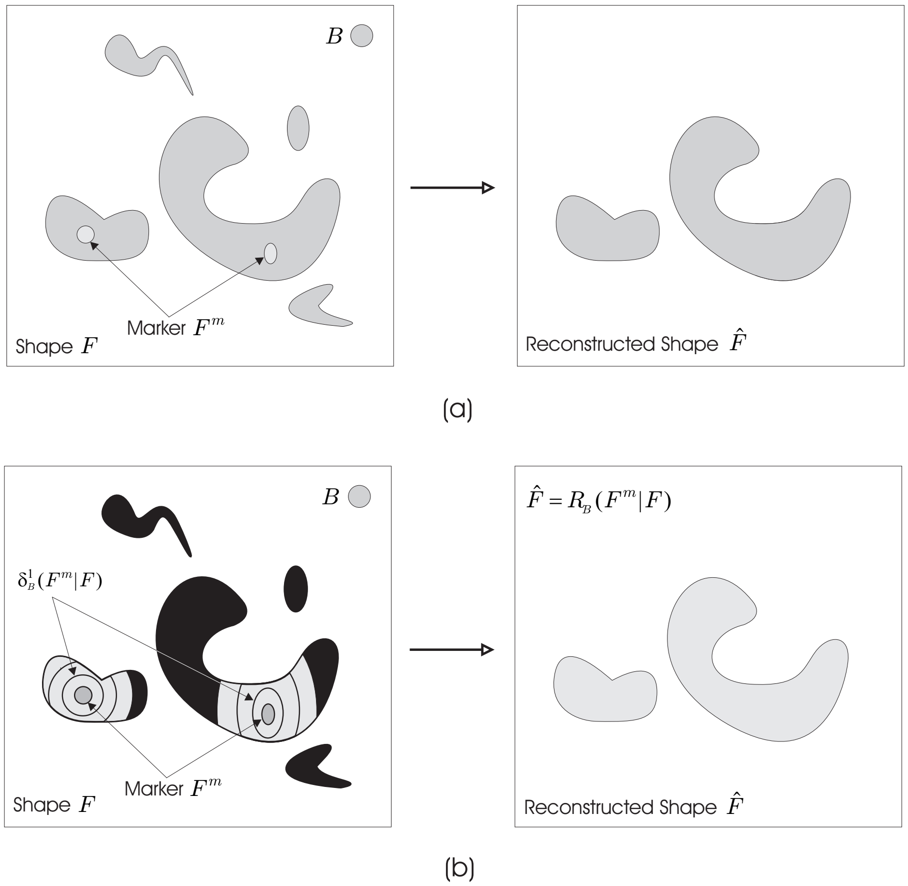

Figure 3.24: *(a) The problem of binary morphological image reconstruction. (b) Binary morphological image reconstruction implemented by means of conditional dilations.*

is an iterative tool that extracts regions of interest from an image marked by a set of markers. We start, by limiting our exposition to the binary case. We then extend our discussion to the grayscale case by means of threshold decomposition.

3.6.1 Reconstruction of binary images

Consider a shape F, like the one depicted in Fig. 3.24(a), comprising several (nonoverlapping) grains. Suppose that we are interested in an operator that automatically extracts all grains $\hat{F}$ of F that are marked by a *marker* F^m (i.e., a set $F^m \subseteq F$). In practice, F^m may mark important targets of interests (objects) that need to be extracted from image F.

Let $\{F_i \mid i = 1, 2, \ldots\}$ be the collection of all grains of F and let $\hat{F}$ denote the portion of F that contains all grains marked by F^m. Under certain conditions, $\hat{F}$ can be computed by means of elementary morphological operators. Indeed, let

$$\delta_B^1(F^m \mid F) = (F^m \oplus B) \cap F,$$

be the conditional dilation (of size 1) of F^m by a structuring element B (that contains the origin) restricted inside F. This conditional dilation "expands" the marker F^m by means of the structuring element B, while making sure that this "expansion" remains inside F (see Fig. 3.24(b)). Iterating this operator k times, yields the *conditional dilation* of size k, given by

$$\delta_B^k(F^m \mid F) = \overbrace{\delta_B^1 \delta_B^1 \cdots \delta_B^1}^{k \text{ times}}(F^m \mid F).$$

It can be shown that, if B is a structuring element that contains the origin, such that

$$(F_i \oplus B) \cap F_j = \emptyset, \quad \text{for every } i \neq j, \tag{3.27}$$

then binary morphological image reconstruction can be achieved by taking the union of all δ_B^k's; i.e.,

$$\hat{F} = R_B(F^m \mid F) = \bigcup_{k \geq 1} \delta_B^k(F^m \mid F). \tag{3.28}$$

The required condition (3.27) simply says that the grains $\{F_i \mid i = 1, 2, \ldots\}$ of F should be "far enough" from each other, in the sense that, for every i, "expanding" F_i by B does not hit any other grain of F. In the discrete case, however, B is typically chosen as the cross structuring element B_{cr}, or the square structuring element B_{sq}, and the condition (3.27) is automatically satisfied. The union in (3.28) always exists, since $F^m \subseteq \delta_B^1(F^m \mid F) \subseteq F$ and therefore the sequence $\{\delta_B^k\}_{k=1,2,\ldots}$ is increasing and bounded from above by F. The resulting operator R_B is called the *conditional reconstruction operator*. Notice that $\delta_B^k(F^m \mid F)$ can be sequentially implemented using

$$\delta_B^k(F^m \mid F) = \delta_B^1(\delta_B^{k-1}(F^m \mid F) \mid F), \quad \text{for } k = 1, 2, \ldots, \tag{3.29}$$

with $\delta_B^0(F^m \mid F) = F^m$. See Fig. 3.24(b) for an illustration.

In many applications, we are interested in a morphological filter that filters-out grains that are of a certain size and shape. For example, consider the problem of removing grains with size smaller than a predefined size n_0, in the sense that all grains that cannot accommodate a structuring element $A = n_0 B$ are completely eliminated, whereas all other grains remain intact. One may think that a simple opening $F \circ A$ of the image F by the structuring element A will do the job. This is only partially true. The opening $F \circ A$ will clearly eliminate all grains of F that cannot contain structuring element $n_0 B$

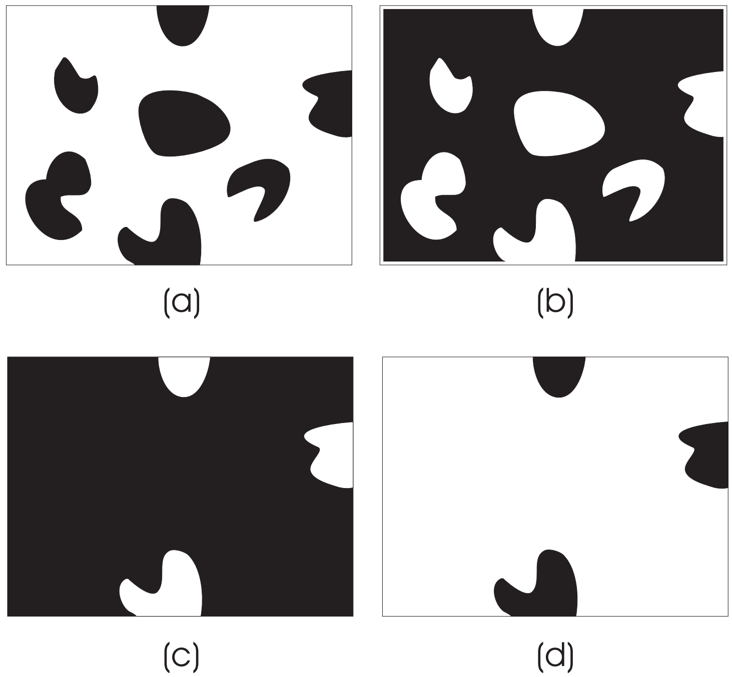

Figure 3.25: *Close-hole operator: (a) a binary image F; (b) the set complement F^c of F and the image window boundary marker F_∂; (c) the result of conditional reconstruction $R_B(F_\partial \mid F^c)$ – notice that only grains that touch the image window boundary are reconstructed; (d) the set complement of the image in (c) – all holes in F that do not touch the image window boundary are filled-in.*

but it will also smooth-out the other grains. However, recall that $F \circ A \subseteq F$. Therefore, the structural opening $F \circ A$ can be used as a marker in a binary morphological reconstruction operator that will reconstruct all those smoothed-out grains of F that remain after the structural opening is applied. It can be shown that the resulting operator

$$\Psi_{\text{opnrec}}(F) = R_B(F \circ A \mid F),$$

is an opening (i.e., an operator that is increasing, anti-extensive, and idempotent). This operator is called *opening by reconstruction.* The dual operator

$$\Psi_{\text{clorec}}(F) = [R_B(F^c \circ A \mid F^c)]^c$$

is a closing (i.e., an operator that is increasing, extensive, and idempotent) and is called *closing by reconstruction.*

The binary conditional reconstruction operator can be used to define another useful morphological operator, known as the *binary close-hole* operator. This operator is given by

$$\Psi_{\text{clohole}}(F) = [R_B(F_\partial \mid F^c)]^c, \tag{3.30}$$

where the binary marker F_∂ is the boundary of the image window. As illustrated in Fig. 3.25, the close-hole operator fills-in all holes in a binary image that do not touch the image window boundary.

3.6.2 Reconstruction of grayscale images

Morphological image reconstruction can be extended to the grayscale case via threshold decomposition. Consider a signal f, like the one depicted in Fig. 3.26. The topographic surface of this signal comprises of several peaks. Suppose that we are interested in designing an operator that automatically removes a pre-selected number of peaks, while leaving the rest of the signal intact. This operation can be very useful in practice: in an image profile, peaks are usually attributed to objects, and peak removal is equivalent to object removal.

Peak removal can be automatically and effectively done by means of the grayscale morphological image reconstruction operator, to be discussed here. Let us assume that, given an image f, we can find another image f^m, known as the *marker image* (or simply as the *marker*), which identifies the portion of the image profile that needs to be preserved (see Fig. 3.26). It is required that $f^m \leq f$. Let us denote by $\mathcal{F} = \{F(t) \mid t \in \mathbb{R}, F(t) \neq \emptyset\}$ and by $\mathcal{F}^m = \{F^m(t) \mid t \in \mathbb{R}, F^m(t) \neq \emptyset\}$ the threshold decompositions of f and f^m, respectively. Notice that, since $f^m \leq f$, we have that $F^m(t) \subseteq F(t)$, for every t. Therefore, $F^m(t)$ can be considered to be a binary marker for $F(t)$. Each binary marker $F^m(t)$ marks a number of grains of the cross section $F(t)$ of image f at level t. If we apply the binary morphological image reconstruction operator $R_B(F^m(t) \mid F(t))$ on $F^m(t)$, given $F(t)$, then all grains of $F(t)$ marked by $F^m(t)$ will be perfectly reconstructed. If we repeat this process for every t, and stack-up the results, we obtain a grayscale operator $r_B(f^m \mid f)$ which is known as *grayscale conditional reconstruction operator*. Since the marker image f^m marks the portion of the image profile that we want preserved, this portion will be perfectly reconstructed from the marker. Notice that

$$\hat{f}(x,y) = r_B(f^m \mid f)(x,y) = \bigvee\{t \in \mathbb{R} \mid (x,y) \in R_B(F^m(t) \mid F(t))\}.$$

Because $R_B(F^m \mid F)$ is an increasing operator, given F, $r_B(f^m \mid f)$ is a flat image operator generated by $R_B(\bullet \mid F)$. Under certain conditions, $r_B(f^m \mid f)$ can be computed by means of elementary grayscale morphological operators. Indeed, let

$$\delta_B^1(f^m \mid f) = (f^m \oplus B) \wedge f$$

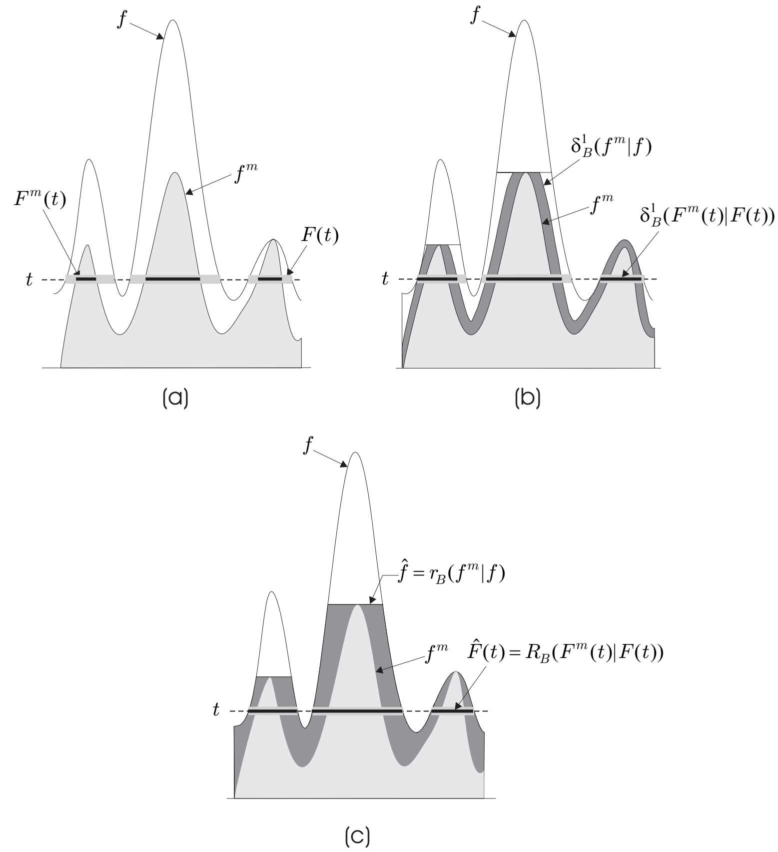

Figure 3.26: *Grayscale morphological image reconstruction: (a) a signal f and its marker f^m; (b) the result of the conditional dilation $\delta_B^1(f^m \mid f)$ of the marker f^m within f; (c) the reconstructed signal $\hat{f} = r_B(f^m \mid f)$.*

be the conditional grayscale dilation (of size 1) of f^m by a structuring element B (containing the origin) that is restricted by f. This conditional dilation "expands" the subgraph of marker f^m by means of the structuring element B making sure that this "expansion" is below f. Iterating this operator k times, yields the conditional grayscale dilation of size k, given by

$$\delta_B^k(f^m \mid f) = \overbrace{\delta_B^1 \delta_B^1 \cdots \delta_B^1}^{k \text{ times}}(f^m \mid f).$$

It can be shown that, if B is a structuring element that contains the origin, with

$$(F_i(t) \oplus B) \cap F_j(t) = \emptyset, \text{ for every } i \neq j, \text{and every } t,$$

where $F_i(t)$ is the i^{th} grain of the cross section $F(t)$ of f, then (grayscale) morphological image reconstruction can be achieved by taking the supremum of all δ_B^k's; i.e.,

$$\hat{f} = r_B(f^m \mid f) = \bigvee_{k \geq 1} \delta_B^k(f^m \mid f).$$

Notice that

$$\delta_B^k(f^m \mid f) = \delta_B^1(\delta_B^{k-1}(f^m \mid f) \mid f), \text{ for } k = 1, 2, \ldots, \tag{3.31}$$

with $\delta_B^0(f^m \mid f) = f^m$, which provides a sequential implementation of the reconstruction process.

Recall now that $f \circ A \leq f$. Therefore, $f \circ A$ can be used as a marker in a morphological reconstruction operator. The resulting operator

$$\psi_{\text{opnrec}}(f) = r_B(f \circ A \mid f) \tag{3.32}$$

is an opening (i.e., an operator that is increasing, anti-extensive, and idempotent) and is called *opening by reconstruction*. The dual operator

$$\psi_{\text{clorec}}(f) = [r_B(f^* \circ A \mid f^*)]^*, \tag{3.33}$$

where f^* is defined in (3.23), is a closing (i.e., an operator that is increasing, extensive, and idempotent) and is called *closing by reconstruction*. Notice that the opening $f \circ A$ will remove peaks and ridges from the topographic surface of f and, therefore, these features will not be marked by $f \circ A$. In this case, the opening by reconstruction operator $\psi_{\text{opnrec}}(f)$ will remove peaks and ridges from the topographic surface of f while preserving the topography of the remaining surface. A dual statement applies for the case of the closing by reconstruction operator.

The grayscale conditional reconstruction operator can be used to define another useful morphological operator, known as the *grayscale close-hole* operator. This operator is given by

$$\psi_{\text{clohole}}(f) = [r_B(f_\partial \mid f^*)]^*, \tag{3.34}$$

where the grayscale marker f_∂ takes value ∞ at pixels on the boundary of the image window, and $-\infty$, otherwise. Clearly, this operator fills-in all holes in the cross sections of image f that do not touch the image window boundary.

Morphological image reconstruction is a time consuming process. Sequential implementation, by means of (3.29) or (3.31), is inefficient. However, a number of alternative algorithms have been proposed in the literature that result in faster implementation. For more information on this subject, the reader is referred to [95].

3.6.3 Examples

Morphological image reconstruction is a powerful tool for extracting objects of interest from a given image. In the following, we illustrate this by means of two examples: detection of the lateral ventricle in an MR image of the brain, and extraction of filarial worms in a microscopic image of blood stream. Additional examples may be found in [95].

Feature detection in MR imaging.

This example illustrates the use of grayscale morphological image reconstruction for detecting the lateral ventricle in an MR image of the brain, depicted in Fig. 3.27(a). A grayscale structural opening, by a disk structuring element with a diameter of 31 pixels, is applied on this image, in order to remove the feature to be detected (i.e., the lateral ventricle). The result is depicted in Fig. 3.27(b). The grayscale morphological image reconstruction of that part of the original image marked by the image in (b) is depicted in Fig. 3.27(c). By subtracting this result from the original image in (a), we obtain the image depicted in Fig. 3.27(d). Notice the prominent presence of the lateral ventricle in (d), as well as the amount of image simplification obtained by means of the previous steps. Thresholding the image in (d) produces the binary image depicted in Fig. 3.27(e). Clearly, thresholding produces a binary image comprising of many grains, the most prominent one (in terms of area) being the grain associated with the lateral ventricle. An area opening, applied on the image in (e), eliminates all grains with area smaller than 150 pixels, while preserving the desirable feature (i.e., the lateral ventricle). The boundary of the result of this area opening, overlaid on the original image, is depicted in Fig. 3.27(f). The detected lateral ventricle boundary is shown in black.

We should point-out here that the image depicted in Fig. 3.27(c) is obtained by applying the opening by reconstruction operator (3.32) on the image depicted in (a). Moreover, the image depicted in Fig. 3.27(d) is obtained by applying the operator

$$\psi_{\text{opnrecth}}(f) = f - r_B(f \bigcirc A \mid f)$$

on the image in (a). This is known as the *opening-by-reconstruction top-hat operator.*

Extraction of filarial worms.

In this example, the aim is to extract filarial worms from a microscopic image of blood stream by progressively eliminating all other objects present in the image. These tiny worms are spread by mosquitos and circulate in the bloodstream. An algorithm can be constructed, based on morphological image reconstruction, that is very effective in accomplishing this task.

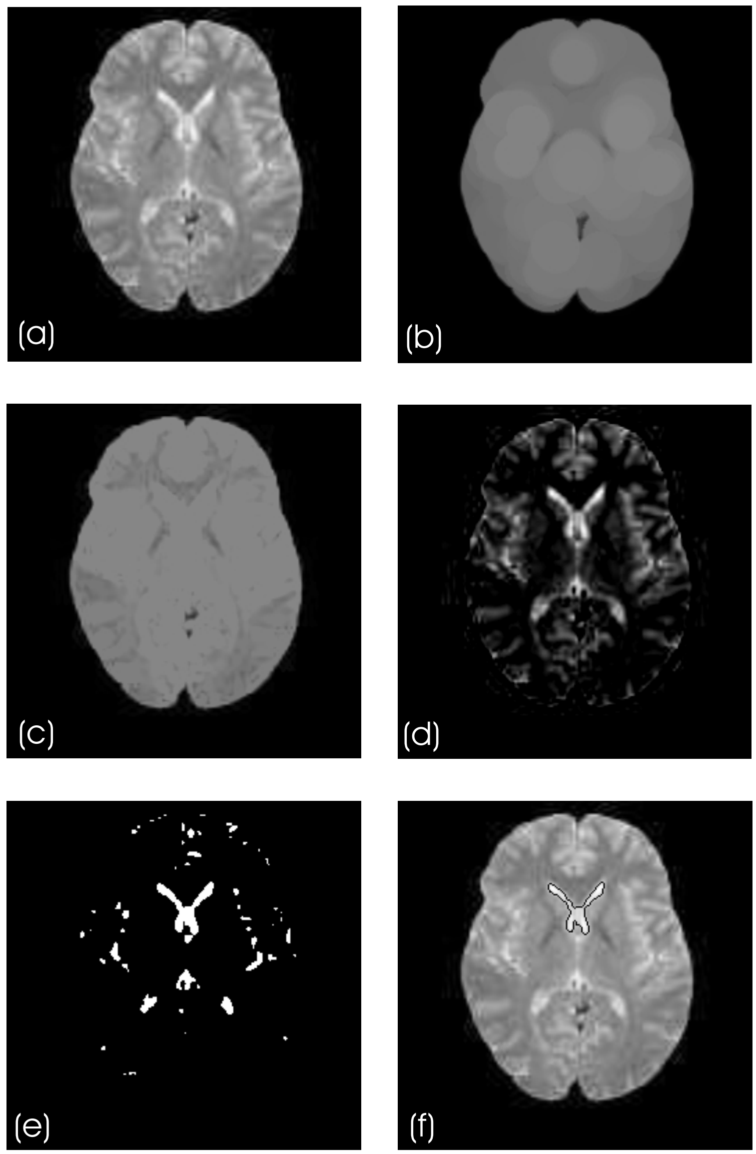

Figure 3.27: *Detection of the lateral ventricle in an MR image of the brain: (a) original image (from [96]); (b) grayscale structural opening of the image in (a) by a disk structuring element with a diameter of* 31 *pixels; (c) the result of grayscale morphological image reconstruction of that part of the image in (a) marked by the image in (b); (d) the differences between the images in (a) and (c); (e) the result of thresholding the image in (d); (f) the boundary of the result of applying a binary area opening on the image in (e), overlaid on the original data in (a).*

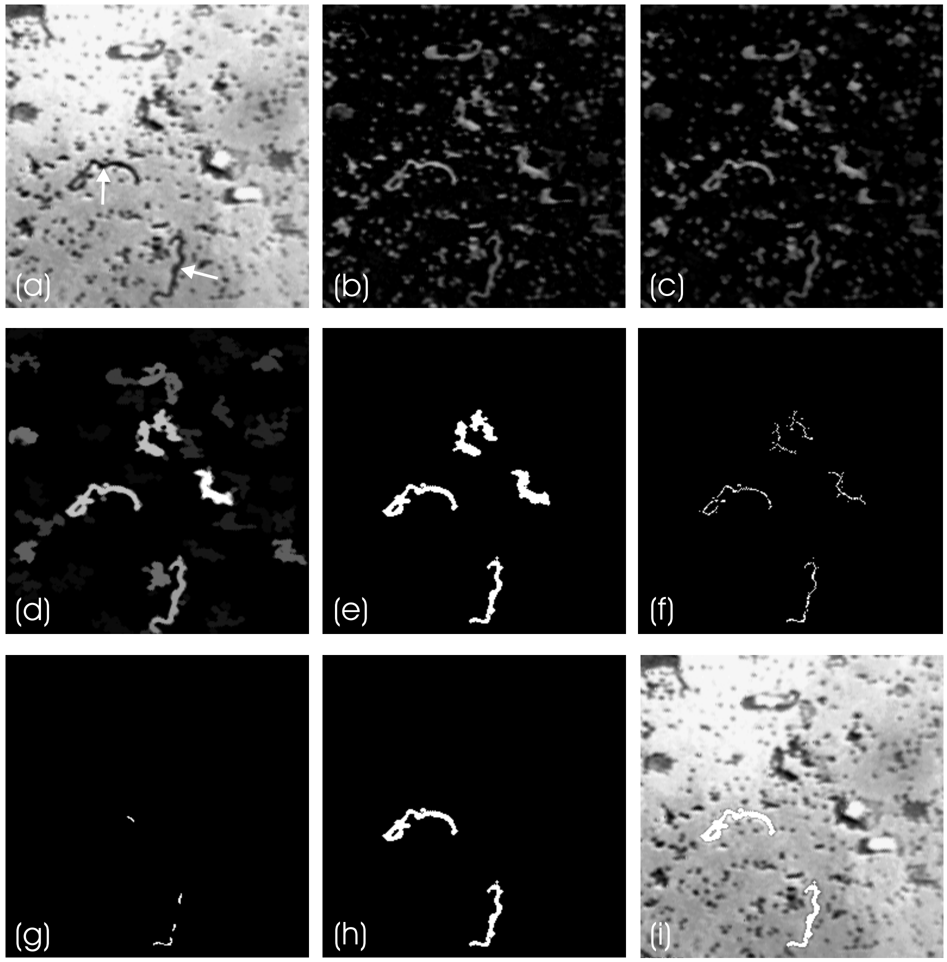

Figure 3.28: *Extraction of filarial worms: (a) a microscopic image of filarial worms in the blood stream, indicated by the two white arrows; (b) the difference between the original image in (a) and a grayscale closing by reconstruction operator applied on (a); (c) the grayscale structural opening of the image in (b) by the cross structuring element* B_{cr}*; (d) the grayscale area opening of the image in (c); (e) the result of thresholding the image in (d); (f) the morphological skeleton of the image in (e); (g) the result of a binary area opening applied on the image in (f); (h) binary morphological reconstruction of the filarial worms from the image in (e), using the image in (g) as a marker; (i) the reconstruction result in (h), overlaid on the original image in (a). – Images courtesy of SDC Information Systems. Used with permission.*

The steps of this algorithm are illustrated in Fig. 3.28. Figure 3.28(a) depicts a microscopic image of filarial worms in the blood stream, indicated by the two white arrows. Although these objects could be extracted by simple thresholding, this turns-out to be very difficult, due to artifacts present in the image. We can use the observation that filarial worms show up as dark, thin, and long objects, in order to design a series of steps that eventually filter-out all objects from the image, except those ones that fit this description. We will be using a combination of morphological reconstruction operators and the morphological skeleton transform in order to accomplish this task. Towards this goal, we subtract the image depicted in Fig. 3.28(a) from the image obtained by applying the closing by reconstruction operator (3.33), with A being an 11-pixel-wide square structuring element, on the image depicted in (a). The result is depicted in Fig. 3.28(b). This step regularizes the image background. We then apply a grayscale structural opening, by the cross structuring element B_{cr}, in order to remove narrow objects from the image in (b). The result is depicted in Fig. 3.28(c). The grayscale area opening operator (3.25) is then applied on the image in (c) in order to remove small objects with area smaller than 200 pixels. This produces the image depicted in Fig. 3.28(d). Now, thresholding the image in (d) produces the result depicted in Fig. 3.28(e), which contains five grains. Notice that, two of the five grains are the filarial worms we are interested in. The length of the other three grains is clearly smaller than the length of the filarial worms. We can use this information to filter-out the three unwanted grains. First, we calculate the morphological skeleton of the image in (e). The result is depicted in Fig. 3.28(f). Then, a binary area opening removes skeleton branches with area smaller than 10 pixels, producing the image depicted in Fig. 3.28(g). The resulting image is used as a marker, in a binary morphological reconstruction step, that reconstructs that part of the image in (e) marked by this marker. The result of this step is depicted in Fig. 3.28(h). Clearly, the reconstructed grains are the two filarial worms. Finally, Fig. 3.28(i) depicts the detected filarial worms, overlaid on the original image in (a).

We should point-out here that the image depicted in Fig. 3.28(b) is obtained by applying the operator

$$\psi_{\mathrm{clorecth}}(f) = [r_B(f^* \circ A \mid f^*)]^* - f$$

on the image depicted in (a). This is known as the *closing-by-reconstruction top-hat operator*.

3.7 Morphological image segmentation

An important application of mathematical morphology is in image segmentation, which deals with the problem of decomposing an image into different areas of interest (see also Chapters **??** and **??** in this volume). In this section, we discuss the problem of segmenting binary and grayscale images by means of mathematical morphology. The main tools associated with this problem is the skeleton by influence zones and the watershed transform.

3.7.1 The distance transform

The distance transform is a basic tool for the construction of morphological segmentation operators. It will soon become apparent that the distance transform is intrinsically related to many morphological set operators, like translation invariant erosions, dilations, and skeletons, to mention a few.

Let us consider images defined over the two-dimensional Euclidean space $\mathbb{R}^2$. A function $d(\bullet, \bullet)$ from $\mathbb{R}^2 \times \mathbb{R}^2$ into the set of nonnegative real numbers $\mathbb{R}^+$ is called a *distance function*, if the following three properties are satisfied:

1. $d(u, v) = 0$ if and only if $u = v,\ u, v \in \mathbb{R}^2$.
2. $d(u, v) = d(v, u)$, for every $u, v \in \mathbb{R}^2$.
3. $d(u, w) \leq d(u, v) + d(v, w)$, for every $u, v, w \in \mathbb{R}^2$.

One calls $d(u, v)$ the *distance* between points u and v. Examples of common distance functions between two points $u = (u_1, u_2)$ and $v = (v_1, v_2)$ in $\mathbb{R}^2$ are

$$d_1(u, v) = |u_1 - v_1| + |u_2 - v_2|, \qquad \textit{cityblock distance}$$

$$d_2(u, v) = \sqrt{(u_1 - v_1)^2 + (u_2 - v_2)^2}, \quad \textit{Euclidean distance}$$

$$d_\infty(u, v) = \max\{|u_1 - v_1|, |u_2 - v_2|\}, \quad \textit{chessboard distance.}$$

Given a distance function d, the *distance transform* $D_F(u)$ of a binary image $F \subseteq \mathbb{R}^2$ at a point $u \in \mathbb{R}^2$ is defined by

$$D_F(u) = \bigwedge_{v \in F} d(u, v).$$

By convention, we set $D_\emptyset(u) = \infty$, for every $u \in \mathbb{R}^2$. Notice that the distance transform is a grayscale function that depends on the particular choice of the distance function d. Its value is zero at all pixels $u \in F$ and increases as we move away from F.

Figure 3.29(a) depicts a microscopic image of red blood cells from a patient with hereditary spherocytosis. By binarizing the image in (a), we obtain the image F depicted in Fig. 3.29(b). Figure 3.29(c) depicts the distance transform $D_F(u)$, plotted as a 2D function, whereas Fig. 3.29(d) depicts the distance transform $D_{F^c}(u)$. In both cases, the Euclidean distance

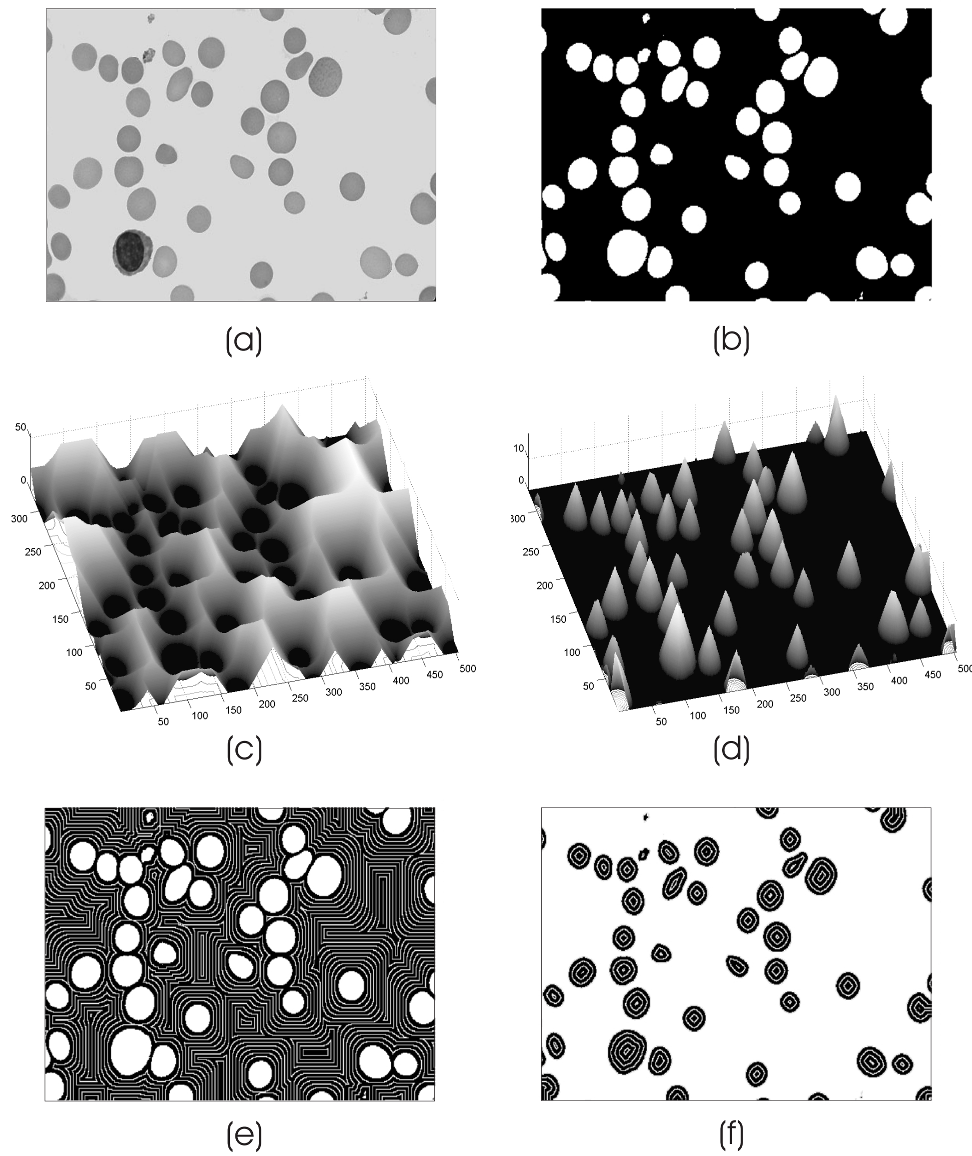

Figure 3.29: *The distance transform: (a) a grayscale microscopic image of red blood cells from a patient with hereditary spherocytosis; (b) binarized version* F *of the image in (a); (c) the distance transform* $D_F(u)$*; (d) the distance transform* $D_{F^c}(u)$*; (e) the level lines of the distance function* $D_F(u)$*; (f) the level lines of the distance function* $D_{F^c}(u)$*. – Data courtesy of K. C. Klatt, Department of Pathology, University of Utah. Used with permission.*

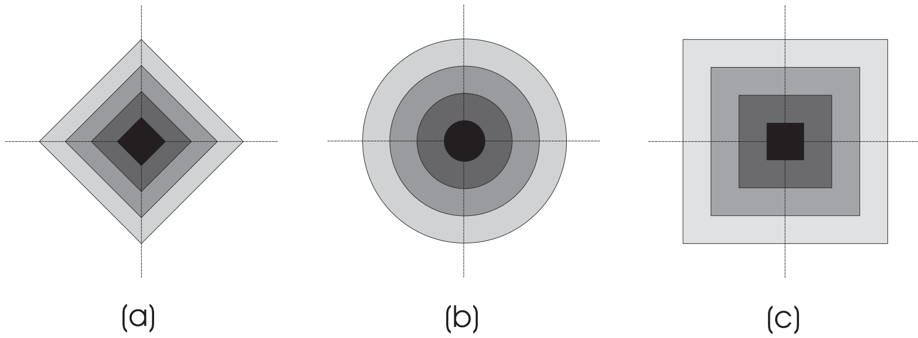

Figure 3.30: *"Disk" structuring elements with increasing radius, for three choices of the distance function: (a) cityblock distance; (b) Euclidean distance; (c) chessboard distance.*

is used. The nonzero values of $D_F(u)$ give the minimum distance of a pixel in F^c from the red blood cells, whereas the nonzero values of $D_{F^c}(u)$ give the minimum distance of a pixel within a red blood cell from its boundary. Notice that $D_F(u)$ is zero within the red blood cells, whereas $D_{F^c}(u)$ is zero outside the cells.

Given an image F, the collection of all points with equal distance to the foreground is obtained by extracting the level lines of the corresponding distance transform $D_F(u)$, whereas the collection of all points with equal distance to the background is obtained by extracting the level lines of the distance transform $D_{F^c}(u)$. Examples of such level lines are depicted in Figs. 3.29(e) and 3.29(f), respectively. Notice that the level lines in these figures coincide with the boundaries of successive translation invariant dilations and erosions of image F by a disk structuring element B of increasing radius. Indeed, if F is a closed and bounded subset of $\mathbb{R}^2$, then the dilated set $F \oplus rB$, where

$$B = \{u \in \mathbb{R}^2 \mid d(u, 0) \leq 1\} \tag{3.35}$$

is a "disk" structuring element with radius 1 centered at the origin, is given by

$$F \oplus rB = \{u \in \mathbb{R}^2 \mid D_F(u) \leq r\}. \tag{3.36}$$

This explains the fact that the boundaries of successive erosions with a "disk" structuring element coincide with the level lines in Fig. 3.29(e). Notice that (3.35), (3.36) depend on the particular choice for the distance function d, which leads to a particular choice for the "disk" structuring element B. Figure 3.30 depicts "disk" structuring elements rB, with increasing value of r, for three different choices of the distance function.

By using the duality between erosions and dilations, the level lines of the distance transform $D_{F^c}(u)$ can be associated with the boundaries of erosions with a "disk" structuring element. If F is a closed and bounded subset of $\mathbb{R}^2$, we have that

$$F \ominus rB = \{u \in \mathbb{R}^2 \mid D_{F^c}(u) > r\}. \tag{3.37}$$

Expressions (3.35)–(3.37) establish a clear relationship between the distance transform and translation invariant erosions and dilations with "disk" structuring elements. Different geometries for the structuring elements are achieved by changing the choice of the associated distance function. Nonetheless, the importance of the distance transform lies on the fact that it aggregates distance information from a continuum of erosions and dilations in a single grayscale function. As we will see in the following, this information can be used for segmentation and for marking areas of interest in a given image.

3.7.2 Skeleton by influence zones (SKIZ)

Let us consider a binary image F, made up of (nonoverlapping) grains F_i, $i = 1, 2, \ldots$. In this framework, the problem of image segmentation is to partition image F into disjoint segments such that, each partition contains only one grain, and the union of all partitions produces the entire image. This can easily be done by means of the so-called *skeleton by influence zones*, or simply SKIZ.

The *influence zone* $Z(F_i)$ of a grain F_i of F is defined as the collection of all points in $\mathbb{R}^2$ which are closer to F_i than to any other grain of F. Evidently,

$$Z(F_i) = \{u \in \mathbb{R}^2 \mid D_{F_i}(u) < D_{F_j}(u), \ \text{for every } i \neq j\}.$$

The set-complement of the union of the influence zones of all grains of F form the SKIZ of F; i.e.,

$$\mathit{SKIZ}(F) = \left(\bigcup_i Z(F_i) \right)^c.$$

Clearly, the SKIZ is the collection of all points in $\mathbb{R}^2$ that do not belong to any influence zone. Moreover, because the influence zone $Z(F_i)$ is an open subset of $\mathbb{R}^2$, the SKIZ is a closed subset of $\mathbb{R}^2$.

Interestingly, it can be shown that the SKIZ of a shape F follows the *ridges*, or *crest lines*, of the distance transform $D_F(u)$. Roughly speaking, a ridge, or crest line, of a grayscale image f is a curve on the topographic surface of f, such that, as we walk along this line, the points to the right and to the left are lower than the ones we are on. A more precise mathematical characterization, based on elementary concepts such as gradient, directional derivative and vector inner product can be found in [97]. A detailed analysis

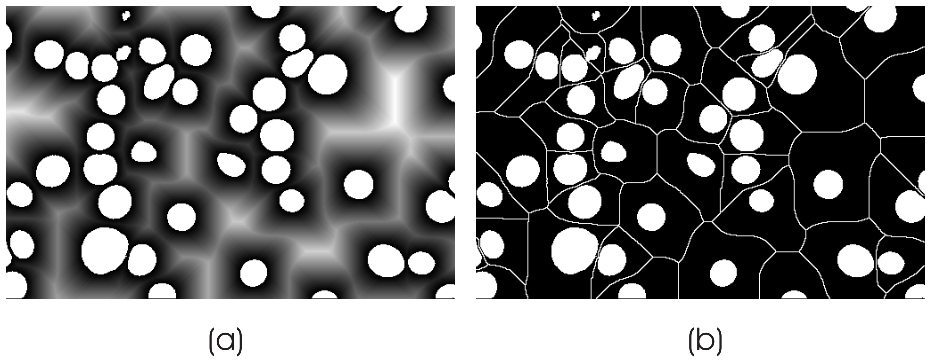

Figure 3.31: *Binary segmentation using the SKIZ: (a) the distance transform $D_F(u)$ of the image F depicted in Fig. 3.29(b), overlaid on F; (b) the SKIZ obtained by extracting the crest lines of $D_F(u)$, overlaid on F.*

of the *crest points* (i.e., the points forming a crest line) in a discrete setting, can be found in [98], with emphasis on the identification of the crest points of the distance function.

An example of binary image segmentation based on the SKIZ is depicted in Fig. 3.31. The distance transform $D_F(u)$ of the binary image F in Fig. 3.29(b) is depicted in Fig. 3.31(a), plotted as a grayscale function and overlaid on image F. The crest lines, extracted from $D_F(u)$, produce the SKIZ, which is depicted in Fig. 3.31(b), overlaid on F (refer to [99] for methods on how to extract crest lines and ravines in grayscale images). Clearly, the SKIZ forms a continuous disjoint net that effectively segments the image into disjoint partitions, each partition containing at most one red blood cell.

3.7.3 Watershed-based segmentation of nonoverlapping particles

An alternative way to obtain the SKIZ of a collection of (nonoverlapping) grains is to use the *binary watershed transform*. This procedure is illustrated in Fig. 3.32. Given a binary image F, like the one depicted in Fig. 3.29(b), the distance transform $D_F(u)$ is calculated. The result is depicted in Fig. 3.32(a). If droplets of water fall on the topographic surface of $D_F(u)$, they will follow the steepest slope towards a *hollow*, or *regional minimum*. Recall that a hollow, or regional minimum, M of a grayscale image f is a connected component of pixels in f with a given grayscale value v, such that, every pixel in the neighborhood of M has a value strictly larger than v. In this case, water will accumulate in the so-called *catchment basins* of $D_F(u)$; see Fig. 3.32(a). The catchment basin $C(M)$ of an image f, associated with a regional minimum M, is the collection of all points p of the topographic surface of f such that, a drop of water falling at p slides along the surface until it reaches M. A small hole is now punched at the bottom of each catchment basin of $D_F(u)$, and the subgraph of $D_F(u)$ is

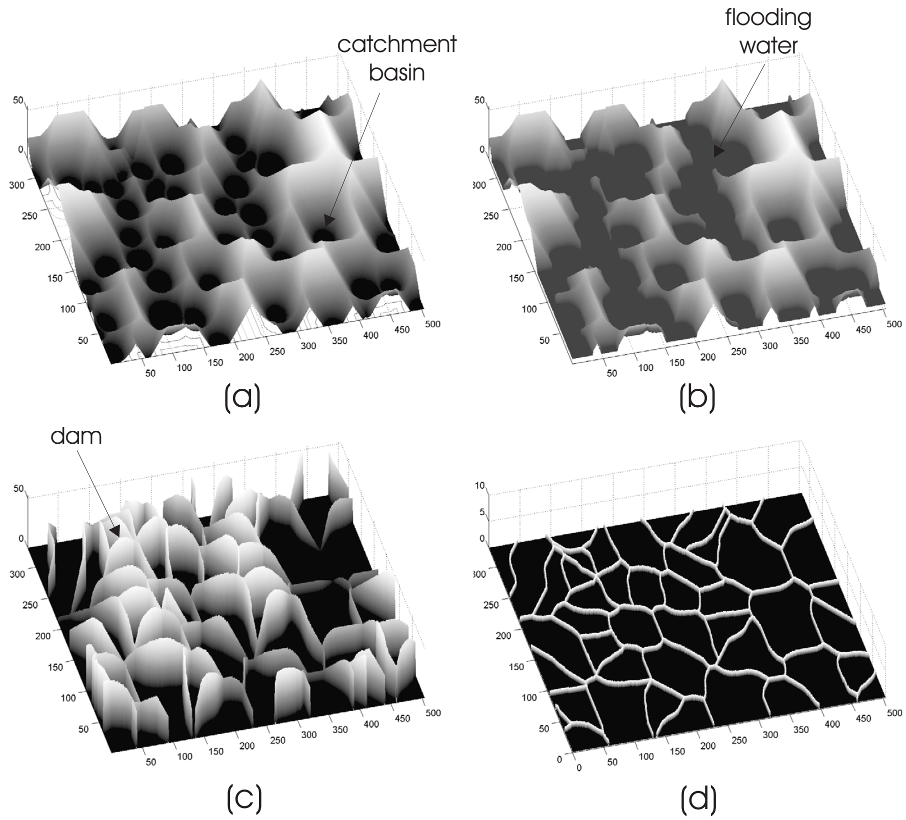

Figure 3.32: *The binary watershed transform: (a) the distance transform* $D_F(u)$ *of the image* F *depicted in Fig. 3.29(b); (b) the subgraph of* $D_F(u)$ *is immersed into water – water fills-in from holes punched through the bottom of catchment basins; (c) the dams constructed to avoid water from merging from two adjacent catchment basins; (d) the top of the dams in (c) defines the watershed lines, which are overlaid on* F.

slowly immersed into water. While the subgraph is flooded, by water passing through the holes, the water level raises uniformly over the subgraph; see Fig. 3.32(b). At some moment, water filling a catchment basin starts merging with water coming from an adjacent catchment basin. At this particular moment, a *dam* is erected to prevent this from happening. When no new dams need to be constructed, the procedure is stopped. The collection of all erected dams are depicted in Fig. 3.32(c). When the subgraph of $D_F(u)$ is totally immersed into water, the only visible structures at the water surface will be the top of the dams. These form the so-called *watershed lines*, which are depicted in Fig. 3.32(d). It turns out, that the crest lines of the distance function, or equivalently the SKIZ, coincide with these watershed lines.

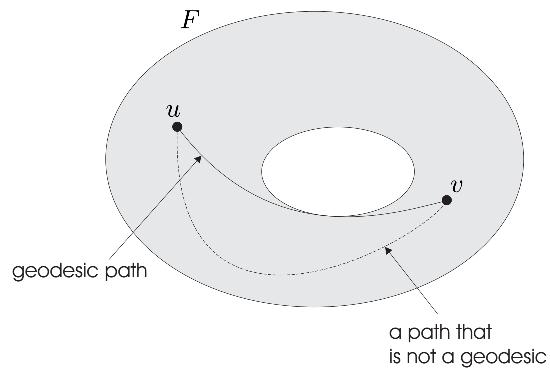

Figure 3.33: *Geodesic path between two points u and v in a binary image F.*

3.7.4 Geodesic SKIZ

Although the SKIZ is an effective tool for segmenting binary images of nonoverlapping particles, what happens when particles overlap? We answer this question in this subsection. However, we first need to modify the notion of distance between two points u and v in $\mathbb{R}^2$.

Consider two points u, v inside a binary image $F \subseteq \mathbb{R}^2$. A *path* in F between u and v is any curve joining these two points that is always in F. If the points u, v can be connected by a path in F, then there exists a path joining u and v whose length is not greater than the length of any other path with the same endpoints. This path is called a *geodesic path.* See Fig. 3.33 for an example. Given two points $u, v \in F$, the length of the geodesic path connecting these two points is called the *geodesic distance* between u and v, and is denoted by $d_F(u, v)$. If there exists no geodesic path between u and v, we set $d_F(u, v) = \infty$.

Let us now assume that we need to separate two overlapping grains F_1 and F_2, like the ones depicted in Fig. 3.34(a). Let us also assume that we can mark the two grains with two markers M_1 and M_2, respectively. Based on the geodesic distance $d_F(u, v)$ between two points $u, v \in F = F_1 \cup F_2$, we define the *geodesic influence zone* $Z_F(M_k)$ of a marker M_k in F as the collection of all points in F which are closer, in terms of the geodesic distance, to M_k than to any other marker of F. Clearly,

$$Z_F(M_k) = \{u \in F \mid GD_{F,M_k}(u) < GD_{F,M_l}(u), \text{ for every } l \neq k\},$$

where $GD_{F,M_k}(u)$ denotes the *geodesic distance transform* in F of marker M_k at a point $u \in F$, given by

$$GD_{F,M_k}(u) \;=\; \bigwedge_{v \in M_k} d_F(u, v).$$

Subtracting from F the union of the influence zones of all markers in F, we

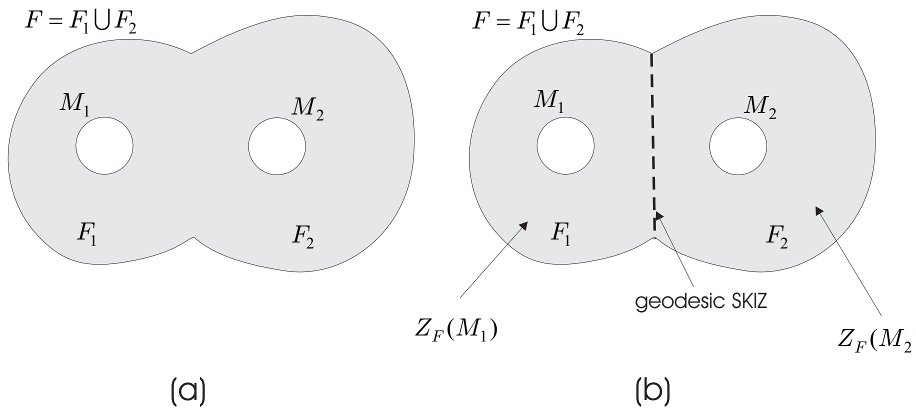

Figure 3.34: *(a) Two overlapping grains F_1 and F_2 that need to be separated – these grains have been marked by two markers M_1 and M_2; (b) segmentation obtained by means of the geodesic SKIZ.*

obtain the *geodesic SKIZ*, given by

$$SKIZ_F(M) = F \setminus \bigcup_k Z_F(M_k).$$

It is not difficult to see that the geodesic SKIZ can be computed by extracting the ridges, or crest lines, of the geodesic distance transform $GD_{F,\cup_k M_k}(u)$. Clearly, the geodesic SKIZ can be used to segment partially overlapping particles, as illustrated in Fig. 3.34(b). However, the segmentation result depends strongly on the choice for the markers.

To illustrate a method for choosing appropriate markers, let us consider the simple case of two partially overlapping disks F_1 and F_2 of the same radius, like the ones depicted in Fig. 3.35(a). We can mark these two disks by their centers. Then, the geodesic SKIZ, based on these markers, provides the desirable segmentation. The centers of the two disks can be easily obtained by means of the distance transform: we first calculate the distance transform $D_{F^c}(u)$, where $F = F_1 \cup F_2$; the desirable disk centers can then be computed as the two points in F where D_{F^c} assumes its maximum value. This simple example suggests that appropriate markers for segmenting a binary image F of overlapping particles based on the geodesic SKIZ can be obtained by means of determining the *peaks*, or *regional maxima*, of the distance transform $D_{F^c}(u)$. Recall that a peak, or regional maximum, M of a grayscale image f is a connected component of pixels in f with a given grayscale value v, such that, every pixel in the neighborhood of M has a value strictly smaller than v. However, keep in mind that this approach may produce misleading results. This is clear from the example depicted in Fig. 3.35(b).

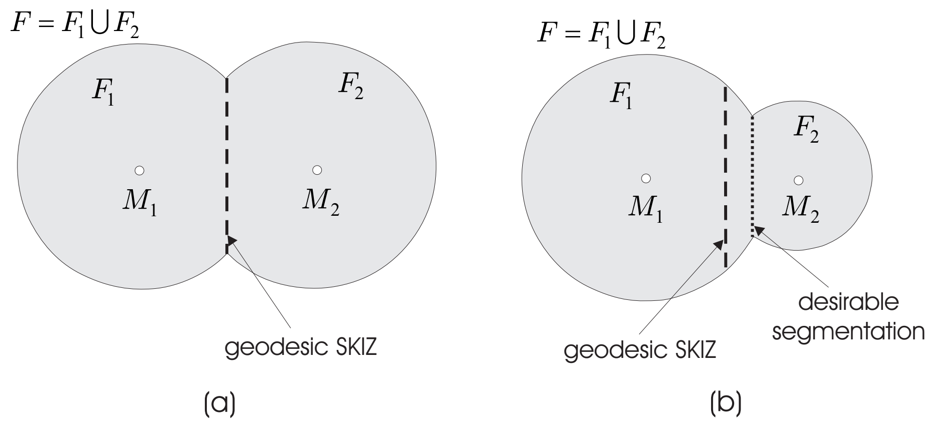

Figure 3.35: *(a) Two overlapping disks with the same radius, marked by their centers, and the segmentation obtained by means of the geodesic SKIZ. (b) The geodesic SKIZ produces the wrong segmentation result when the radius of one of the two disks is reduced.*

3.7.5 Watershed-based segmentation of overlapping particles

An alternative technique for segmenting overlapping particles, which avoids use of the geodesic SKIZ, is based on the watershed transform. Given a binary image F of overlapping particles, like the one depicted in Fig. 3.36(a), we calculate the negative distance transform $-D_{F^c}(u)$; see Fig. 3.36(b). Notice that the regional minima of this grayscale function appear at points in F which are the farthest away from F^c. The catchment basins of $-D_{F^c}(u)$ clearly mark the different regions into which F is to be segmented.

Now, we pierce the topographic surface of $-D_{F^c}(u)$ at the location of its regional minima, and we immerse it slowly into water. Water starts flooding the catchment basins. To prevent merging of water coming from two adjacent catchment basins, we erect dams. Once the surface is totally immersed into water, the top of the erected dams provides the watershed lines, which, in turn, segment the image into the desirable regions; see Fig. 3.36(c). Notice that the watershed transform is not applied on the distance transform $D_F(u)$, as it was done in the case of nonoverlapping particles, but on the negative distance transform $-D_{F^c}(u)$. The watershed lines thus produced do not necessarily coincide with the geodesic SKIZ.

3.7.6 Grayscale segmentation

The watershed transform can be applied to the problem of grayscale segmentation as well, in order to partition a grayscale image into regions of interest. Usually, these regions correspond to areas of relatively homogenous grayscale variation. In this case, image segmentation is achieved by means of a watershed-based technique similar to the one used in the binary case. For

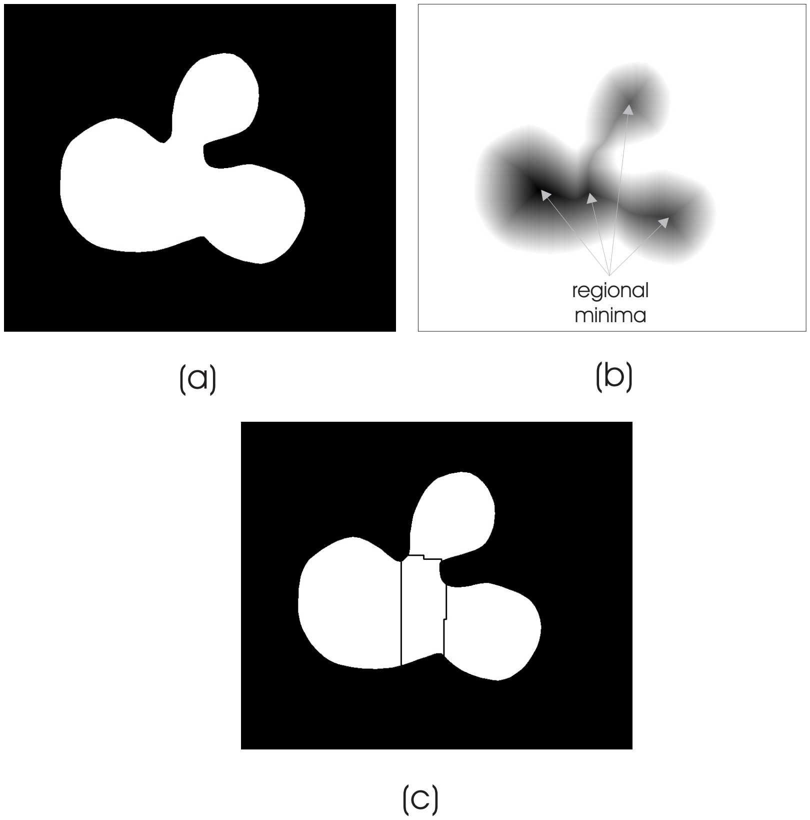

Figure 3.36: *Binary watershed segmentation: (a) a binary image F of overlapping particles; (b) the negative distance transform $-D_{F^c}(u)$ – notice the location of the regional minima; (c) the watershed lines, overlaid on F.*

example, a function f_o may be constructed from f, with crest lines that coincide with the contours of the regions of interest and catchment basins that mark these regions; see Fig. 3.37. Then, the crest lines of f_o are extracted by means of the watershed transform applied on f_o. By construction, the watershed lines will coincide with the desirable region contours.

Despite the simplicity of the previous approach, construction of the appropriate function f_o is a rather challenging and delicate matter. To say that a region of interest in an image f has a "relatively homogeneous" grayscale variation, we mean that there is only slight variation in grayscale values inside the region, or that it has a low gradient. On the other hand, high gradient values often indicate region contours. Therefore, f_o can be taken to be the gradient of f (or more precisely its magnitude); see Fig. 3.37. The crest lines of f_o, extracted by means of the watershed transform, will then provide the desirable segmentation result.

Usually, watershed-based segmentation, using the gradient of the original

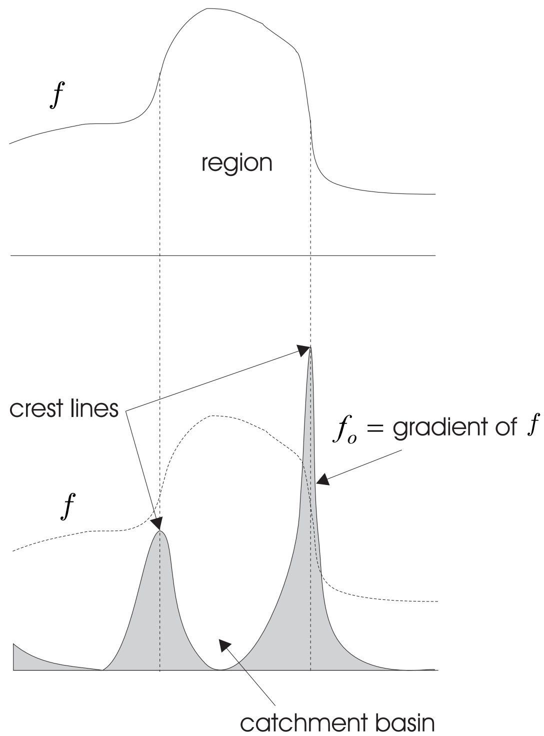

Figure 3.37: *Mapping regions and region contours in f to the catchment basins and crest lines of the gradient of f.*

image, leads to an *oversegmentation* problem. This is primarily due to the sensitivity of the gradient operator to grayscale variation and noise, creating a large number of irrelevant regional minima (catchment basins). This is illustrated in Fig. 3.38. Notice that the relevant contours are buried inside a dense net of irrelevant ones.

One way to ameliorate this problem is to simplify the original image before the gradient is calculated. This may reduce the number of regional minima while preserving the most relevant ones. This is illustrated in Fig. 3.39. The original image f, depicted in Fig. 3.39(a), is pre-filtered by means of the opening by reconstruction operator (3.32) followed by the closing by reconstruction operator (3.33). The structuring element A in (3.32) and (3.33) is taken to be a disk with a diameter of 19 pixels. The result is depicted in Fig. 3.39(b). This effectively "flattens" the image f. The morphological gradient is now applied on the image in (b) and produces the result depicted in Fig. 3.39(c). The result is clearly crisper than the one depicted in Fig. 3.38(b). Subsequent watershed-based segmentation produces the result depicted in Fig. 3.39(d), which contains far less oversegmentation artifacts. However, the result is still not satisfactory.

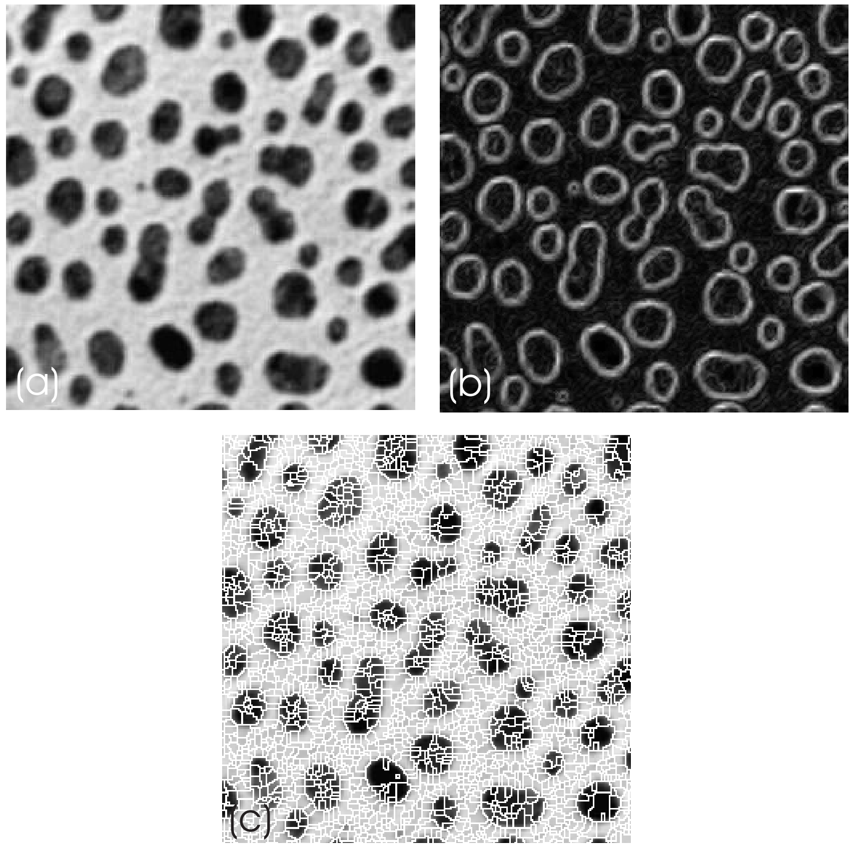

Figure 3.38: *Oversegmentation as a result of watershed-based segmentation using the morphological gradient: (a) original image f; (b) the result of the morphological gradient applied on f; (c) the resulting watershed lines, overlaid on f.*

Better segmentation may be obtained by constraining the regions where the watershed lines might occur. This idea can be implemented by means of an algorithm that employs *internal* and *external* binary markers, which are used to constrain the implementation of the watershed transform, when applied on the gradient image f_o. This approach is illustrated in Fig. 3.40. The first step of this algorithm is to generate an *internal binary marker* F^m_{int}, which marks the regions of interest in a grayscale image f, as the one depicted in Fig. 3.38(a). Towards this goal, we may extract the regional minima of f. We choose to extract the regional minima, since the regions of interest appear as dark cells in f. However, due to noise in f, this step produces a large number of regional minima. If all these minima are used in subsequent steps, they will result in oversegmentation. Therefore, before we extract regional minima, we first simplify f by means of the opening

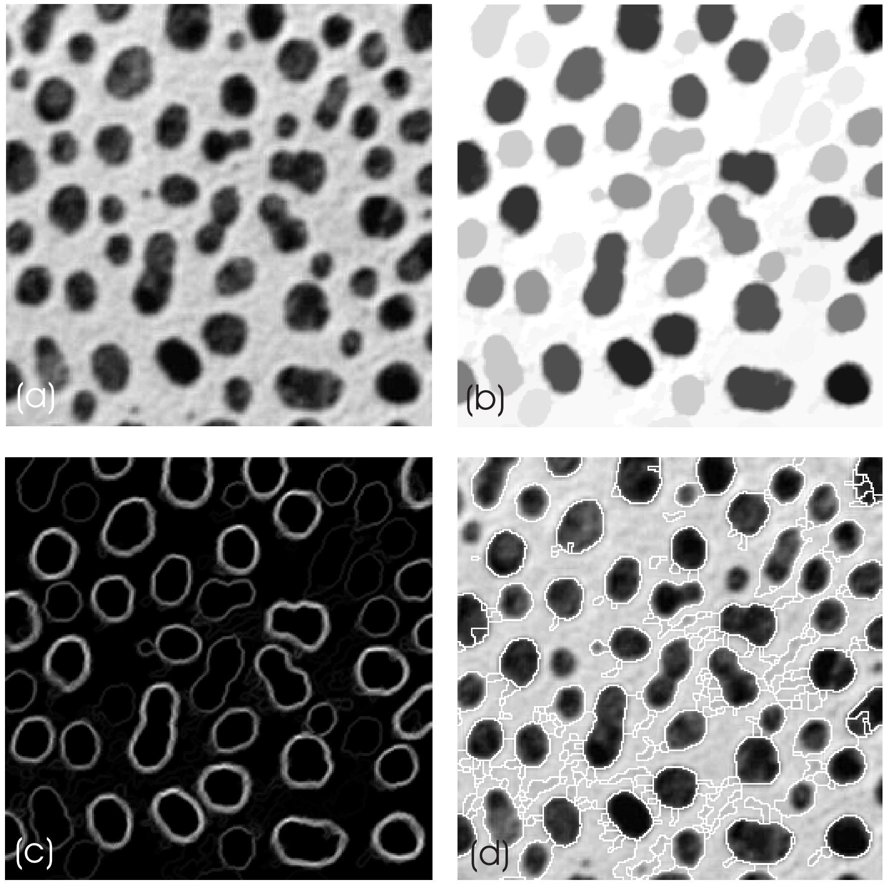

Figure 3.39: *The effect of pre-filtering on watershed-based segmentation, using the morphological gradient as a marker: (a) original image f; (b) the result of pre-filtering f by means of an opening by reconstruction followed by a closing by reconstruction; (b) the result of the morphological gradient applied on the image in (b); (c) the resulting watershed lines, overlaid on f.*

by reconstruction operator (3.32) followed by the closing by reconstruction operator (3.33). The structuring element A in (3.32) and (3.33) is taken to be a disk with a diameter of 11 pixels. The result is depicted in Fig. 3.40(a). The internal marker F^m_{int} is now taken to be the regional minima of the grayscale image in (a). This marker is depicted in Fig. 3.40(b).

The next step is to generate an *external binary marker* F^m_{ext}, which marks the highest crest lines of the original image f that separate the regional minima in (b). Such a marker can be obtained by piercing the topographic surface of f at the points of the regional minima depicted in Fig. 3.40(b), by immersing the subgraph of f into water, and by detecting the resulting watershed lines. The result of this process is de-

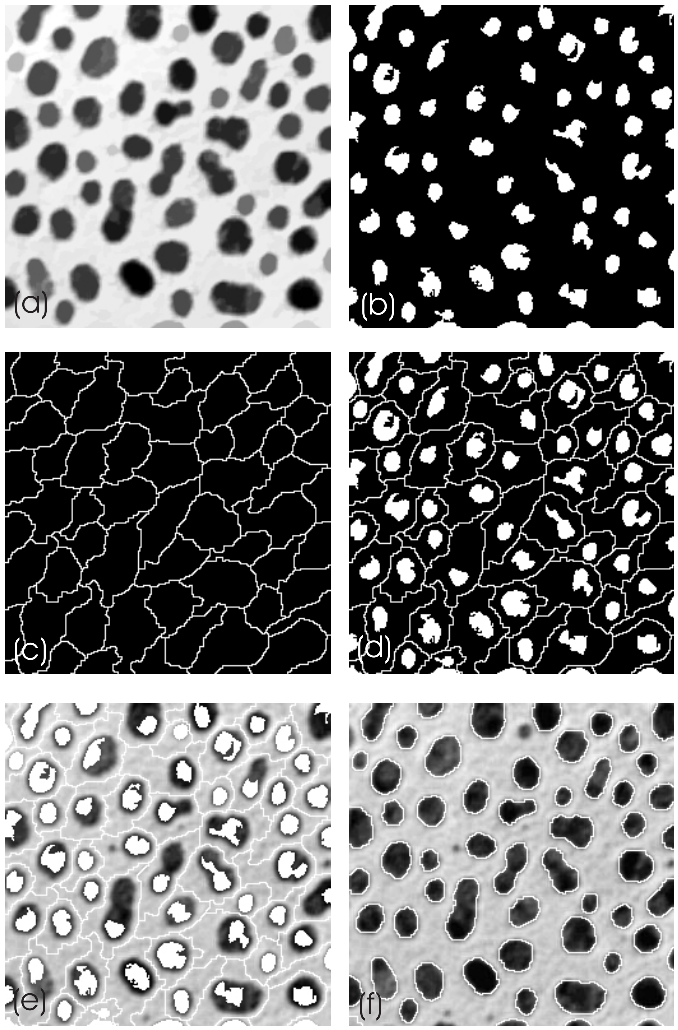

Figure 3.40: *Watershed-based segmentation constrained by internal and external markers: (a) the result of pre-filtering the image f, depicted in Fig. 3.38(a), by means of an opening by reconstruction followed by a closing by reconstruction; (b) the internal marker containing the regional minima of the image in (a); (c) the external marker containing the watershed lines obtained by piercing the topographic surface of f at the points of the regional minima in (b) and by immersing the subgraph of f into water; (d) the combined internal and external markers; (e) the combined internal and external markers overlaid on f; (f) the watershed lines obtained by piercing the topographic surface of the morphological gradient of f, depicted in Fig. 3.38(b), at the points of the combined marker in (d), and by immersing the subgraph of the morphological gradient into water.*

picted in Fig. 3.40(c). Figure 3.40(d) depicts the combined binary marker $F^m = F^m_{\text{int}} \cup F^m_{\text{ext}}$, whereas Fig. 3.40(e) depicts F^m overlaid on the original image. Notice that the cell boundaries are constrained between the external and internal markers. These boundaries can now be detected as the highest crest lines of the morphological gradient of the original image, depicted in Fig. 3.38(b), constrained by the internal and external markers. To detect these lines, we pierce the topographic surface of the morphological gradient $1/2[f \oplus B - f \ominus B]$ at all points of the combined marker F^m in Fig. 3.40(d), we immerse the subgraph into water, and detect the resulting watershed lines. The result of this process is depicted in Fig. 3.40(f). Clearly, the overall algorithm produces an excellent segmentation result, especially when compared to the results depicted in Figs. 3.38(c) and 3.39(d).

The watershed transform can be classified as a region-based segmentation approach. Its success relies heavily on the appropriate choice for the grayscale image f_o and on the choice for the binary markers used for piercing the topographic surface of f_o. Clearly, these choices depend on the particular segmentation problem at hand. Another important issue is the fact that the watershed transform is one of the most time consuming operations of mathematical morphology. In an attempt to speed-up computations, a number of algorithms (serial and parallel) have been proposed in the literature that deal with specific implementation issues. The interested reader is referred to [100] for a survey. For more information on watershed-based segmentation techniques, the reader is referred to [80, 101–108].

3.7.7 Examples

The watershed transform is a powerful tool for extracting regions of interest from a given image. In the following, we illustrate this by means of two examples: segmentation of MR images of the prostate and segmentation of the left ventricle in tagged MR images of the heart.

Segmentation of MR images of the prostate.

This example illustrates the use of the watershed transform for segmenting MR images of the prostate, like the one depicted in Fig. 3.41(a). Here, we are interested in segmenting major anatomical features, such as the prostate, the rectum, and the Denonvillies fascia (which separates the prostate from the anterior surface of the rectum). In this application, segmentation is very important for pre- and post-operative assessment of the prostate. For more information on this imaging technique, the reader is referred to [109]. Figure 3.41(a) depicts an MR image of the prostate with labeling indicating the three regions of interest. Our main objective is to automatically determine a set of internal and external markers that can be used for a successful watershed-based segmentation. Figure 3.41(b) depicts the negative of the

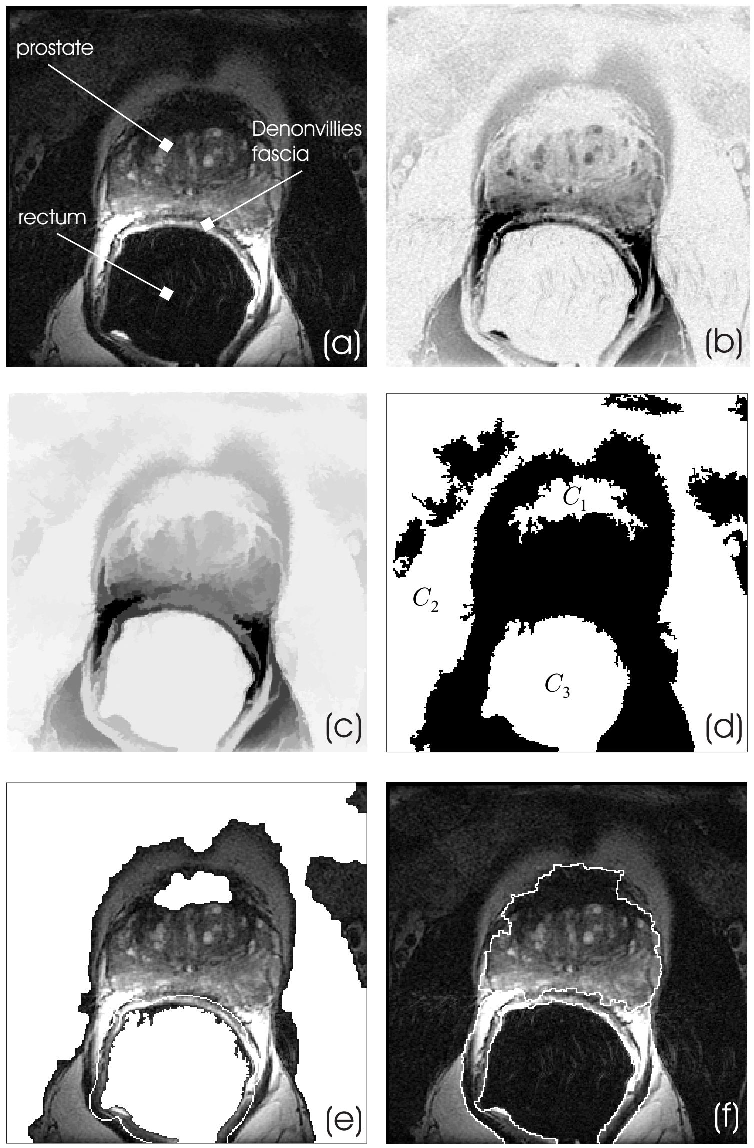

Figure 3.41: *Segmentation of an MR image of the prostate: (a) original image with three labeled anatomical features; (b) the negative of the image in (a); (c) the result of applying an opening by reconstruction followed by a closing by reconstruction on the image in (b); (d) the result of thresholding the image in (d); (e) the combined internal and external markers (in white) obtained from the image in (d), overlaid on the original image in (a); (f) the watershed lines, overlaid on the original image in (a). – Data courtesy of Clare Tempany, MD, Director of Clinical MRI, Brigham and Women's Hospital, Harvard University. Used with permission.*

image in (a). Notice that, in this image, the regions of interest are characterized by high graylevel values, as compared to the gray values associated with the tissues surrounding the prostate and rectum. Thresholding will produce appropriate markers for these regions. However, before thresholding is applied, we need to reduce the graylevel variation within individual regions. To accomplish this goal, the image in (b) is subjected to the opening by reconstruction operator (3.32), followed by the closing by reconstruction operator (3.33). The structuring element A in (3.32) and (3.33) is taken to be a disk with a diameter of 11 pixels. The result is depicted in Fig. 3.41(c). Thresholding now produces the binary image depicted in Fig. 3.41(d), from which the required markers will be extracted. Notice that this image consists of 3 connected components, labeled C_1, C_2 and C_3. First, the holes in C_2 are closed by means of the binary close-hole operator (3.30). Then, the resulting image is slightly shrunk, by means of a binary erosion by a disk structuring element with a diameter of 3 pixels, and the result is smoothed-out by means of a structural opening by a disk structuring element with a diameter of 9 pixels. Notice that the smoothed component C_1 can serve as an internal marker for the prostate, the smoothed component C_2 can serve as an external marker for the prostate, whereas the smoothed component C_3 can serve as an internal marker for the rectum. What is left to do is to obtain an external marker for the rectum. This can be easily obtained from C_3. By applying area opening operators, we can extract the smoothed internal rectum marker C_3 from the image in (d). The dilation of this marker by a disk structuring element with a diameter of 15 pixels is subtracted from the dilation of the marker by a disk structuring element with a diameter of 17 pixels. This produces a ring that surrounds the internal rectum marker and lies outside the rectum, in close proximity to its boundary. This ring can now serve as the desirable external rectum marker. Figure 3.41(e) depicts the combined marker (in white), overlaid on the original image in (a). Using this marker, the topographic surface of the internal morphological gradient of the image in (a) is pierced at the points determined by this marker, and the subgraph is immersed into water. The detected watershed lines are depicted in Fig. 3.41(f), overlaid on the original image in (a). Clearly, watershed-based segmentation is successful in segmenting the original image into the three desirable regions of interest.

We should point-out that the result depicted in Fig. 3.41(f) is not clinically validated. Further processing may be required in order to obtain a clinically acceptable segmentation result. However, the segmentation result depicted in Fig. 3.41(f) is obtained automatically in less than 1 second, when implemented using MatLab® on a Windows NT based system, equipped with a Xeon 400MHz processor, and can serve as an initialization for more accurate model-based segmentation techniques, if necessary.

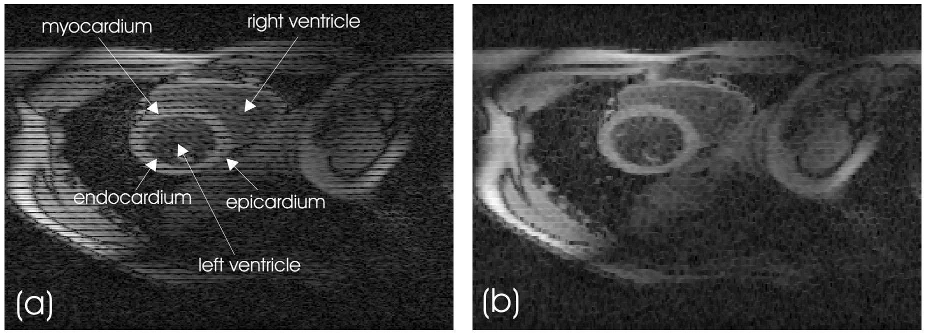

Figure 3.42: *(a) A slice of a tagged MR image of the heart – tag lines appear in black. (b) The result of applying a grayscale structural closing by a vertically oriented* 3*-pixel-wide linear structuring element to the image in (a) – all tag lines have been successfully removed. – Data courtesy of E. R. McVeigh, Department of Biomedical Engineering and Radiology, The Johns Hopkins University. Used with permission.*

Segmentation of tagged MR images of the heart.

In this example, we illustrate the use of marker-driven watershed-based segmentation for the extraction of major anatomical features of the left ventricle from tagged MR images of the heart. The main application concerns *cardiac image analysis*, where estimation of cardiac motion and deformation is of interest (see also Chapter **??** in this volume, for more details on this subject). The example discussed here is interesting in several respects. Primarily, it is concerned with segmentation in a special class of MR imaging aiming at characterizing heart motion. Accurate segmentation helps identify and track the location of key anatomical features associated with the left ventricle. Segmentation is applied to a sequence of images tracking heart motion in its contraction cycle. In this respect, the time evolution of boundaries in several short-axis slices spanning the entire left ventricle is investigated. The resulting procedure is iterative in that the initial segmentation is refined during a second pass by using the results of the first pass to derive an improved set of markers. Alternative segmentation techniques for tagged MR images of the heart are discussed in Chapter **??** of this volume.

The tagged MR imaging technique has been introduced by Zerhouni et. al. in 1988 [110]. The procedure is based on temporarily marking tissue by means of electro-magnetic modulation. Typically, few millimeter apart parallel sheets of "tag surfaces," orthogonal to the image plane, are utilized. The intersection of these surfaces from orthogonal directions provides marks in 3D space. Tracking the motion of these marks helps visualize and characterize heart function abnormalities in a non-invasive fashion [111] (see also Chapter **??** in this volume).

A slice of a tagged MR image of the heart is depicted in Fig. 3.42(a). In this image, tag lines appear as black. A short axis basal view of the left ventricle is used. This makes the left ventricle appear as a round object. Here, we are interested in segmenting three major anatomical features of the heart, namely the left ventricle, and the inner and outer walls of the myocardium (i.e., the wall surrounding the left ventricle), known as endocardium and epicardium, respectively. The image in Fig. 3.43(a) is taken right after tagging, prior to any heart motion. Therefore, the tag lines appear as straight parallel lines. However, the tag lines deform in time according to the contraction of heart muscle. These marks are part of the image and may interfere with a segmentation technique used for the extraction of the left ventricle and its wall. To remedy this situation, we remove the tag lines by means of a grayscale structural closing using a 3-pixel-wide linear structuring element, orthogonal to the tag lines. As shown in Fig. 3.42(b), this operation is quite successful in removing the tag lines while preserving the anatomical features of interest (e.g., the left ventricle, the endocardium and the epicardium).

The main purpose of this example is to demonstrate the use of watershed-based segmentation for extracting the left ventricle, as well as the endocardium and epicardium, in a number of slices as a function of time. The data used for this example consists of 6 slices, each slice producing 10 images (frames) as a function of time. First, we need to come-up with the appropriate set of markers: an internal marker, located within the left ventricle, an intermediate one, buried inside the myocardium, and an external marker circumscribing the epicardium. The highest crest line of the gradient of the original image, located in between the external and the intermediate markers, will be the watershed approximation of the epicardium. Similarly, the highest crest line of the gradient image located in between the internal and the intermediate markers will be the watershed approximation of the endocardium. Clearly, the success of the watershed-based segmentation procedure strongly depends on the accurate determination of these markers in each slice and all time frames.

We use a robust technique, based on mathematical morphology, to find these markers. The approach is based on the observation that the myocardium appears as a ring shaped object (see Fig. 3.42(a)). Despite a noticeable deformation during the contraction cycle, the cavity within the myocardium is a persistent attribute in all slices. The cavities present in the first time frame of each slice are extracted by using a simple *close-hole top-hat* operator $\psi_{\mathrm{cloholeth}}$, based on the grayscale close-hole operator ψ_{clohole} in (3.34); namely,

$$\psi_{\mathrm{cloholeth}}(f) = \psi_{\mathrm{clohole}}(f) - f. \tag{3.38}$$

The resulting image, depicted in Fig. 3.43(a), for a slice close to the base

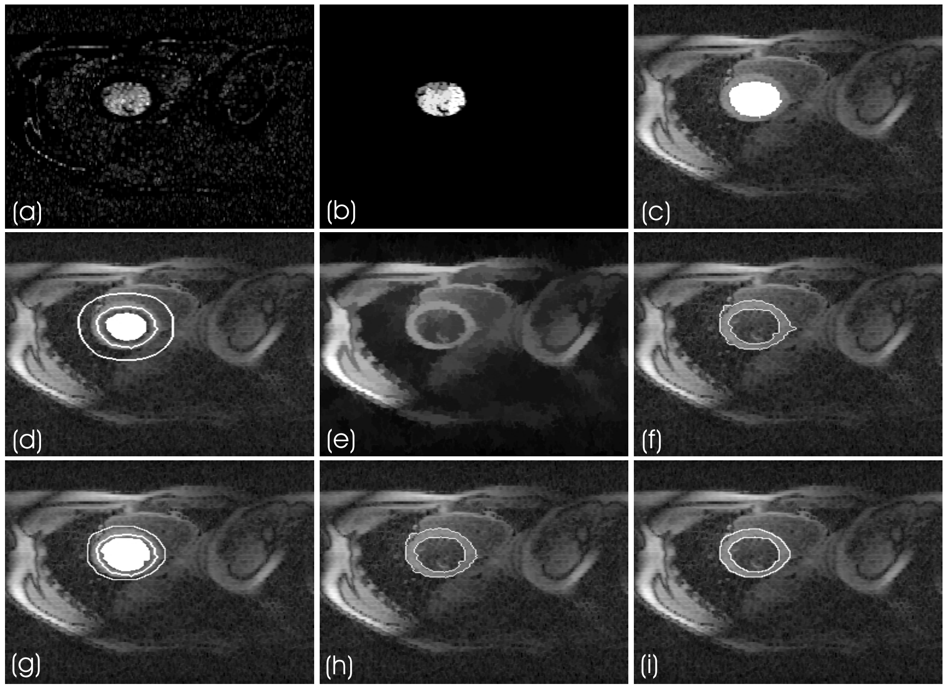

Figure 3.43: *(a) The result of the close-hole top-hat operator (3.38), applied on the image depicted in Fig. 3.42(b). (b) The result of grayscale area opening applied on the image in (a). (c) The result of applying a binary alternating filter on the thresholded version of the image in (b). (d) The internal, intermediate, and external left ventricle markers obtained from the binary image in (c). (e) A simplified version of the image depicted in Fig. 3.42(b) obtained by means of a grayscale alternating sequential filter based on opening and closing by reconstruction operators. (f) The watershed lines obtained by applying the watershed transform on the internal morphological gradient of the image in (e) marked by the markers in (d). (g) A tighter set of markers obtained by a morphological manipulation of the result in (f). (h) The watershed lines obtained by applying the watershed transform on the internal morphological gradient of the image in (e) marked by the markers in (g). (i) Final segmentation obtained by smoothing the watershed lines in (h).*

of the heart, is processed by the grayscale area opening operator (3.25), with $\alpha = 200$, which eliminates unwanted debris. The result is depicted in Fig. 3.43(b). Notice that, the only remaining object resides within the left ventricle cavity. Simple thresholding, followed by an application of the binary alternating filter $\Pi_k(F)$ in (3.18), with $k = 2$ and B being a 3-pixel-wide square structuring element, produces the binary image depicted in Fig. 3.43(c), overlaid on the image depicted in (b). This binary image serves as an initial estimate of the endocardial marker. It will be used to provide the actual internal, the intermediate, and the external markers needed by the watershed transform. The inner marker is obtained via eroding this image by a disk structuring element with a diameter of 9 pixels. The intermediate and outer markers are obtained by extracting the boundaries of the dilations of the same image by a 9-pixel-wide cross structuring element and by a 39-pixel wide disk structuring element, respectively. The sizes of the structuring elements are chosen such that, the internal marker always exists, the intermediate marker always stays within the myocardium, and the external marker does not intersect with the epicardium. The resulting markers are depicted in Fig. 3.43(d) as an overlay. The watershed transform is now applied on the internal morphological gradient of the image depicted in Fig. 3.43(e) (and not on the gradient of the image in (b) to avoid oversegmentation) and produces the result depicted in Fig. 3.43(f). The image in (e) is obtained by applying a variant of the grayscale alternating sequential filter $\rho_k(f)$, discussed in Subsection 3.4.11. The main difference between this filter and the traditional alternating sequential filter is that the opening is replaced by opening by reconstruction, and the closing is replaced by closing by reconstruction. The filter effectively reduces grayscale variation within homogeneous regions, as is evident by comparing Figs. 3.42(b) and 3.43(e). We use a filter of order $k = 3$ and a disk structuring element with a diameter of 3 pixels. Notice that, the watershed transform does a satisfactory job at locating the endocardium and epicardium. However, the resulting segmentation starts to deteriorate for slices closer to the heart's apex and for time frames taken at a later stage of the contraction. The problem associated with extracting the epicardium is due to the contact points of the left and right ventricles, as well as on the intermixing of the heart's boundary with the silhouettes of other structures during the contraction phase. On the other hand, the problem associated with extracting the endocardium is associated with the appearance of papillary muscles in the left ventricle.

To improve the quality of segmentation, the initial watershed lines in Fig. 3.43(f) are used to construct a tighter set of markers. This is achieved by first filling-in the interior and exterior portions of the watershed curves, by using the binary close-hole operator (3.30). Then, the shape corresponding to the exterior watershed line is dilated by a disk structuring element with a diameter of 23 pixels. The boundary of the resulting shape is used as the new external marker. The new internal marker is obtained by eroding the filled-in internal watershed line by a disk structuring element with a diameter of 3 pixels. The intermediate marker is kept the same. The aggregation of the new internal, intermediate, and external markers is depicted in Fig. 3.43(g). Notice how tight the new set of markers is, as compared to the ones shown in (d). The result of the watershed transform, applied on the same gradient image with the new set of markers, is depicted in Fig. 3.43(h).

The improvement in extracting the epicardium is evident. Extraction of the endocardium is very satisfactory, even during the first pass, and does not improve much during the second pass.

Due to the inherent noise in the imaging system, tagging artifacts and overlapping anatomical features, the segmentation is not very smooth. We address this problem by applying a morphological opening on the interior of the exterior watershed line, by a disk structuring element with a diameter of 23 pixels, and by using the boundary of the result as the final segmentation of the epicardium. Similarly, the inner watershed line is smoothed by closing the result of the filling by a disk structuring element with a diameter of 17 pixels and by extracting the boundary. The resulting segmentation is depicted in Fig. 3.43(i).

A close-up of the final segmentation results, for selected set of slices at different time frames, is depicted in Fig. 3.44. These results are comparable in quality with results obtained by other methods (e.g., based on deformable contour models – see Chapter **??** in this volume). However, watershed-based segmentation can be implemented in a fraction of time than other comparable methods. In fact, our implementation using MatLab® on a Windows NT based system, equipped with a Xeon 400MHz processor, took less than 4 seconds per frame. This is fast, considering the complexity of the problem under consideration and the use of a high-level interpreted language, like MatLab®.

Finally, we would like to point-out here that, although the algorithm discussed in this example requires specification of the shape and size of a number of structuring elements (which seems to be case depended), in reality these parameters can be extracted from the data, by deriving bounds on the shape and size of the myocardium as appears in all slices and frames.

3.8 Conclusions and further discussion

In this chapter, we presented fundamental concepts and techniques of a nonlinear tool for image analysis known as mathematical morphology, and illustrated its use with a number of examples. The current literature reveals extensive use of mathematical morphology in biomedical image analysis applications (e.g., see [20–53]). However, it has been mostly limited to simple morphological operators, like structural erosions, dilations, openings, and closings. Accurate and efficient solutions to a number of biomedical imaging problems can be obtained by employing more advanced morphological tools, like the morphological skeleton, the discrete size transform and pattern spectrum, morphological image reconstruction operators, and the watershed transform. To some extent, this has been demonstrated in this chapter with a few examples.

Due to space limitation, we did not discuss extensions of 2D morphology

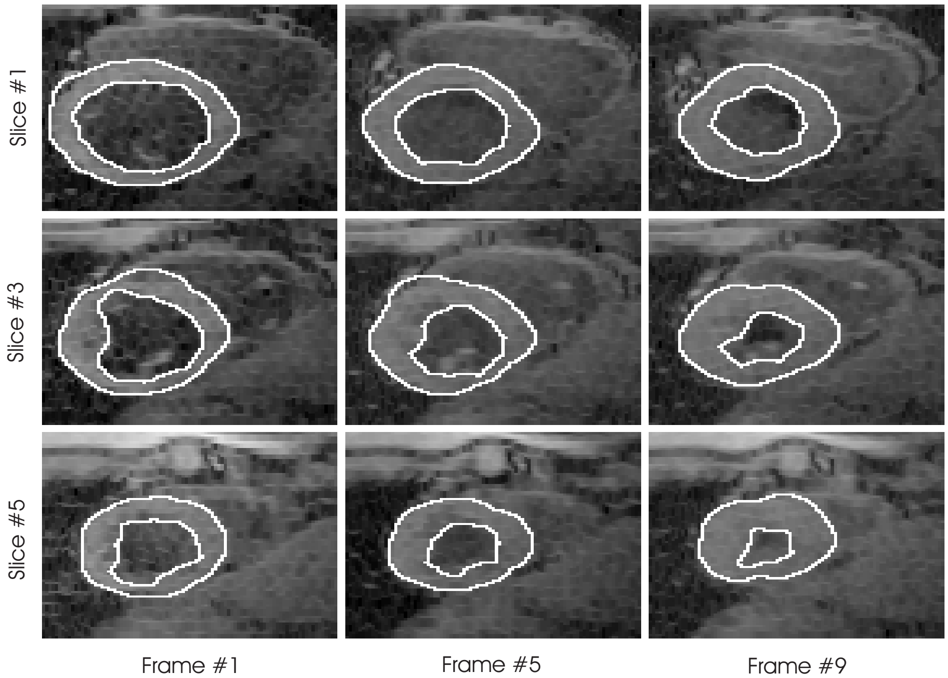

Figure 3.44: *A close-up of final segmentation results for selected tagged MR slices of the heart, at different time frames. – Data courtesy of E. R. McVeigh, Department of Biomedical Engineering and Radiology, The Johns Hopkins University. Used with permission.*

to 3D (see [31]), morphological sampling and discretization [112–114], mathematical morphology on graphs [115,116], and mathematical morphology for vector-valued images [117], multivalued images [118], and image sequences [119]. Moreover, we did not discuss some recent developments, like the theory of connected operators (which include, as a special case, the morphological image reconstruction operators discussed in Section 3.6) [120–125], multiscale morphological image decomposition schemes (morphological pyramids and wavelets) [126–131], and morphological scale-spaces [132–136]. These new tools show great potential for solving complex biomedical image analysis problems.

Of particular interest to applying mathematical morphology methods to problems in biomedical image analysis are recent investigations on the relationship between curve evolution [137–139], level set methods [140, 141], differential morphology [142,143], and nonlinear *partial differential equations* (PDEs) (see also [144–147]). *Curve evolution* studies propagation of curves as a function of time, by using techniques from differential geometry. It is used for the development of geometric models for active contours, which are important in medical image segmentation problems (e.g., see [148] and

Chapter **??** in this volume). *Level set methods* lead to algorithms for the efficient implementation of curve evolution and produce numerical schemes for solving the PDEs underlying geometric active contour models (see also Chapter **??** in this volume). Finally, *differential morphology* studies the problem of describing morphological operators via nonlinear PDEs. In a recent paper [147], the theoretical and algorithmic relationship between curve evolution, level set methods, differential morphology, and nonlinear PDE theory has been investigated. It has been identified that the distance transform can be used to relate differential morphology and curve evolution to a particular type of a nonlinear PDE, the so-called *eikonal* PDE. These results indicate that mathematical morphology is directly related to various differential geometric models, which have been extensively used in medical image analysis problems.

Virtually, all currently available image processing and analysis software packages are capable, to a certain extent, of analyzing images by means of morphological operators. The following list provides a typical sample.

- Aphelion
  (http://www.aai.com)
  A very sophisticated stand-alone image analysis and understanding software with a large number of morphological operators (for Windows NT/98/95 systems).

- CVIPtools [96]
  (http://www.ee.siue.edu/CVIPtools)
  A free software package, developed at Southern Illinois University at Edwardsville (for UNIX and Windows NT/98/95 systems). Contains a limited number of morphological operators.

- MegaWave
  (http://www.cmla.ens-cachan.fr/Cmla/Megawave)
  A free collection of C functions that, among other things, includes morphological filtering, affine morphological scale spaces, PDE-based segmentation, and snakes (for UNIX systems). This package has been developed at CEREMADE (Centre de Recherches en Mathématiques de la Decision), Université de Paris, Dauphine, France.

- MicroMorph
  (http://cmm.ensmp.fr)
  A highly sophisticated stand-alone software package for mathematical morphology (for Windows NT/98/95 systems). This package has been developed at CMM (Centre de Morphologie Mathématique), Ecole des Mines de Paris, Fontainebleau, France.

- MMACH TOOLBOX FOR KHOROS [149]
  (http://www.khoral.com)
  A highly sophisticated mathematical morphology toolbox for a powerful visual prototyping environment (for UNIX systems).

- NIH IMAGE
  (http://rsb.info.nih.gov/nih-image and http://www.scioncorp.com)
  A free and highly flexible stand-alone image processing and analysis software from the National Institutes of Health (for Mac and Windows NT/98/95 systems). Contains a limited number of morphological operators.

- SDC MORPHOLOGY TOOLBOX FOR MATLAB®
  (http://www.mmorph.com and http://www.mathworks.com)
  A highly sophisticated mathematical morphology toolbox, similar to MMach, for a popular prototyping environment (for UNIX and Windows NT/98/95 systems).

3.9 Acknowledgments

This work was supported by the Office of Naval Research, Mathematical, Computer, and Information Sciences Division, under ONR Grant N00014-90-1345, and by the National Science Foundation, under NSF Award #9729576.

The authors would like to thank Professor Edward C. Klatt, Department of Pathology, University of Utah, for kindly permitting use of the images depicted in Figs. 3.3, 3.5–3.7, 3.9, and 3.29, and Clare Tempany, MD, Director of Clinical MRI, Brigham and Women's Hospital, Harvard University, for kindly permitting use of the prostate image depicted in Fig. 3.41. The authors also thank Professor Elliot R. McVeigh, Department of Biomedical Engineering and Radiology, The Johns Hopkins University, for permitting use of the data associated with the "segmentation of tagged MR images of the heart" example of Subsection 3.7.7. Special thanks to *SDC Information Systems* for permitting use of the images depicted in Figs. 3.19 and 3.28. The example depicted in Fig. 3.28 is a slightly modified version of the "mmdfila" demonstration of the *SDC Morphology Toolbox for MatLab®* , and has been replicated here with permission. All simulations have been implemented in MatLab® 5.3 using the SDC Morphology Toolbox for MatLab® , version 0.9.

Finally, the authors are indebted to Henk Heijmans, Roberto Lotufo, and Milan Sonka for providing suggestions on how to improve the manuscript.

3.10 References

[1] A. K. Jain. *Fundamentals of Digital Image Processing*. Prentice Hall, Englewood Cliffs, New Jersey, 1989.

[2] R. C. Gonzalez and R. E. Woods. *Digital Image Processing.* Addison-Wesley, Reading, Massachusetts, 1992.

[3] M. Sonka, V. Hlavac, and R. Boyle. *Image Processing, Analysis, and Machine Vision.* PWS Publishing, Pacific Grove, California, second edition, 1999.

[4] G. Matheron. *Random Sets and Integral Geometry.* John Wiley, New York City, New York, 1975.

[5] J. Serra. *Image Analysis and Mathematical Morphology.* Academic Press, London, England, 1982.

[6] H. J. A. M. Heijmans. *Morphological Image Operators.* Academic Press, Boston, Massachusetts, 1994.

[7] P. Soille. *Morphological Image Analysis: Principles and Applications.* Springer, Berlin, Germany, 1999.

[8] H. J. A. M. Heijmans and C. Ronse. The algebraic basis of mathematical morphology I. Dilations and erosions. *Computer Vision, Graphics, and Image Processing*, 50:245–295, 1990.

[9] C. Ronse and H. J. A. M. Heijmans. The algebraic basis of mathematical morphology II. Openings and closings. *Computer Vision, Graphics, and Image Processing: Image Understanding*, 54:74–97, 1991.

[10] H. J. A. M. Heijmans. Theoretical aspects of gray-level morphology. *IEEE Transactions on Pattern Analysis and Machine Intelligence*, 13:568–582, 1991.

[11] C. Ronse. Why mathematical morphology needs complete lattices. *Signal Processing*, 21:129–154, 1990.

[12] G. J. F. Banon and J. Barrera. Minimal representations for translation-invariant set mappings by mathematical morphology. *SIAM Journal of Applied Mathematics*, 51:1782–1798, 1991.

[13] G. J. F. Banon and J. Barrera. Decomposition of mappings between complete lattices by mathematical morphology, Part I. General lattices. *Signal Processing*, 30:299–327, 1993.

[14] C. R. Giardina and E. R. Dougherty. *Morphological Methods in Image and Signal Processing.* Prentice Hall, Englewood Cliffs, New Jersey, 1988.

[15] E. R. Dougherty. *An Introduction to Morphological Image Processing.* SPIE Optical Engineering Press, Bellingham, Washington, 1992.

[16] J. Serra, editor. *Image Analysis and Mathematical Morphology. Volume 2: Theoretical Advances.* Academic Press, London, England, 1988.

[17] J. Serra and P. Soille, editors. *Mathematical Morphology and its Applications to Image Processing.* Kluwer, Dordrecht, The Netherlands, 1994.

[18] P. Maragos, R. W. Schafer, and M. A. Butt, editors. *Mathematical Morphology and its Applications to Image and Signal Processing.* Kluwer, Boston, Massachusetts, 1996.

[19] H. J. A. M. Heijmans and J. B. T. M. Roerdink, editors. *Mathematical Morphology and its Applications to Image and Signal Processing.* Kluwer, Dordrecht, The Netherlands, 1998.

[20] F. Prêteux, A. M. Laval-Jeantet, B. Roger, and M. H. Laval-Jeantet. New prospects in CT image processing via mathematical morphology. *European Journal of Radiology*, 5:313–317, 1985.

[21] C. Lesty, M. Raphael, L. Nonnenmacher, V. Leblond-Missenard, A. Delcourt, A. Homond, and J. L. Binet. An application of mathematical morphology to analysis of the size and shape of nuclei in tissue sections of non-Hodgkin's lymphoma. *Cytometry*, 7:117–131, 1986.

[22] F. Meyer. Automatic screening of cytological specimens. *Computer Vision, Graphics, and Image Processing*, 35:356–369, 1986.

[23] M. M. Skolnick. Application of morphological transformations to the analysis of two-dimensional electrophoretic gels of biological materials. *Computer Vision, Graphics, and Image Processing*, 35:306–332, 1986.

[24] J. W. Klingler Jr., C. L. Vaughan, T. D. Fraker Jr., and L. T. Andrews. Segmentation of echocardiographic images using mathematical morphology. *IEEE Transactions on Biomedical Engineering*, 35:925–934, 1988.

[25] C. Frances, M. C. Branchet, S. Boisnic, C. L. Lesty, and L. Robert. Elastic fibers in normal human skin. Variations with age: a morphometric analysis. *Archives of Gerontology and Geriatrics*, 10:57–67, 1990.

[26] C. Toumoulin, R. Collorec, and J. L. Coatrieux. Vascular network segmentation in subtraction angiograms: a comparative study. *Medical Informatics*, 15:333–341, 1990.

[27] M. C. Branchet, S. Boisnic, C. Frances, C. Lesty, and L. Robert. Morphometric analysis of dermal collagen fibers in normal human skin as a function of age. *Archives of Gerontology and Geriatrics*, 13:1–14, 1991.

[28] J. G. Thomas, R. A. Peters II, and P. Jeanty. Automatic segmentation of ultrasound images using morphological operators. *IEEE Transactions on Medical Imaging*, 10:180–186, 1991.

[29] V. Conan, S. Gesbert, C. V. Howard, D. Jeulin, F. Meyer, and D. Renard. Geostatistical and morphological methods applied to three-dimensional microscopy. *Journal of Microscopy*, 166:169–184, 1992.

[30] J. S. J. Lee, W. I. Bannister, L. C. Kuan, P. H. Bartels, and A. C. Nelson. A processing strategy for automated Papanicolaou smear screening. *Analytical and Quantitative Cytology and Histology*, 14:415–425, 1992.

[31] F. Meyer. Mathematical morphology: from two dimensions to three dimensions. *Journal of Microscopy*, 165:5–28, 1992.

[32] J. Pladellorens, J. Serrat, A. Castell, and M. J. Yzuel. Using mathematical morphology to determine left ventricular contours. *Physics in Medicine and Biology*, 37:1877–1894, 1992.

[33] M. E. Brummer, R. M. Mersereau, R. L. Eisner, and R. R. J. Lewine. Automatic detection of brain contours in MRI data sets. *IEEE Transactions on Medical Imaging*, 12:153–166, 1993.

[34] Y. Chen, E. R. Dougherty, S. M. Totterman, and J. P. Hornak. Classification of trabecular structure in magnetic resonance images based on morphological granulometries. *Magnetic Resonance in Medicine*, 29:358–370, 1993.

[35] A. Moragas, C. Castells, and M. Sans. Mathematical morphologic analysis of aging-related epidermal changes. *Analytical and Quantitative Cytology and Histology*, 15:75–82, 1993.

[36] M. Sans and A. Moragas. Mathematical morphologic analysis of the aortic medial structure: Biomechanical implications. *Analytical and Quantitative Cytology and Histology*, 15:93–100, 1993.

[37] B. D. Thackray and A. C. Nelson. Semi-automatic segmentation of vascular network images using a rotating structuring element (ROSE) with mathematical morphology and dual feature thresholding. *IEEE Transactions on Medical Imaging*, 12:385–392, 1993.

[38] J. Cardillo and M. A. Sid-Ahmed. An image processing system for locating craniofacial landmarks. *IEEE Transactions on Medical Imaging*, 13:275–289, 1994.

[39] F. Moreso, D. Serón, J. Vitriá, J. M. Grinyó, F. M. Colomé-Serra, N. Parés, and J. Serra. Quantification of interstitial chronic renal damage by means of texture analysis. *Kidney International*, 46:1721–1727, 1994.

[40] W. Böcker, W.-U. Müller, and C. Streffer. Image processing algorithms for the automated micronucleus assay in binucleated human lymphocytes. *Cytometry*, 19:283–294, 1995.

[41] J. A. Giménez-Mas, M. P. Sanz-Moncasi, L. Remón, P. Gambó, and M. P. Gallego-Calvo. Automated textural analysis of nuclear chromatin: A mathematical morphology approach. *Analytical and Quantitative Cytology and Histology*, 17:39–47, 1995.

[42] C. Tsai, B. S. Manjunath, and R. Jagadeesan. Automated segmentation of brain MR images. *Pattern Recognition*, 28:1825–1837, 1995.

[43] G. Wolf, M. Beil, and H. Guski. Chromatin structure analysis based on a hierarchic texture model. *Analytical and Quantitative Cytology and Histology*, 17:25–34, 1995.

[44] M. Beil, T. Irinopoulou, J. Vassy, and J. P. Rigaut. Application of confocal scanning laser microscopy for an automated nuclear grading of prostate lesions in three dimensions. *Journal of Microscopy*, 183:231–240, 1996.

[45] J.-P. Thiran and B. Macq. Morphological feature extraction for the classification of digital images of cancerous tissues. *IEEE Transactions on Biomedical Engineering*, 43:1011–1020, 1996.

[46] A. Elmoataz, S. Schüpp, R. Clouard, P. Herlin, and D. Bloyet. A segmentation method combining mathematical morphology and a level set approach of active contours: Application to localization of objects in medical images. *Acta Stereologica*, 16:223–231, 1997.

[47] S. Kumasaka and I. Kashima. Initial investigation of mathematical morphology for the digital extraction of the skeletal characteristics of trabecular bone. *Dentomaxillofacial Radiology*, 26:161–168, 1997.

[48] A. Mojsilović, M. Popović, N. Amodaj, R. Babić, and M. Ostojić. Automatic segmentation of intravascular ultrasound images: A texture-based approach. *Annals of Biomedical Engineering*, 25:1059–1071, 1997.

[49] P. Bamford and B. Lovell. Unsupervised cell nucleus segmentation with active contours. *Signal Processing*, 71:203–213, 1998.

[50] A. Elmoataz, S. Schüpp, R. Clouard, P. Herlin, and D. Bloyet. Using active contours and mathematical morphology tools for quantification of immunohistochemical images. *Signal Processing*, 71:215–226, 1998.

[51] P. Korn, N. Sidiropoulos, C. Faloutsos, E. Siegel, and Z. Protopapas. Fast and effective retrieval of medical tumor shapes. *IEEE Transactions on Knowledge and Data Engineering*, 10:889–904, 1998.

[52] A. Moragas, M. García-Bonafé, M. Sans, N. Torán, P. Huguet, and C. Martín-Plata. Image analysis of dermal collagen changes during skin aging. *Analytical and Quantitative Cytology and Histology*, 20:493–499, 1998.

[53] S. Baeg, S. Batman, E. R. Dougherty, V. G. Kamat, N. Kehtarnavaz, S. Kim, A. Popov, K. Sivakumar, and R. Shah. Unsupervised morphological granulometric texture segmentation of digital mammograms. *Journal of Electronic Imaging*, 8:65–75, 1999.

[54] P. Maragos and R. W. Schafer. Morphological filters - Part I: Their set-theoretic analysis and relations to linear shift-invariant filters. *IEEE Transactions on Acoustics, Speech, and Signal Processing*, 35:1153–1169, 1987.

[55] J. Astola and E. R. Dougherty. Nonlinear filters. In E. R. Dougherty, editor, *Digital Image Processing Methods*, pages 1–42. Marcel Dekker, New York City, New York, 1994.

[56] D. Zhao and D. G. Daut. Morphological hit-or-miss transformation for shape recognition. *Journal of Visual Communication and Image Representation*, 2:230–243, 1991.

[57] E. R. Dougherty and R. P. Loce. Optimal mean-absolute-error hit-or-miss filters: Morphological representation and estimation of the binary conditional expectation. *Optical Engineering*, 32:815–827, 1993.

[58] J. S. J. Lee, R. M. Haralick, and L. G. Shapiro. Morphologic edge detection. *IEEE Journal of Robotics and Automation*, 3:142–156, 1987.

[59] J.-F. Rivest, P. Soille, and S. Beucher. Morphological gradients. *Journal of Electronic Imaging*, 2:326–336, 1993.

[60] H. J. A. M. Heijmans and C. Ronse. Annular filters for binary images. *IEEE Transactions on Image Processing*, 8:1330–1340, 1999.

[61] H. J. A. M. Heijmans. Composing morphological filters. *IEEE Transactions on Image Processing*, 6:713–723, 1997.

[62] P. Maragos and R. W. Schafer. Morphological filters - Part II: Their relations to median, order-statistic, and stack filters. *IEEE Transactions on Acoustics, Speech, and Signal Processing*, 35:1170–1184, 1987.

[63] J. Serra and L. Vincent. An overview of morphological filtering. *Circuits, Systems and Signal Processing*, 11:47–108, 1992.

[64] M. Vetterli and J. Kovačević. *Wavelets and Subband Coding*. Prentice Hall, Englewood Cliffs, New Jersey, 1995.

[65] P. Maragos. Morphological skeleton representation and coding of binary images. *IEEE Transactions on Acoustics, Speech, and Signal Processing*, 34:1228–1244, 1986.

[66] P. Maragos. Pattern spectrum and multiscale shape representation. *IEEE Transactions on Pattern Analysis and Machine Intelligence*, 11:701–716, 1989.

[67] I. Pitas and A. N. Venetsanopoulos. Morphological shape decomposition. *IEEE Transactions on Pattern Analysis and Machine Intelligence*, 12:38–45, 1990.

[68] J. Goutsias and D. Schonfeld. Morphological representation of discrete and binary images. *IEEE Transactions on Signal Processing*, 39:1369–1379, 1991.

[69] J. M. Reinhardt and W. E. Higgins. Efficient morphological shape representation. *IEEE Transactions on Image Processing*, 5:89–101, 1996.

[70] R. Kresch and D. Malah. Skeleton-based morphological coding of binary images. *IEEE Transactions on Image Processing*, 7:1387–1399, 1998.

[71] D. Schonfeld and J. Goutsias. Optimal morphological pattern restoration from noisy binary images. *IEEE Transactions on Pattern Analysis and Machine Intelligence*, 13:14–29, 1991.

[72] E. R. Dougherty, R. M. Haralick, Y. Chen, C. Agerskov, U. Jacobi, and P. H. Sloth. Estimation of optimal morphological τ-opening parameters based on independent observation of signal and noise pattern spectra. *Signal Processing*, 29:265–281, 1992.

[73] R. M. Haralick, P. L. Katz, and E. R. Dougherty. Model-based morphology: The opening spectrum. *Graphical Models and Image Processing*, 57:1–12, 1995.

[74] K. Sivakumar and J. Goutsias. Discrete morphological size distributions and densities: Estimation techniques and applications. *Journal of Electronic Imaging*, 6:31–53, 1997.

[75] E. R. Dougherty and J. B. Pelz. Morphological granulometric analysis of electrophotographic images-Size distribution statistics for process control. *Optical Engineering*, 30:438–445, 1991.

[76] V. Anastassopoulos and A. N. Venetsanopoulos. The classification properties of the pecstrum and its use for pattern identification. *Circuits, Systems and Signal Processing*, 10:293–326, 1991.

[77] E. R. Dougherty, J. T. Newell, and J. B. Pelz. Morphological texture-based maximum-likelihood pixel classification based on local granulometric moments. *Pattern Recognition*, 25:1181–1198, 1992.

[78] E. R. Dougherty, J. B. Pelz, F. Sand, and A. Lent. Morphological image segmentation by local granulometric size distributions. *Journal of Electronic Imaging*, 1:46–60, 1992.

[79] B. Li and E. R. Dougherty. Size-distribution estimation in process fluids by ultrasound for particle sizes in the wavelength range. *Optical Engineering*, 32:1967–1980, 1993.

[80] L. Vincent and E. R. Dougherty. Morphological segmentation for textures and particles. In E. R. Dougherty, editor, *Digital Image Processing Methods*, pages 43–102. Marcel Dekker, New York City, New York, 1994.

[81] E. R. Dougherty and Y. Cheng. Morphological pattern-spectrum classification of noisy shapes: Exterior granulometries. *Pattern Recognition*, 28:81–98, 1995.

[82] S. Batman and E. R. Dougherty. Size distributions for multivariate morphological granulometries: Texture classification and statistical properties. *Optical Engineering*, 36:1518–1529, 1997.

[83] L. Vincent. Morphological algorithms. In E. R. Dougherty, editor, *Mathematical Morphology in Image Processing*, pages 255–288. Marcel Dekker, New York City, New York, 1993.

[84] L. Vincent. Granulometries and opening trees. *Fundamenta Informaticae*, To Appear, 2000.

[85] H. Blum. A transformation for extracting new descriptors of shape. In W. Wathen-Dunn, editor, *Models for the Perception of Speech and Visual Forms*, pages 362–380. MIT Press, Cambridge, Massachusetts, 1967.

[86] H. Blum. Biological shape and visual science (Part I). *Journal of Theoretical Biology*, 38:205–287, 1973.

[87] L. Vincent. Efficient computation of various types of skeletons. In *Proceedings of the SPIE Conference on Medical Imaging V*, pages 297–311. vol. 1445, San Jose, California, 1991.

[88] F. Y.-C. Shih and O. R. Mitchell. Threshold decomposition of gray-scale morphology into binary morphology. *IEEE Transactions on Pattern Analysis and Machine Intelligence*, 11:31–42, 1989.

[89] L. Vincent. Morphological area openings and closings for grey-scale images. In Y.-L. O, A. Toet, D. Foster, H. J. A. M. Heijmans, and P. Meer, editors, *Shape in Picture: Mathematical Description of Shape in Grey-level Images*, pages 197–208. Springer-Verlag, New York City, New York, 1994.

[90] J. C. Russ. *The Image Processing Handbook. Second Edition.* CRC Press, Boca Raton, Florida, 1995.

[91] Y. Chen and E. R. Dougherty. Gray-scale morphological granulometric texture classification. *Optical Engineering*, 33:2713–2722, 1994.

[92] K. Sivakumar and J. Goutsias. Morphologically constrained GRFs: Applications to texture synthesis and analysis. *IEEE Transactions on Pattern Analysis and Machine Intelligence*, 21:99–113, 1999.

[93] L. Vincent. Fast grayscale granulometry algorithms. In J. Serra and P. Soille, editors, *Mathematical Morphology and its Applications to Image Processing*, pages 265–272. Kluwer, Dordrecht, The Netherlands, 1994.

[94] K. Sivakumar, M. J. Patel, N. Kehtarnavaz, B. Yoganand, and E. R. Dougherty. A constant-time algorithm for erosions/dilations with applications to morphological texture feature computation. *Real-Time Imaging*, To Appear, 2000.

[95] L. Vincent. Morphological grayscale reconstruction in image analysis: Applications and efficient algorithms. *IEEE Transactions on Image Processing*, 2:176–201, 1993.

[96] S. E. Umbaugh. *Computer Vision and Image Processing: A Practical Approach using CVIPtools.* Prentice Hall, Upper Saddle River, New Jersey, 1998.

[97] R. M. Haralick and L. G. Shapiro. *Computer and Robot Vision. Volume I.* Addison-Wesley, Reading, Massachusetts, 1992.

[98] F. Meyer. Skeletons in digital spaces. In J. Serra, editor, *Image Analysis and Mathematical Morphology. Volume 2: Theoretical Advances*, pages 257–296. Academic Press, London, England, 1988.

[99] A. M. López, F. Lumbreras, J. Serrat, and J. J. Villanueva. Evaluation of methods for ridge and valley detection. *IEEE Transactions on Pattern Analysis and Machine Intelligence*, 21:327–335, 1999.

[100] J. B. T. M. Roerdink and A. Meijster. A survey of parallelization strategies for the watershed transform. *Fundamenta Informaticae*, To Appear, 2000.

[101] F. Meyer and S. Beucher. Morphological segmentation. *Journal of Visual Communication and Image Representation*, 1:21–46, 1990.

[102] L. Vincent and P. Soille. Watersheds in digital spaces: An efficient algorithm based on immersion simulations. *IEEE Transactions on Pattern Analysis and Machine Intelligence*, 13:583–598, 1991.

[103] S. Beucher and F. Meyer. The morphological approach to segmentation: The watershed transformation. In E. R. Dougherty, editor, *Mathematical Morphology in Image Processing*, pages 433–481. Marcel Dekker, New York City, New York, 1993.

[104] F. Meyer. Topographic distance and watershed lines. *Signal Processing*, 38:113–125, 1994.

[105] L. Najman and M. Schmitt. Watershed of a continuous function. *Signal Processing*, 38:99–112, 1994.

[106] L. Najman and M. Schmitt. Geodesic saliency of watershed contours and hierarchical segmentation. *IEEE Transactions on Pattern Analysis and Machine Intelligence*, 18:1163–1173, 1996.

[107] N. Michael and R. Arrathoon. Optoelectronic parallel watershed implementation for segmentation of magnetic resonance brain images. *Applied Optics*, 36:9269–9286, 1997.

[108] J. M. Gauch. Image segmentation and analysis via multiscale gradient watershed hierarchies. *IEEE Transactions on Image Processing*, 8:69–79, 1999.

[109] P. Ramchandani and M. D. Schnall. Magnetic resonance imaging of the prostate. *Seminars in Roentgenology*, XXVIII:74–82, 1993.

[110] E. A. Zerhouni, D. M. Parish, W. J. Rogers, A. Yang, and E. P. Shapiro. Human heart: Tagging with MR imaging – A method for noninvasive assessment of myocardial motion. *Radiology*, 169:59–63, 1988.

[111] W. S. Kerwin and J. L. Prince. Cardiac material markers from tagged MR images. *Medical Image Analysis*, 2:339–353, 1998.

[112] R. M. Haralick, X. Zhuang, C. Lin, and J. S. J. Lee. The digital morphological sampling theorem. *IEEE Transactions on Acoustics, Speech, and Signal Processing*, 37:2067–2090, 1989.

[113] H. J. A. M. Heijmans and A. Toet. Morphological sampling. *Computer Vision, Graphics, and Image Processing: Image Understanding*, 54:384–400, 1991.

[114] H. J. A. M. Heijmans. Discretization of morphological operators. *Journal of Visual Communication and Image Representation*, 3:182–193, 1992.

[115] L. Vincent. Graphs and mathematical morphology. *Signal Processing*, 16:365–388, 1989.

[116] H. J. A. M. Heijmans, P. Nacken, A. Toet, and L. Vincent. Graph morphology. *Journal of Visual Communication and Image Representation*, 3:24–38, 1992.

[117] S. S. Wilson. Theory of matrix morphology. *IEEE Transactions on Pattern Analysis and Machine Intelligence*, 14:636–652, 1992.

[118] J. Serra. Anamorphoses and function lattices (multivalued morphology). In E. R. Dougherty, editor, *Mathematical Morphology in Image Processing*, pages 483–523. Marcel Dekker, New York City, New York, 1993.

[119] J. Goutsias, H. J. A. M. Heijmans, and K. Sivakumar. Morphological operators for image sequences. *Computer Vision and Image Understanding*, 62:326–346, 1995.

[120] P. Salembier and J. Serra. Flat zones filtering, connected operators, and filters by reconstruction. *IEEE Transactions on Image Processing*, 4:1153–1160, 1995.

[121] C. Ronse. Set-theoretical algebraic approaches to connectivity in continuous or digital spaces. *Journal of Mathematical Imaging and Vision*, 8:41–58, 1998.

[122] P. Salembier, A. Oliveras, and L. Garrido. Antiextensive connected operators for image and sequence processing. *IEEE Transactions on Image Processing*, 7:555–570, 1998.

[123] J. Serra. Connectivity on complete lattices. *Journal of Mathematical Imaging and Vision*, 9:231–251, 1998.

[124] H. J. A. M. Heijmans. Connected morphological operators for binary images. *Computer Vision and Image Understanding*, 73:99–120, 1999.

[125] J. Serra. Connectivity for sets and functions. *Fundamenta Informaticae*, To Appear, 2000.

[126] A. Toet. A morphological pyramidal image decomposition. *Pattern Recognition Letters*, 9:255–261, 1989.

[127] X. Kong and J. Goutsias. A study of pyramidal techniques for image representation and compression. *Journal of Visual Communication and Image Representation*, 5:190–203, 1994.

[128] A. Morales, R. Acharya, and S.-J. Ko. Morphological pyramids with alternating sequential filters. *IEEE Transactions on Image Processing*, 4:965–977, 1995.

[129] J. Goutsias and Henk J. A. M. Heijmans. Multiresolution signal decomposition schemes. Part 1: Linear and morphological pyramids. Technical Report PNA–R9810, CWI, Amsterdam, The Netherlands, October 1998.

[130] R. L. de Queiroz, D. A. F. Florêncio, and R. W. Schafer. Nonexpansive pyramid for image coding using a nonlinear filterbank. *IEEE Transactions on Image Processing*, 7:246–252, 1998.

[131] Henk J. A. M. Heijmans and J. Goutsias. Multiresolution signal decomposition schemes. Part 2: Morphological wavelets. Technical Report PNA–R9905, CWI, Amsterdam, The Netherlands, July 1999.

[132] M.-H. Chen and P.-F. Yan. A multiscaling approach based on morphological filtering. *IEEE Transactions on Pattern Analysis and Machine Intelligence*, 11:694–700, 1989.

[133] R. van den Boomgaard and A. Smeulders. The morphological structure of images: The differential equations of morphological scale-space. *IEEE Transactions on Pattern Analysis and Machine Intelligence*, 16:1101–1113, 1994.

[134] J. A. Bangham, P. D. Ling, and R. Harvey. Scale-space from nonlinear filters. *IEEE Transactions on Pattern Analysis and Machine Intelligence*, 18:520–528, 1996.

[135] P. T. Jackway. Gradient watersheds in morphological scale-space. *IEEE Transactions on Image Processing*, 5:913–921, 1996.

[136] P. T. Jackway and M. Deriche. Scale-space properties of the multiscale morphological dilation-erosion. *IEEE Transactions on Pattern Analysis and Machine Intelligence*, 18:38–51, 1996.

[137] L. Alvarez, F. Guichard, P. L. Lions, and J. M. Morel. Axioms and fundamental equations of image processing. *Archive for Rational Mechanics and Analysis*, 123:199–257, 1993.

[138] G. Sapiro and A. Tannenbaum. Affine invariant scale-space. *International Journal of Computer Vision*, 11:25–44, 1993.

[139] B. B. Kimia, A. R. Tannenbaum, and S. W. Zucker. Shapes, shocks, and deformations I: The components of two-dimensional shape and the reaction-diffusion space. *International Journal of Computer Vision*, 13:189–224, 1995.

[140] S. Osher and J. A. Sethian. Fronts propagating with curvature-dependent speed: Algorithms based on Hamilton-Jacobi formulations. *Journal of Computational Physics*, 79:12–49, 1988.

[141] J. A. Sethian. *Level Set Methods and Fast Marching Methods – Evolving Interfaces in Computational Geometry, Fluid Mechanics, Computer Vision, and Materials Science, Second Edition.* Cambridge University Press, Cambridge, England, 1999.

[142] R. W. Brockett and P. Maragos. Evolution equations for continuous-scale morphological filtering. *IEEE Transactions on Signal Processing*, 42:3377–3386, 1994.

[143] P. Maragos. Differential morphology and image processing. *IEEE Transactions on Image Processing*, 5:922–937, 1996.

[144] G. Sapiro, R. Kimmel, D. Shaked, B. B. Kimia, and A. M. Bruckstein. Implementing continuous-scale morphology via curve evolution. *Pattern Recognition*, 26:1363–1372, 1993.

[145] L. Alvarez and J. M. Morel. Formalization and computational aspects of image analysis. *Acta Numerica*, pages 1–59, 1994.

[146] J. Weickert. *Anisotropic Diffusion in Image Processing.* Teubner-Verlag, Stuttgart, Germany, 1998.

[147] P. Maragos and M. A. Butt. Curve evolution, differential morphology, and distance transforms applied to multiscale and eikonal problems. *Fundamenta Informaticae*, To Appear, 2000.

[148] V. Caselles, F. Catte, T. Coll, and F. Dibos. A geometric model for active contours. *Numerische Mathematik*, 66:1–31, 1993.

[149] J. Barrera, G. J. F. Banon, R. A. Lotufo, and R. Hirata Jr. MMach: a mathematical morphology toolbox for the KHOROS system. *Journal of Electronic Imaging*, 7:174–210, 1998.

Index